Lattice studies of SU(3) gauge system with many fermion flavors

by

Anqi Cheng

B.S., Sichuan University, 2009

M.S., University of Colorado, 2012

A thesis submitted to the

Faculty of the Graduate School of the

University of Colorado in partial fulfillment

of the requirements for the degree of

Doctor of Philosophy

Department of Physics

2014

This thesis entitled:
Lattice studies of SU(3) gauge system with many fermion flavors
written by Anqi Cheng
has been approved for the Department of Physics

Prof. Anna Hasenfratz

Prof. Thomas DeGrand

Date

The final copy of this thesis has been examined by the signatories, and we find that both the content and the form meet acceptable presentation standards of scholarly work in the above mentioned discipline.

Cheng, Anqi (Ph.D., Physics)

Lattice studies of SU(3) gauge system with many fermion flavors

Thesis directed by Prof. Anna Hasenfratz

In this dissertation, we use various lattice methods to study SU(3) gauge theories with $N_f = 4, 8, 12, 16$ flavor fundamental fermions. We use nHYP smeared staggered fermions with a negative adjoint gauge term in our lattice formulation. Our study concentrates on the most controversial $N_f = 12$ system, and also includes some interesting results for the $N_f = 8$ system. The $N_f = 4$ and 16 systems serve as examples of QCD-like and IR-conformal systems respectively.

The direct motivation of our research is to locate the lower boundary of the conformal window in N_f for SU(3) gauge theories with N_f fermions in the fundamental representation. This is important because the candidate for walking technicolor (WTC) models could lie just under the conformal window. The WTC models provide an alternative to the Higgs mechanism and naturally break the electroweak symmetry via new strong interactions. They need large mass anomalous dimension $\gamma_m \sim 1$ over a large energy range in order to give realistic quark and lepton masses without generating excessive flavor changing neutral currents. After the discovery of the 125 GeV Higgs-like particle at the LHC, the WTC model with quasi-conformal symmetry is not excluded because it might predict a light dilaton from spontaneous breaking of the approximate conformal symmetry, which could be responsible for the 125 GeV particle.

In our investigations we discovered a novel phase bounded by two first-order bulk transitions in the 12-flavor system, where the single site shift symmetry is spontaneously broken. We used the chiral condensate, blocked Polyakov loop, low-lying Dirac eigenvalues, static potential and meson spectrum to study the nature of the novel phase, and found it is confining yet chirally symmetric, which is forbidden in the continuum. We also found the same phase structure in the 8-flavor system. Combining all the information we believe this is an artificial effect caused by the lattice discretization scheme we chose.

We then developed a universal method to extract the scale-dependent mass anomalous dimension γ_m from the eigenmode number of the massless Dirac operator. The scale-dependence of γ_m is an important discovery because it requires covering a large enough range of energy scales in order to get correct results, which were not paid attention to before. This method provides a universal probe from infrared to ultraviolet for any lattice model of interest.

We first studied the $N_f = 4$ system and observed the expected QCD-like behaviors for the mass anomalous dimension. We demonstrated our method is reliable and the systematic effects are under control even with small lattice volumes and vanishing fermion masses.

We then applied the method to the $N_f = 12$ system, where the mass anomalous dimension behaves completely differently from the $N_f = 4$ system, and indicates the existence of an infrared fixed point with mass anomalous dimension $\gamma_m^* = 0.235(27)$. For comparison we also studied the $N_f = 16$ system and found very similar behavior, which supports our conclusion about $N_f = 12$ on its infrared dynamics.

We also explored the $N_f = 8$ system, where the results are hard to interpret. However, we did observe clear walking behavior of the mass anomalous dimension at different gauge couplings, which makes this system interesting for further study.

In the exploration of the $N_f = 12$ system we developed a code for a stochastic estimator to efficiently measure the mode number without calculating the eigenvalues. This improvement allows us to cover large energy scales on large lattice volumes, and significantly helps extrapolation to the infrared and infinite volume limit. We also implemented the stochastic estimator with the highly improved staggered quark (HISQ) action and the Wilson action, which can be used in the future studies.

Dedication

To my husband Honghua and my family.

Acknowledgements

I first sincerely thank my advisor Professor Anna Hasenfratz. Her consistent encouragement and stimulation are indispensable to the completion of my Ph.D work. Over the years I have tremendously benefited from her extensive knowledge and experience, and I am always inspired by her creativity and passion in doing physics.

David Schaich deserves special acknowledgement as the previous postdoctoral scholar in our group. He is always helpful and resourceful answering my questions no matter in physics, programming or writing. His extremely organized way of doing research continuously benefits me even after his leaving.

I am grateful to our collaborators for helpful comments and discussions on our research. They include D. Kaplan, D. Son, S. Sharpe, J. Kuti, S. Schaefer, P. Damgaard, Tamas Kovacs and Krzysztof Cichy. I am indebted to Agostino Patella and Tom DeGrand on advice developing code to stochastically calculate the mode number.

I thank Prof. Tom DeGrand for teaching me quantum field theories and Prof. Oliver DeWolfe for hosting the discussion forum on advanced topics in quantum field theories. I also want to thank Dr. Yuzhi Liu and my fellow graduate students Gregory Petropoulos and Oscar Henriksson for insightful discussions on physics.

I acknowledge the theoretical high energy group and the physics department at CU for financially supporting me doing research in the form of research and teaching assistantships.

Finally I want to express my deep gratitude to Prof. Xiangsong Chen, who led me to the amazing physics world in the first place.

Contents

Chapter

1 Introduction 1

2 The Composite Higgs 5

2.1 The SM Higgs model 5

2.1.1 Overview 5

2.1.2 Problematic aspects of the SM Higgs 8

2.2 The composite Higgs models 9

2.2.1 From χSB to EWSB 9

2.2.2 "Walking" 11

2.3 The conformal window of SU(N) theories 12

3 Lattice gauge theory 18

3.1 Action on lattice 18

3.1.1 Gauge bosons on lattice 20

3.1.2 Fermions on lattice 20

3.2 Improvements of the action 23

3.2.1 Fermionic part: nHYP smearing 24

3.2.2 Gauge part: negative adjoint term 25

3.3 Observables 29

3.3.1 Polyakov loop 29

3.3.2 Static potential 30

3.3.3 Meson spectrum 30

3.4 Formulation and simulation 31

4 Novel phase in SU(3) $N_f = 12$ system 33

4.1 Introduction 33

4.2 Phase structure 34

4.3 Single-site shift symmetry breaking 38

4.4 Eigenvalue Spectrum 41

4.5 Static potential and meson spectrum 46

4.6 The 8-flavor case 51

4.7 Conclusion 52

5 Dirac Eigenmodes 54

5.1 Introduction and Overview 54

5.2 Mass anomalous dimension from the mode number 56

5.3 Concerns about the Dirac eigenvalue density 60

5.4 Potential systematic effects 61

5.4.1 Systematic effects from direct calculation 61

5.4.2 Systematic effects from stochastic calculation 69

5.5 Stochastic estimator of Dirac eigenmode number 74

5.5.1 Overview 74

5.5.2 Approximation of the spectral projector $\mathbb{P}_\Omega$ 74

5.5.3 Implementation 76

5.6 Results for the $N_f = 4$ systems 78

5.7 Results for the $N_f = 12$ system 83

5.8 Results for the $N_f = 8$ system 89

5.9 Results for the $N_f = 16$ system 92

5.10 Conclusion 93

6 Conclusion 97

Bibliography 100

Appendix

A Code of the step function in the stochastic estimator 108

Tables

Table

2.1 Notations of gauge fields 5

2.2 Fermion Fields of the Standard Model 7

3.1 Classes of mesons in the continuum. 31

3.2 Phase factors of staggered meson operators. 31

5.1 $N_f = 4$ lattice ensembles used in Figs. 5.4, 5.5, 5.6, 5.15 and 5.16. For each ensemble specified by the volume, fermion mass, and gauge coupling β_F, we report the total molecular dynamics time units generated with the HMC algorithm, the number of configurations on which we measure at least 1000 (1500) eigenvalues, and the fit range $\Delta\lambda$. 81

5.2 $N_f = 12$ lattice ensembles used in direct calculation (Figs. 5.7, 5.8 and 5.17), with columns as in Table 5.1. 85

5.3 $N_f = 12$ lattice ensembles used in stochastic estimator (Figs. 5.11, 5.12, 5.18). Columns are lattice volume, fermion mass, tgauge coupling β_F, otal MDTU and the number of thermalized configurations on which measurements are made. Each fit uses 3 point and λ are measured with constant separation $\Delta\lambda = 0.01$. 85

5.4 $N_f = 8$ lattice ensembles used direct calculation (Figs. 5.23 and 5.21), with columns as in Table 5.1. 90

5.5 $N_f = 8$ lattice ensembles used in stochastic calculation (Fig. 5.22). All configurations are in chiral limit (zero mass). Each fit uses 3 points while λ are measured with constant separation $\Delta\lambda = 0.02$. 91

5.6 $N_f = 16$ lattice ensembles used with stochastic estimator (Fig. 5.24 and 5.25). All fermion masses are set to zero. Each fit uses 3 point and λ are measured with constant separation $\Delta\lambda = 0.01$. 93

Figures

Figure

2.1 Beta function behaviors for different systems. The green line represents QCD-like ($N_f < 8.05$) systems, the purple line represents IR slavery systems ($N_f > 16.5$) and the red line represents the IR conformal system with an IRFP at g^* ($8.05 < N_f < 16.5$). 15

2.2 Walking behaviors in the beta function and the running gauge coupling. (a) The beta function approaches zero near g^*, and turns back without crossing. (b) The gauge coupling runs very slowly where the beta function is very small, and it is this behavior called “walking”. 15

2.3 From [1]. Conformal window for $SU(N)$ theories with fermions in the (from top to bottom) (i) fundamental (gray) (ii) two-index antisymmetric (blue), (iii) two-index symmetric (red), (iv) adjoint (green) representations, as a function of flavor number N_f and color number N. The upper solid curves represents loss of asymptotic freedom, the lower solid curve represents onset of chiral symmetry breaking, and the dashed curves show existence of an IR fixed point. 16

3.1 Cartoon of gauge bosons and fermions on 2D lattice. 19

3.2 From [2]. Hypercubic blocking in three dimensions (Eqns. 3.35-3.38). (a) The ‘fat’ link $\tilde{V}$ (thick dark line in the center) is built from four staples of intermediate links $\bar{V}$(double line). (b) Each intermediate link $\bar{V}$ is built from two staples of U in the hypercubes directly attached to the original link. 25

3.3 Phase diagram for pure SU(2)[3] (left) and SU(3) [4] (right) lattice gauge theory with fundamental-adjoint couplings. 27

3.4 Phase diagram for SU(3) lattice gauge theory with fundamental-adjoint couplings and 12 fundamental fermions [5]. The red line is the first order transition (solid) and its continued crossover (dashed). The horizontal blue line at $\beta_A = 0$ is studied by MCRG matching, the second blue line is $\beta_A/\beta_F = -0.25$ which the author advocated because it is far away from the red line and its extension, and the green line is $\beta_A/\beta_F = -0.5$ which flips the system into a new universal class. 28

4.1 The chiral condensate $\langle\overline{\psi}\psi\rangle$ (on a log scale) and the blocked Polyakov loop $\langle \mathrm{Tr} L_b\rangle$ indicate two well-separated transitions at $m = 0.005$. 34

4.2 The stronger-coupling transitions in the $\beta_F - m$ plane at several temperatures and volumes, signaled by $\langle\overline{\psi}\psi\rangle$ 36

4.3 The weaker coupling transitions in the $\beta_F - m$ plane at several temperatures and volumes, signaled by $\langle \mathrm{Tr} L_b\rangle$. 37

4.4 The two bulk transitions merge as m increase. Small vertical offsets distinguish the different volumes, and lines connect the points to guide the eye. The transitions are nearly identical on zero-temperature volumes, and the finite-temperature transitions appear to converge to these bulk transitions. 37

4.5 (a) The plaquette difference ΔP_t (Eqn. 4.4) measured on $16^3\times32$ volumes in both the $\cancel{S^4}$ phase ($\beta_F = 2.6,\ m = 0.005$) and the weak-coupling phase($\beta_F = 2.7,\ m = 0.005$), as functions of the molecular dynamics time. 39

4.6 the link difference ΔL_t (Eqn. 4.5) measured on $16^3 \times 32$ volumes in both the $\cancel{S^4}$ phase ($\beta_F = 2.6,\ m = 0.005$) and the weak-coupling phase($\beta_F = 2.7,\ m = 0.005$), as functions of the molecular dynamics time. 40

4.7 The low-lying eigenvalues $\langle\lambda_i\rangle$ in the $\cancel{S^4}$ phase ($\beta_F = 2.6$) for $m = 0.005$ on the four volumes $12^4, 12^3 \times 24, 16^4$ and $16^3 \times 32$. The dashed line shows the soft edge $\lambda_0 = 0.0175(5)$ found in the fit plotted in Fig. 4.9. 42

4.8 The low-lying eigenvalues $\langle\lambda_i\rangle$ in the weak-coupling phase ($\beta_F = 2.7$), for $m = 0.005$ on the four volumes $12^4, 12^3 \times 24, 16^4$ and $16^3 \times 32$. 42

4.9 Scaling of the low-lying eigenvalues in the $\cancel{S^4}$ phase ($\beta_F = 2.6$) for $m = 0.005$ on the four volumes $12^4, 12^3 \times 24, 16^4$ and $16^3 \times 32$. The soft edge $\lambda_0 = 0.0175(5)$. 44

4.10 Scaling of the low-lying eigenvalues in the weak-coupling phase ($\beta_f = 2.7$) for $m = 0.005$ on the four volumes $12^4, 12^3 \times 24, 16^4$ and $16^3 \times 32$. $\lambda_0 = 0$ but $x_0 \sim 3$. 44

4.11 The HYP-smeared static potential in the $\cancel{S^4}$ phase at $\beta_F = 2.6$ and the weak-coupling phase at $\beta_F = 2.7$. 46

4.12 The masses of the Goldstone π_5, its "a_5" parity partner, the π_{05} pseudoscalar and the a_0 scalar in the $\cancel{S^4}$ phase at $\beta_F = 2.6$ on $12^3 \times 24$ and $16^3 \times 32$ lattices. 47

4.13 The masses of the Goldstone π_5, the π_{05} pseudoscalar, the a_0 scalar and π_{i5} vector in the weak-coupling phase at $\beta_F = 2.7$ on $12^3 \times 24$ (except π_{i5}) and $16^3 \times 32$ lattices. 48

4.14 The ρ and a_1 are degenerate in both the weak-coupling phase at $\beta_F = 2.7$ as well as the $\cancel{S^4}$ phase at $\beta_F = 2.6$. At $\beta_F = 2.7$ this degeneracy is a familiar effect. At $\beta_F = 2.6$, it is consistent with our observation of chiral symmetry in the eigenvalue spectrum. 49

4.15 The chiral condensate $\langle\overline{\psi}\psi\rangle$ (on a log scale) in the $N_f = 8$ flavor system at $m = 0.005$ on 12^4 and 16^4 lattices. The phase between the two first order transitions is an $\cancel{S^4}$ phase like that we observe for $N_f = 12$. 50

5.1 Cartoons of eigenvalue densities $\rho(\lambda)$ and scale-dependent mass anomalous dimension γ_m in in IR-conformal (left) and chirally broken (right) continuum systems. In the IR-conformal systems (left), on the weak coupling side of the IRFP γ_m grows toward γ_m^* at the IR fixed point as $\lambda \to 0$, while on the strong coupling we conjecture γ_m increases with energy as suggested by the dashed blue line, motivated from a backward flow in the gauge coupling. In the chirally broken systems (right), spontaneous chiral symmetry breaking produces $\rho(0) \propto \langle\bar{\psi}\psi\rangle \neq 0$ in the infrared, which does not follow the scaling form $\rho(\lambda) \propto \lambda^{\alpha(\lambda)}$. In both systems, asymptotic freedom predicts $\gamma_m \to 0$ as $\lambda \to \infty$ in the UV. 57

5.2 The eigenvalue density $\rho(\lambda)$ at $\beta_F = 2.8$ of the 12 flavor system on $16^3 \times 32$ volumes at various sea fermion mass values. 62

5.3 The eigenvalue density $\rho(\lambda)$ at $\beta_F = 2.8$ of the 12 flavor system with mass $m = 0.0025$ on various volumes. 64

5.4 The volume dependence of the $\rho(\lambda)$ at $\beta_f = 6.4$ for $N_f = 4$. At this stronger coupling the system exhibits chiral symmetry breaking with $\rho(0) > 0$ on $24^3 \times 48$ lattices with $m = 0.0025$. The insets enlarge the small-λ behavior. 65

5.5 The volume dependence of the $\rho(\lambda)$ at $\beta_f = 7.0$ for $N_f = 4$. At this weaker coupling all three lattice systems are volume-squeezed and we encounter no obstacle to working directly at $m = 0$ on all three volumes. The insets enlarge the small-λ behavior. . . . 66

5.6 Predictions for γ_m from the scaling of ν for $N_f = 4$ at coupling $\beta_F = 6.4$, illustrating finite-volume effects at small λ . We observe $\gamma_m > 1$ on $24^3 \times 48$ lattices with $m = 0.0025$, consistent with chiral symmetry breaking found in Fig. 5.4. 66

5.7 Predictions for γ_m from the scaling of ν for $N_f = 12$ at $\beta_F = 4.0$, illustrating finite-volume effects at small λ 67

5.8 Finite volume effects for 12-flavor systems at $\beta_F = 5.0$, where the finite volume effects get so strong that we can hardly see any overlap between different volumes. . 68

5.9 The mass anomalous dimension γ_m for $N_f = 12, \beta_F = 5.0$ on volume $24^3 \times 48$. The red band uses mode number from direct calculation, and the green band uses mode number from stochastic estimator. They overlap and confirm the correctness of the stochastic estimator. 69

5.10 The mass anomalous dimension γ_m for $N_f = 12, \beta_F = 5.0$ on volume $24^3 \times 48$ with periodic spatial conditions and 24^4 with anti-periodic spatial conditions. The 24^4 has a larger bump due to finite volume effects, but the finite volume effects on the two ensembles disappear at the same $\lambda \sim 0.34$, and merge together afterwards. . . . 70

5.11 Finite volume effects for 12-flavor systems at $\beta_F = 6.0$ using stochastic estimator. Although $\beta_F = 6.0$ is the weakest coupling with most severe finite volume effects in our study, which seem to be further magnified by anti-periodic boundary conditions, we still manage to combine different lattices and obtain volume-independent physics at large enough λ 71

5.12 Predictions for γ_m from the scaling of ν for $N_f = 12$ at $\beta_F = 4.0$ from stochastic calculation, where we are able to extend λ range on large volumes, and obtain perfect overlap among different volumes. 72

5.13 . Finite mass effects, tested on 12-flavor systems at $\beta_F = 4.0$. At $m = 0.02$ and $m = 0.025$, heavy fermion masses explicitly break chiral symmetry and cause unphysical large γ_m in the small λ region, but they join the curve from 32^4, $m = 0$ ensemble shortly. 73

5.14 . Minmax polynomial approximation of sign(x). Both lines fix $\epsilon = 0.0025$. Full line uses $n = 22$ and has 5% relative error in the range $\sqrt{\epsilon} \leq |x| \leq 1$, while the dashed line uses $n = 57$ and has 0.1% relative error in the same range. 75

5.15 . The mass anomalous dimension for $N_f = 4$ system. At each gauge coupling, results from several lattice volumes are combined and the small λ regions affected by finite volume effects are cut off. 79

5.16 . Mass anomalous dimension for $N_f = 4$ system. We rescale the $N_f = 4$ results to be expressed in terms of a common lattice spacing ($a_{7.4}$ corresponding to $\beta_F = 7.4$). The dashed line is the one-loop perturbative prediction of the mass anomalous dimension. 82

5.17 . The effective mass anomalous dimension γ_m for $N_f = 12$ model using direct calculation. At weaker couplings the finite volume effects are large. 84

5.18 . The mass anomalous dimension γ_m for $N_f = 12$ model using stochastic calculation. All volumes overlap and essentially indistinguishable. 84

5.19 Extrapolations of γ_m from the results at the largest volumes (see Table. 5.3) at each coupling. The bands are data and the dashed lines are extrapolations. The common intercept is predicted to be 0.235(27). 87

5.20 Extrapolations of γ_m from twice nHYP smeared configurations. The bands are data and the dashed lines are extrapolations. The common intercept is predicted to be 0.231(36). 88

5.21 The mass anomalous dimension γ_m for $N_f = 8$ model from direct calculation. 89

5.22 The mass anomalous dimension γ_m for $N_f = 8$ model from stochastic calculation. All measurements are in chiral limit. 90

5.23 Volume dependence of the spectral density $\rho(\lambda)$, normalized per continuum flavor, for $N_f = 8$ with $\beta_F = 4.65$. We do not observe spontaneous chiral symmetry breaking even on our largest $24^3 \times 48$ and $32^3 \times 64$ volumes. The insets enlarge the small-λ behavior. 91

5.24 The mass anomalous dimension γ_m for $N_f = 16$ system. 94

5.25 Linear extrapolations of γ_m from multiple couplings with a common intercept. The intercept is 0.025(10). Though it should not be taken too seriously, it is consistent with the perturbative prediction 0.022. 94

Chapter 1

Introduction

This research is motivated by the desire to understand the mechanism of electroweak symmetry breaking (EWSB). In the standard model (SM), electromagnetic and weak interactions are unified uniformly by the $SU(2)_L \times U(1)_Y$ gauge group, while in low energy regime the electromagnetic and weak interactions behave completely differently. This is where EWSB comes in. The W and Z bosons gain masses via the symmetry breaking scheme:

$$SU(2)_L \times U(1)_Y \to U(1)_{EM}. \tag{1.1}$$

While EWSB is widely recognized as the mass generation mechanism for elementary particles, its underlying interactions remain unknown.

The simplest and most well known proposal is the Higgs mechanism. In this picture, an elementary scalar particle is introduced into the gauge fields and induces the spontaneous electroweak symmetry breaking. Despite its simplicity, the Higgs model is unsatisfactory as a fundamental model, which we will discuss in detail in chapter 2.

On the other hand, inspired by quantum chromodynamics (QCD), it is appealing to explore the possibility that some novel strong dynamics governs the physics beyond the electroweak scale and results in EWSB via chiral symmetry breaking (χSB). This framework is given the name 'technicolor' (TC), taking QCD with its three colors as a role model [6, 7]. Later the extended technicolor (ETC) models were developed, where the standard model quarks and leptons are connected to technifermions and acquire masses via exchanging the ETC bosons [8, 9]. However, ETC models generically suffer from the excessive flavor-changing neutral currents (FCNC's) [10]. In order to resolve the contradiction a 'walking' scenario is proposed (WTC), where the large, approximately constant mass anomalous dimension $\gamma_m \sim 1$ over large energy scales could suppress the FCFC's. In particular, in the walking technicolor model first proposed in [11], a light dilaton is predicted from the weakly broken conformal symmetry, which is compatible with the 125 GeV particle discovered at LHC. Even if the particle discovered at 125 GeV turns out to be an elementary scalar, the study of these strongly coupled systems remains important not only for theory but model building as well.

The WTC models with a light dilaton require quasi-conformal symmetry, where an approximate infrared fixed point (IRFP) governs the physics just above the electroweak scale, and induces the 'walking' behavior. Therefore tremendous efforts have been put in searching for the 'conformal window' of SU(N) gauge theories, in the phase space of color N, flavor N_f and fermionic representations. For a review see [1].

Our group studies the SU(3) gauge theory with many flavor fermions in the fundamental representation. The universal two-loop beta function indicates a second zero appears when $8.05 \leq N_f \leq 16.5$, and estimates based on the Dyson-Schwinger equation raises the lower boundary to ≈ 12 [12]. Locating the lower boundary of the conformal window N_f^*, is non-perturbative in nature and has to be put onto lattice. Various numerical tools that have been developed to study lattice QCD can be well adapted to investigate this new class of models. Examples include phase structure, spectral studies, Schrődinger functional (SF) studies, potential schemes, and Monte Carlo Renormalization Group (MCRG) methods. We use staggered fermions with normalized hypercubic (nHYP) smearing and a negative adjoint term in the gauge action. The details of the lattice action we use will be introduced in chapter 3. In this dissertation we focus on the phase structure and scale-dependent mass anomalous dimension from Dirac eigenmodes.

On the lattice the continuous Euclidean space-time is discretized. While the real physics lies in the continuum limit, various lattice artificial phases could appear in the lattice system. Therefore it is important to study the phase structure of the lattice theory and identify the genuine features of continuum physics. Our investigations of the phase diagram of the 12-flavor SU(3) model have identified a novel phase where the single site shift symmetry is spontaneously broken ('$\cancel{S^4}$'). We use the chiral condensate, (blocked) Polyakov loop, Dirac eigenvalue spectrum, static potential and meson spectrum to show that the novel phase is bounded by first order bulk transitions, and possesses both confinement and chiral symmetry, which is forbidden in the continuum. Moreover, this phase is also discovered in the 8-flavor system, which is believed to have different infrared dynamics. Therefore we believe the novel phase is a lattice artifact due to the specific discretization scheme we choose in our study. The details of the novel phase are presented in chapter 4.

We then study the weak coupling phase of the 8- and 12-flavor systems using the renormalization group (RG) invariant eigenmode number of the massless Dirac operator from which we extract the mass anomalous dimension γ_m. We combine different lattice volumes as well as different gauge couplings, and carefully explore potential systematic effects. We discover that the mass anomalous dimension is scale dependent. This discovery is important because it indicates analysis not covering a range of energy scales might get precise but incorrect results. We also test this method on the 4- and 16-flavor systems. This method is universal and can be applied to any lattice model of interest.

The $N_f = 4$ system is known to be QCD-like and the mass anomalous dimension behaves as expected near an asymptotically free UV fixed point: it decreases as the energy scale increases and as the coupling weakens. We also manage to combine results from different gauge couplings into a single curve which overlaps with the one-loop perturbative prediction in the UV once the lattice scales are matched with the continuum ones. The $N_f = 12$ system is completely different: the mass anomalous dimension at strong couplings increases towards the UV, and results at different couplings converge to a common value $\gamma_m^* = 0.23(3)$ in the infrared limit, which we identify as the scheme-independent mass anomalous dimension at the IR fixed point. The results for the $N_f = 8$ system are hard to interpret but the approximate constant mass anomalous dimension across a large energy range at each coupling is consistent with the 'walking' scenario, and makes this system interesting to study. Finally the $N_f = 16$ system which is believed to be infrared conformal, shows very similar behaviors to the $N_f = 12$ system, further supporting our conclusion for the $N_f = 12$

system. The details are in chapter 5.

One important step in the above exploration is developing a stochastic estimator to efficiently measure a large number of Dirac eigenmodes on large lattice volumes. It involves defining a spectral projector which projects the Dirac eigenmodes into a subspace where the eigenvalues are smaller than a given cutoff, and then calculating the number of low-lying eigenmodes with five stochastic sources. I have also implemented the stochastic estimator for highly improved staggered quarks (HISQ) action and Wilson action, so that similar analysis with different lattice formulations could be done in the further.

Chapter 2

The Composite Higgs

The standard model Higgs, originally proposed in the early 1960's, is an elementary scalar particle that spontaneously breaks the electroweak symmetry and gives mass to $W^{\pm}, Z$ bosons. The discovery of a Higgs-like particle of mass $m_h \approx 125$ GeV at the Large Hadron Collider in 2013 [13, 14] seems again to confirm the spectacular success of the Standard Model. However, the possibility that the Higgs-like particle is not elementary but composite still remains. For a unified description of composite Higgs models see Ref. [15]. In this chapter we will first briefly revisit the Standard Model Higgs model and its unsatisfying features, proceed to a brief overview of the walking technicolor models that have a light dilaton consistent with the current data of the 125 GeV resonance, and conclude with the SU(N) gauge theories which could potentially contain the candidates for the walking technicolor models.

2.1 The SM Higgs model

2.1.1 Overview

We begin with the Lagrangian of the electroweak sector of SM (notations are in table 2.1):

Table 2.1: Notations of gauge fields

	generators	gauge bosons	coupling
$U(1)_Y$	Y	B_μ	g'
$SU(2)_L$	τ	W^i_μ	g

$$\mathcal{L}_{EW} = -\frac{1}{4}W^i_{\mu\nu}W^{\mu\nu i} - \frac{1}{4}B_{\mu\nu}B^{\mu\nu} \tag{2.1}$$

where

$$W^i_{\mu\nu} = \partial_\nu W^i_\mu - \partial_\mu W^i_\nu + g\epsilon^{ijk}W^j_\mu W^k_\nu, \tag{2.2}$$

$$B_\mu\nu = \partial_\nu B_\mu - \partial_\mu B_\nu. \tag{2.3}$$

To partially break the symmetry a complex scalar field Φ is introduced:

$$\mathcal{L}_s = (D^\mu\Phi)^\dagger(D_\mu\Phi) - V(\Phi), \tag{2.4}$$

where

$$D_\mu = \partial_\mu + i\frac{g}{2}\tau \cdot W_\mu + i\frac{g'}{2}B_\mu Y. \tag{2.5}$$

and the potential term is given by:

$$V(\Phi) = -\mu^2\Phi^\dagger\Phi + \lambda(\Phi^\dagger\Phi)^2 \quad (\lambda > 0). \tag{2.6}$$

The scalar field Φ develops a nonzero vacuum expectation value (VEV), which can be chosen to be:

$$\langle\Phi\rangle = \frac{1}{\sqrt{2}}\begin{pmatrix} 0 \\ \nu \end{pmatrix}, \tag{2.7}$$

where $\nu = \sqrt{\mu^2/\lambda}$. This VEV remains invariant under the $U(1)_{EM}$ subgroup generated by:

$$Q = Y + \tau^3. \tag{2.8}$$

Physically Q is recognized as the electromagnetic charge, and the unbroken $U(1)_{EM}$ subgroup describes electromagnetism. The Higgs particle comes in as small perturbations to the ground state:

$$\Phi(x) = \frac{1}{\sqrt{2}}\begin{pmatrix} 0 \\ \nu + h(x) \end{pmatrix}. \tag{2.9}$$

Substitute 2.9 into 2.6 and use 2.7:

$$V(h) = 2\lambda\nu^2 h(x), \tag{2.10}$$

at the leading order of $h(x)$. Therefore the mass of Higgs is $M_h = \sqrt{2\lambda}\nu$.

The kinetic term in 2.4 becomes:

$$(D^\mu\Phi)^\dagger(D_\mu\Phi) = \frac{1}{2}(\partial_\mu h)^2 + \frac{g^2\nu^2}{8}((W_\mu^1)^2 + (W_\mu^2)^2) + \frac{\nu^2}{8}(g'B_\mu - gW_\mu^3)^2 \tag{2.11}$$

$$\equiv \frac{1}{2}(\partial_\mu h)^2 + m_W^2 W_\mu^+ W^{-\mu} + \frac{1}{2}m_Z^2 Z_\mu Z^\mu, \tag{2.12}$$

where the gauge bosons:

$$W_\mu^\pm = \frac{1}{2}(W_\mu^1 \mp iW_\mu^2) \tag{2.13}$$

$$Z_\mu = \frac{-g'B_\mu + gW_\mu^3}{\sqrt{g^2 + g'^2}}, \tag{2.14}$$

obtain masses from the Higgs mechanism:

$$m_W^2 = \frac{1}{4}g^2\nu^2, \tag{2.15}$$

$$m_Z^2 = \frac{1}{4}(g^2 + g'^2)\nu^2. \tag{2.16}$$

The gauge boson of the unbroken $U(1)_{EM}$ group remains massless:

$$A_\mu = \frac{gB_\mu + g'W_\mu^3}{\sqrt{g^2 + g'^2}}, \tag{2.17}$$

$$m_A = 0. \tag{2.18}$$

Table 2.2: Fermion Fields of the Standard Model

Field	SU(3)	$SU(2)_L$	$U(1)_Y$
$Q_L = \begin{pmatrix} u_L \\ d_L \end{pmatrix}$	3	2	1/6
u_R	3	1	2/3
d_R	3	1	− 1/3
$L_L = \begin{pmatrix} \nu_L \\ e_L \end{pmatrix}$	1	2	− 1/2
e_R	1	1	− 1

The $SU(2)_L \times U(1)_Y$ electroweak theory joins with QCD to form the complete $SU(3)_C \times SU(2)_L \times U(1)_Y$ standard model. However, since the left-handed and right-handed fermions live in different representations (see table 2.2), explicit mass terms of the form:

$$\mathcal{L}_{mass} = -m\bar{\psi}\psi = -m(\bar{\psi}_L\psi_R + \bar{\psi}_R\psi_L) \tag{2.19}$$

are forbidden by gauge invariance. A 'bonus' of the Higgs particle is that it could give masses to fermions via the gauge invariant Yukawa coupling:

$$\mathcal{L}_{mass} = -\sum_{\psi} \lambda_\psi \bar{\psi}_L \Phi \psi_R + h.c.\ , \tag{2.20}$$

substituting Φ with 2.9 gives the mass of fermions:

$$m_\psi = \frac{1}{\sqrt{2}}\lambda_\psi \nu. \tag{2.21}$$

2.1.2 Problematic aspects of the SM Higgs

Though simple and efficient, the Higgs model is unsatisfactory as a fundamental theory to the Planck scale in several aspects:

(1) Dynamics: The parameter ν can be calculated from the interaction strength of muon decay:

$$\nu = (\sqrt{2}G_F)^{-1/2} = 246\ GeV. \tag{2.22}$$

However, there is no dynamical principle underlying the energy scale $\nu = 246$ GeV.

(2) Naturalness: The Higgs mass:

$$m_h = \sqrt{2\lambda}\nu \sim 125 \text{ Gev} \tag{2.23}$$

is vastly smaller than the Planck mass (10^{19} Gev). This requires incredible fine tuning to correct for the large quadratic radiative corrections.

(3) Triviality: the self-coupling $\lambda(M)$ at energy scale M:

$$\lambda(M) \simeq \frac{\lambda(\Lambda)}{1 + (24/16\pi^2)\lambda(\Lambda)\log(\Lambda/M)} \tag{2.24}$$

vanishes when the cutoff $\Lambda \to \infty$. This indicates the Higgs model is at best an *effective* theory.

One other thing physicists expect a fundamental theory to do where the SM Higgs model fails is to provide a dynamical explanation of flavor symmetry. The origin and scale of flavor symmetry breaking is unknown. The Yukawa coupling of the Higgs boson to fermions is put in by hand and bears no physical constraints.

2.2 The composite Higgs models

The above concerns about the SM Higgs model have led to extensive studies of alternative electroweak symmetry breaking schemes. Technicolor (TC) models introduce new strong dynamics beyond the electroweak scale and generate masses for W and Z bosons through new gauge interactions . In particular, in quasi-conformal walking technicolor models a light, composite boson named technidilaton [11, 16, 17, 18], remains as a competitor of the SM Higgs for the 125 GeV resonance. A systematic exploration of the possibility that the new particle observed at LHC is not the SM Higgs but a dilation from spontaneous (approximate) conformal symmetry breaking can be found in Ref. [19]. As the TC models must exhibit spontaneously chiral symmetry breaking (χSB), in this section I will begin with considering 2-flavor QCD to illustrate what is χSB, and how χSB could induce EWSB; then briefly discuss what is 'walking' and why it is desirable. For a detailed review of technicolor models we refer to Ref. [20].

2.2.1 From χSB to EWSB

We begin with an introduction of chiral symmetry breaking in QCD with massless up and down quarks. The Lagrangian of the fermions is

$$\mathcal{L}_f = i\bar{\psi}\gamma^\mu D_\mu\psi, \quad \psi = (u\ d)^T, \tag{2.25}$$

where $D_\mu = \partial_\mu - ig_3 T^a G^a_\mu$, G are gluons, $T^a = \frac{1}{2}\lambda^a$ and λ^a are the Gell-Mann matrices. If we define left-handed and right-handed quarks as

$$\psi_L = \frac{1}{2}(1-\gamma_5)\psi \equiv P_L\psi, \tag{2.26}$$

$$\psi_R = \frac{1}{2}(1+\gamma_5)\psi \equiv P_R\psi, \tag{2.27}$$

the Lagrangian can be rewritten as

$$\mathcal{L}_f = i\bar{\psi}_L \gamma^\mu D_\mu \psi_L + i\bar{\psi}_R \gamma^\mu D_\mu \psi_R. \tag{2.28}$$

$\mathcal{L}$ is invariant under transformations

$$\psi_L \to L\psi_L, \quad \psi_R \to R\psi_R, \tag{2.29}$$

where L and R are independent 2×2 unitary matrices. This global flavor symmetry is often denoted by $U(2)_L \times U(2)_R$, and called chiral symmetry since the left- and right-handed quarks transform independently. This symmetry can be decomposed into $SU(2)_L \times SU(2)_R \times U(1)_V \times U(1)_A$.

The $U(1)_A$ symmetry has an anomaly and therefore has no corresponding conserved quantity; the $U(1)_V$ symmetry corresponds to the conserved quark number; the $SU(2)_V$ symmetry where $L = R$ is the isospin symmetry of hadrons, and it is the $SU(2)_A$ symmetry with $L = R^\dagger$ that does not exist in low energy QCD. The only explanation for the absence of $SU(2)_A$ symmetry in the hadrons is that the axial symmetry is spontaneously broken. Such symmetry breaking generates three Goldstone bosons. The nonzero VEV required to spontaneously break chiral symmetry cannot be obtained from elementary scalar operators without losing Lorentz symmetry or the SU(3) color symmetry, so composite scalars are the natural option. The simplest candidate of composite scalars to achieve this goal is the chiral condensate with a non-zero VEV

$$\langle\overline{\psi}\psi\rangle = \langle\bar{\psi}_L \psi_R + \bar{\psi}_R \psi_L\rangle \neq 0. \tag{2.30}$$

The three Goldstone bosons (the poins π^a) generated from the spontaneous chiral symmetry breaking can be described by an effective low-energy Lagrangian

$$\mathcal{L}_{pi} = \frac{f_\pi^2}{4}\mathrm{Tr}[(D_\mu U)^\dagger D^\mu U], \tag{2.31}$$

where

$$U = \exp(2i\pi^a T^a / f_\pi), \tag{2.32}$$

T^a are the generators of SU(2) and π^a are three real scalars which are identified to be pions, and f_π is the pion decay constant.

The technicolor models, originally proposed as scaled-up QCD, are chosen to be in the spontaneously chiral symmetry broken regime. When coupled to the SM, the Goldstone bosons associated with the broken TC chiral symmetry are eaten by the SM gauge bosons, generating EWSB. To see this, we replace the Lagrangian of the complex scalar fields in SM Higgs model (Eqn. 2.4) with the effective Lagrangian of pions (Eqn. 2.31), where the covariant derivative is [21]

$$iD_\mu U = (-\frac{4}{f_\pi} T^a \partial_\mu \pi^a + g_2 T^a W_\mu^a - g_1 T^3 B_\mu)U. \tag{2.33}$$

Now if we expand $\frac{f_\pi^2}{4}\mathrm{Tr}[(D_\mu U)^\dagger D^\mu U]$ like we expanded $(D^\mu \Phi)^\dagger (D_\mu \Phi)$ in Eqn. 2.11, we will recover the mass terms for $W^\pm$ and Z gauge bosons in the Standard Model.

2.2.2 "Walking"

Although it neatly breaks the electroweak symmetry without introducing elementary scalar fields, the TC models have a hard time accommodating fermion masses and mixings. The so-called extended technicolor (ETC) models introduce new gauge interactions between technifermions and quarks as well as leptons, so that the quarks and leptons acquire mass through exchanging the ETC gauge bosons. The effective field theory at low energy scale $\mu \lesssim \Lambda_{ETC}$, where the heavy ETC bosons are integrated out, has three types of effective four-fermion interactions:

$$\frac{1}{\Lambda_{ETC}^2}\{\alpha_{ab}(\bar{T}\gamma_\mu t^a T)(\bar{T}\gamma^\mu t^b T) + \beta_{ab}(\bar{T}\gamma_\mu t^a T)(\bar{q}\gamma^\mu t^b q) + \gamma_{ab}(\bar{q}\gamma_\mu t^a q)(\bar{q}\gamma^\mu t^b q)\}, \tag{2.34}$$

where T are technifermions, q are quarks and leptons and t are ETC generators. The α terms give techiaxion masses, the β terms give quark and lepton masses and the γ terms are associated with flavor-changing neutral currents (FCNC). In the scaled-up QCD version of ETC models, the constraints from FCNC severely contradict with realistic quark and lepton masses. For example, The $K_L - K_S$ mass difference, which is well measured experimentally, puts a lower bound $\Lambda_{ETC} \gtrsim$ 1000 TeV. This leads to a nonphysically small upper bound on the quark and lepton masses $m_{q,l} \lesssim$ 100 MeV, assuming the coefficients $\beta \sim \gamma$.

To solve the FCNC problem a 'walking' scenario is proposed. The key observation is that the FCNC terms are proportional to $1/\Lambda_{ETC}^2$ while the generic quark and lepton masses are proportional to $\langle \bar{T}T\rangle^2_{ETC}/\Lambda^2_{ETC}$. The extra factor $\langle \bar{T}T\rangle^2_{ETC}$ is the technifermion bilinear condensate renormalized at Λ_{ETC}. It evolves from the Λ_{TC} scale via the renormalization equation:

$$\langle \bar{T}T\rangle^2_{ETC} = \langle \bar{T}T\rangle^2_{TC} \exp(\int_{\Lambda_{TC}}^{\Lambda_{ETC}} \frac{d\mu}{\mu}\gamma_m(\mu)). \tag{2.35}$$

If we assume the $\gamma_m(\mu)$ is **not** negligible above Λ_{TC} like it is in QCD, but remains large and approximately constant up to Λ_{ETC}, then the quark and lepton masses are enhanced by a factor

$$\langle \bar{T}T\rangle^2_{ETC} \simeq \langle \bar{T}T\rangle^2_{TC} (\frac{\Lambda_{ETC}}{\Lambda_{TC}})^{\gamma_m}. \tag{2.36}$$

The nonperturbative expression of γ_m can be obtained from the ladder approximation of the Schwinger-Dyson "mass-gap" equations [11], which is

$$\gamma_m(\mu) = 1 - (1 - \alpha_{TC}(\mu)/\alpha_c)^{1/2}, \tag{2.37}$$

where α_c is the critical coupling that triggers chiral symmetry breaking by definition. Eqn 2.37 constraints $\gamma_m(\mu) \leq 1$. To keep γ_m large across large energy scales, we require the beta function close to zero near α_c so that $\alpha_{TC}(\mu)$ runs slowly and remains close to α_c in a large energy range. This is the so-called 'walking' behavior, which is depicted in Fig. 2.2.

The maximum renormalization enhancement can be achieved with $\gamma_m \approx 1$ from Λ_{TC} to Λ_{ETC}. With $\Lambda_{TC} \approx 1$ TeV and $\Lambda_{ETC} \gtrsim 100$ TeV, the quarks and lepton masses can be enhanced to 1 GeV. This enhancement is large enough to accommodate the charm quarks and possibly bottom quarks, but certainly not top quarks. Alternative mechanisms are proposed to generate the third generation quark masses, but they are out of the scope of this dissertation. Finally we want to point out that, although the FCNC problem is described in the framework of ETC here, it is general for many composite Higgs models that involve strong dynamics, therefore the walking behavior is a generally desirable feature for these models.

2.3 The conformal window of SU(N) theories

In the walking technicolor models people assume the mass anomalous dimension, and thus also the gauge coupling $g(\mu)$, remains large and approximately constant across a large energy range.

This assumption is interesting and now it is a critical question whether such a theory really exists. Ref. [11, 16] proposed a scale-invariant/conformal model featured with an asymptotically **nonfree** ultraviolet fixed point, near which the mass anomalous dimension $\gamma_m \sim 1$ based on the Schwinger-Dyson equation in ladder approximation, and therefore naturally solves the FCNC problem without fine tuning. In particular, this model predicts a pseudo- Nambu-Goldstone boson associated with the spontaneous breaking of the scale invariance, which remains as a candidate for the 125 GeV resonance at LHC [22, 23].

There have been tremendous efforts searching for a concrete quasi-conformal 'walking' model from the general class of SU(N) gauge theories with N_f flavor fermions. The hints for the existence of a walking theory comes from the universal two loop beta function, which indicates an infrared fixed point (IRFP) exists in the conformal window $[N_f^*, N_f^{up}]$. The 'walking' behaviors are expected with N_f slightly below the conformal window.

To illustrate the idea we start from the two-loop beta function for a generic non-Abelian gauge theory (group G) with fermions in representation R [24]:

$$\beta(g) = -b_0 \frac{g^3}{(4\pi)^2} - b_1 \frac{g^5}{(4\pi)^4}, \tag{2.38}$$

where

$$b_0 = \frac{11}{3} C_2(G) - \frac{4}{3} T(R), \tag{2.39}$$

$$b_1 = \frac{34}{3} C_2^2(G) - \frac{20}{3} C_2(G) T(R) - 4 C_2(R) T(R). \tag{2.40}$$

$C_2(R)$ stands for the quadratic Casimir operator of the representation R, and $T(R)$ is the trace normalization factor of the representation R.

Taking the SU(3) group with N_f fermion multiplets in the fundamental representation as an example, the relevant group invariants are

$$C_2(G) = N = 3, \tag{2.41}$$

$$T(R) = \frac{1}{2} N_f, \tag{2.42}$$

$$C_2(R) = \frac{N^2 - 1}{2N} = \frac{4}{3}. \tag{2.43}$$

The coefficients of the beta function become:

$$b_0 = 11 - \frac{2}{3}N_f, \tag{2.44}$$

$$b_1 = 102 - \frac{38}{3}N_f. \tag{2.45}$$

Based on the value of N_f the behaviors of the system at two-loop perturbation level can be classified into three categories:

- $N_f < 8.05$. b_0 and b_1 are both positive. The beta function is negative and monotonically decreasing. The theory is asymptotically free and QCD-like.
- $N_f > 16.5$. b_0 and b_1 are both negative. The beta function is positive and monotonically increasing. This category is uninteresting for our current purpose.
- $8.05 < N_f < 16.5$. b_0 is negative and b_1 is positive. In this range the beta function develops a nontrivial zero, which indicates the theory has a nontrivial infrared fixed point and therefore conformal.

Fig. 2.1 shows a cartoon of the beta function for the above three categories. Right below the conformal window we might see the walking behaviors, which is illustrated in Fig. 2.2. Therefore finding the exact location of the lower edge of the conformal window becomes the center of the search for the walking theory. Ref. [12] argues that chiral symmetry breaking is triggered when the quark mass anomalous dimension $\gamma_m = 1$, and boosts the N_f^* to ~ 12. A general phase diagram for SU(N) theories with many fermions in various representations are given in Fig. 4.2.

While the perturbative theory provides useful guidance in the search of conformality, precisely determining the lower boundary of the conformal window is non-perturbative in nature and has to be studied on lattice. Many lattice studies have therefore focused on determining whether given models exhibit confinement and chiral symmetry breaking, or if they develop an IR fixed point resulting in IR conformality [25, 26, 27, 28]. SU(3) gauge theory with $N_f = 12$ fundamental flavors has merged in lattice studies as one of the most controversial models [29, 30, 31, 5, 32, 33, 34, 35, 36, 37, 38, 39, 40, 41, 42](see Ref.[27] for a recent review). A large-scale study of the $N_f = 12$ system concluded

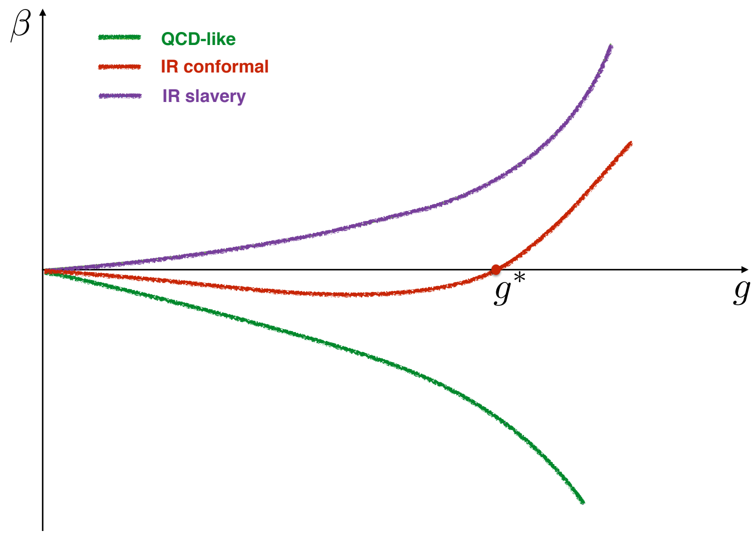

Figure 2.1: Beta function behaviors for different systems. The green line represents QCD-like ($N_f < 8.05$) systems, the purple line represents IR slavery systems ($N_f > 16.5$) and the red line represents the IR conformal system with an IRFP at g^* ($8.05 < N_f < 16.5$).

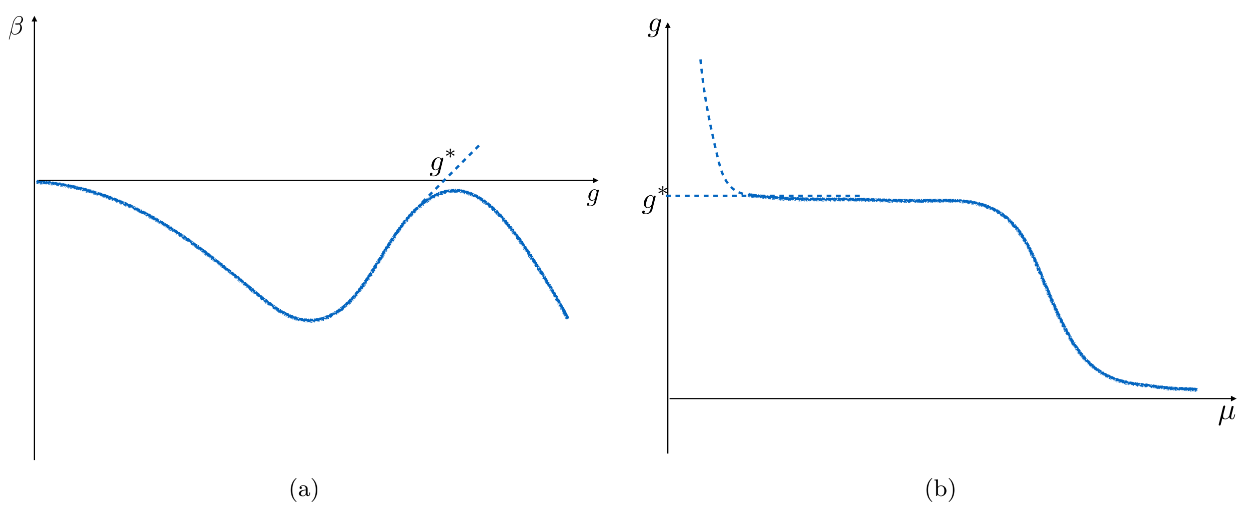

Figure 2.2: Walking behaviors in the beta function and the running gauge coupling. (a) The beta function approaches zero near g^*, and turns back without crossing. (b) The gauge coupling runs very slowly where the beta function is very small, and it is this behavior called “walking”.

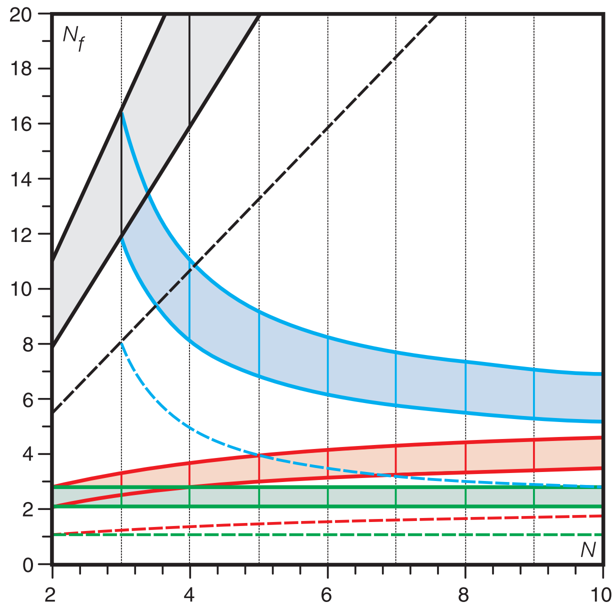

Figure 2.3: From [1]. Conformal window for $SU(N)$ theories with fermions in the (from top to bottom) (i) fundamental (gray) (ii) two-index antisymmetric (blue), (iii) two-index symmetric (red), (iv) adjoint (green) representations, as a function of flavor number N_f and color number N. The upper solid curves represents loss of asymptotic freedom, the lower solid curve represents onset of chiral symmetry breaking, and the dashed curves show existence of an IR fixed point.

that their data favored a confining, chirally broken scenario [33], though other groups interpreted these data as consistent with IR conformality [35, 36]. We investigated the same system with the Monte Carlo renormalization group (MCRG) two-lattice matching method [5, 34, 39], finding an IRFP consistent with IR-conformal dynamics. Recently the LatKMI collaboration discovered a scalar state lighter than the pion due to the dilatonic nature of conformality [43].

The $N_f = 8$ system is also interesting. The two loop beta function predicts it right below the conformal window. However, since this two-loop perturbative fixed point is at very strong coupling, higher-loop corrections could be significant [44, 45]. Analytic estimates based on the Dyson-Schwinger equation [46, 1] or a conjectured thermal inequality [47] put the lower edge of the conformal window around $N_f \approx 12$, leaving the 8-flavor system well in the chirally broken regime. It is indeed generally believed that the $N_f = 8$ is below the conformal window from lattice studies [48, 49, 29, 31, 5, 50, 51, 52, 53, 54, 55]. Ref. [28] found the meson spectrum of the 8-flavor system using HISQ action is consistent with spontaneous chiral symmetry breaking while the finite size scaling indicates large $\gamma_m \sim 1$, and therefore could be a candidate for walking technicolor models.

Chapter 3

Lattice gauge theory

As we have seen in chapter 2, strongly coupled gauge-fermion systems, beyond their intrinsic theoretical interest, play an essential role in many theories of physics beyond the standard model. Lattice gauge theory is at present the most reliable method to study strongly coupled gauge-fermions systems in a systematic, controlled way. Lattice QCD has gained prominent success [56, 57, 58, 59]. This chapter is arranged as following: section 3.1 introduces a simple lattice action; section 3.2 describes two improvements to the action that we implemented in our simulation, section 3.3 gives definition of some useful observables we will use in later chapters, and finally section 3.4 briefly describes the lattice formation and simulation procedures. For more detailed introduction and reviews of lattice gauge theory we refer to [60, 61, 62, 63, 64].

3.1 Action on lattice

We start with the action of general SU(N) gauge theories in the continuum:

$$S[\psi, \bar{\psi}, A_\mu] = S_F[\psi, \bar{\psi}, A_\mu] + S_G[A_\mu], \tag{3.1}$$

where

$$S_F[\psi, \bar{\psi}, A_\mu] = \int d^4x \bar{\psi}(\gamma_\mu(\partial_\mu + igA_\mu(x)) + m)\psi \tag{3.2}$$

$$\equiv \int d^4x \bar{\psi} D(m) \psi, \tag{3.3}$$

$$S_G[A_\mu] = \frac{1}{2} \int d^4x \mathrm{Tr}[F_{\mu\nu}(x) F_{\mu\nu}(x)], \tag{3.4}$$

$$F_{\mu\nu}(x) = \partial_\mu A_\nu(x) - \partial_\nu A_\mu(x) + ig[A_\mu(x), A_\nu(x)] \tag{3.5}$$

The $\psi, \bar{\psi}$ are fermions, $D(m)$ is the Dirac operator in the continuum, and $A_\mu = A_\mu^a T^a$ are gauge fields of SU(N) group with generators T^a.

The action is invariant under local SU(N) symmetry:

$$\psi_A(x) \to [\Omega(x)]_{AB}\psi_B(x), \tag{3.6}$$

$$\bar{\psi}_A(x) \to \bar{\psi}_B(x)[\Omega(x)^\dagger]_{BA}, \tag{3.7}$$

$$A_\mu(x) \to \Omega(x)A_\mu\Omega(x)^\dagger + \frac{i}{g}(\partial_\mu\Omega(x))\Omega(x)^\dagger. \tag{3.8}$$

When the theory is put on discrete lattice $\Lambda = \{\vec{n},\ n_\mu = 0, ..., N_\mu - 1\}$, the fermions $\psi(n)$ live on the lattice sites while the gauge bosons are associated with the lattice links by defining

$$U_{n,\mu} = \exp[igaA_\mu(n + a\hat{\mu}/2)], \tag{3.9}$$

where a is the lattice spacing.

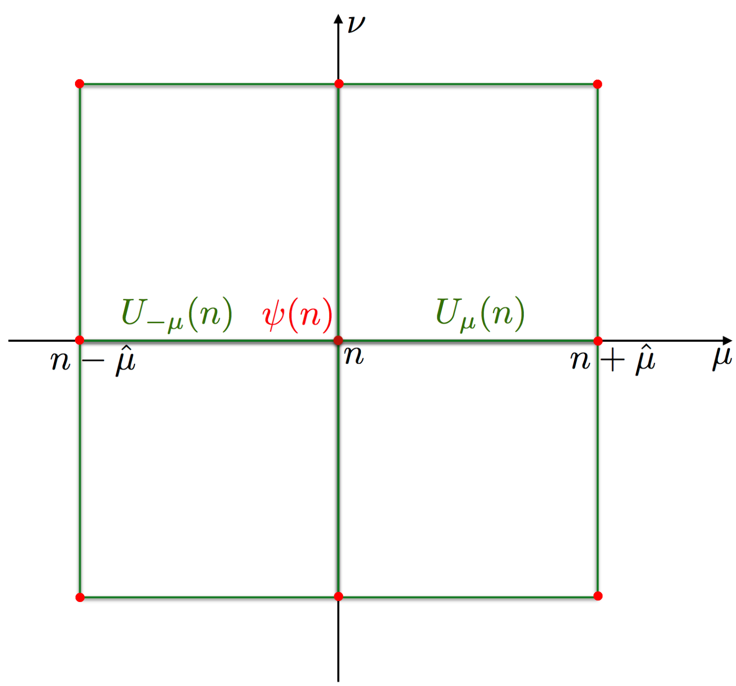

Figure 3.1: Cartoon of gauge bosons and fermions on 2D lattice.

3.1.1 Gauge bosons on lattice

The simplest gauge invariant object built from U is the trace of the path ordered product along a square (which is called a plaquette):

$$\mathrm{Tr}\ \Box_{\mu\nu}(n) = \mathrm{Tr}\ U_{n,\mu} U_{n+\hat{\mu},\nu} U^{\dagger}_{n+\hat{\nu},\mu} U^{\dagger}_{n,\nu}. \tag{3.10}$$

Expansion of $\Box_{\mu\nu}$ in terms of lattice spacing a gives

$$\Box_{\mu\nu} \backsimeq 1 - ia^2 F_{\mu\nu} - \frac{a^4}{2} F_{\mu\nu} F^{\mu\nu} + ... \tag{3.11}$$

Therefore by summing over the traces of all plaquettes we can recover the standard gauge action given in Eqn. 3.13 to the lowest order in a:

$$\sum_{n,\mu>\nu} [N - \mathrm{Tr}\Box_{\mu,\nu}(n)] \backsimeq \int d^4x \frac{1}{2} F_{\mu\nu} F^{\mu\nu}. \tag{3.12}$$

In convention the lattice gauge action is written as

$$S = \beta \sum_{n,\mu>\nu} (1 - \frac{1}{N} \mathrm{Tr}\ \Box_{\mu\nu}(n)) \tag{3.13}$$

where β is the inverse gauge coupling:

$$\beta = \frac{2N}{g^2}. \tag{3.14}$$

This is the simplest gauge action on lattice and it is the Wilson action [65]. It gives the correct continuum action at the lowest order of expansion in lattice spacing a. More sophisticated gauge actions are proposed to deal with higher order corrections [66, 67, 68] but they are out of the scope of this document. In the next section we will introduce a negative adjoint term to avoid a well-know first order transition caused by lattice artifacts on the fundamental-adjoint coupling plane.

3.1.2 Fermions on lattice

3.1.2.1 Naive discretization

The most obvious and naive discretization of the fermion action is:

$$\begin{aligned} S_F[\psi, \bar{\psi}, U] &= \sum_n \bar{\psi}(n) [\frac{1}{2a} \sum_{\mu=1}^{4} \gamma_\mu (U_{n,\mu} \psi(n+\hat{\mu}) - U_{n,-\mu} \psi(n-\hat{\mu})) + m\psi(n)] \quad (3.15) \\ &\equiv \bar{\psi} D_{naive}(m) \psi. \quad (3.16) \end{aligned}$$

with the transformation property:

$$\psi(n) \to \Omega(n)\psi(n), \quad U_{n,\mu} \to U'_{n,\mu} = \Omega(n)U_{n,\mu}\Omega(n+\hat{\mu})^\dagger, \tag{3.17}$$

$$\bar{\psi}(n) \to \bar{\psi}(n)\Omega(n)^\dagger, \quad U_{n,-\mu} \to U'_{n,-\mu} = \Omega(n)U_{n,-\mu}\Omega(n-\hat{\mu})^\dagger. \tag{3.18}$$

However, such naive discretization is problematic. To see this, we can take a look at the free fermion propagator:

$$\begin{aligned} S_F[\psi,\bar{\psi}] &= \sum_n \bar{\psi}(n)(\frac{1}{2a}\sum_{\mu=1}^{4}\gamma_\mu(\psi(n+\hat{\mu})-\psi(n-\hat{\mu})+m\psi(n)) & (3.19)\\ &= \sum_{n_1,n_2}\bar{\psi}(n_1)D(n_1|n_2)\psi(n_2) & (3.20)\end{aligned}$$

After a Fourier transform, the free momentum-space propagator is

$$\tilde{D}(p)^{-1} = \frac{m - i\sum_\mu \gamma_\mu \sin(p_\mu)}{m^2 + \sum_\mu \sin^2(p_\mu)}. \tag{3.21}$$

The usual fermion propagator is recovered in the small $p_\mu \sim (0,0,0,0)$ regime where $\gamma^\mu \sin(p_\mu) \approx \not{p}$. However, now on lattice we have another fifteen clones of the propagator in the corners of the Brillouin zone. Therefore the naive discretization will generate sixteen degenerate fermions, which are not physical. This is the well known 'doubling problem'.

3.1.2.2 Fermions on lattice: Staggered fermions

To overcome the doubling problem two schemes are widely used: Wilson fermions and staggered fermions. Wilson fermions, proposed by K. G. Wilson, directly remove the extra doublers in the hypercube, by inserting an extra term in the propagator which does not vanish at the redundant fifteen corners of the Brillouin zone. However, this is accomplished at the expense of explicitly breaking chiral symmetry on the lattice. Staggered fermions, introduced by Kogut and Susskind [69], start from the naive formulation and diagonalize the sixteen degeneracies into four blocks, therefore reducing the degeneracy from sixteen to four. To achieve fewer species in this formulation, people sometimes take the square root (two species) or the fourth root (one species) of the determinant, which is controversial [70, 71, 72, 73, 74, 75, 76]. Although staggered fermions do not completely remove the doublers, it is advantageous in retaining a residual chiral symmetry. More advanced formulations like domain-wall fermions, which introduces an auxiliary fifth dimension that suppresses chirality-violating effects, are out of the scope of this dissertation and we refer to ref. [77] for more details. We use staggered fermions with N_f equal to a multiple of four in our work and avoid the "rooting" problem. Therefore I will briefly introduce the formulation of staggered fermions in this section.

To condense the degeneracy, we define a local transformation matrix:

$$\Omega_n = \gamma_1^{n_1}\gamma_2^{n_2}\gamma_3^{n_3}\gamma_4^{n_4}, \tag{3.22}$$

where $n_\mu' s$ are integers and (n_1, n_2, n_3, n_4) donate the sites on the lattice. The fermion fields are then transformed to

$$\psi(n) \to \Omega_n \psi'(n), \quad \bar{\psi}(n) \to \bar{\psi}'(n)\Omega_n^\dagger \tag{3.23}$$

Now we can rewrite the fermion action Eqn. 3.15 in terms of ψ'

$$S_F[\psi', \bar{\psi}', U] = \frac{1}{2a}\sum_{n,\mu}\bar{\psi}'(n)\alpha_\mu(n)[U_{n,\mu}\psi'(n+\hat{\mu}) - U_{n,-\mu}\psi'(n-\hat{\mu})] + m\sum_n \bar{\psi}'(n)\psi'(n), \tag{3.24}$$

where $\alpha_\mu(n)$ is defined as:

$$\alpha_\mu(n) \equiv \Omega_n^\dagger \gamma_\mu \Omega_{n+\hat{\mu}} = (-1)^{n_1+n_2+\ldots+n_{\mu-1}} \tag{3.25}$$

Now the action becomes diagonal in the spinor space, i.e., the four components of ψ' are independent, so we can keep one component of the spinor and discard the other three. The remaining one-component fermion field, denoted by χ, is the so called 'staggered fermion'. The action of the staggered fermions is:

$$\begin{aligned} S_F[\chi, \bar{\chi}, U] &= \frac{1}{2}\sum_{n,\mu}\bar{\chi}(n)\alpha_\mu(n)[U_{n,\mu}\chi(n+\hat{\mu}) - U_{n,-\mu}\chi(n-\hat{\mu})] + m\sum_n \bar{\chi}(n)\chi(n) \quad (3.26) \\ &\equiv \bar{\chi}D_{stagger}(m)\chi. \quad (3.27) \end{aligned}$$

One staggered fermion corresponds to four species in the continuum, which is often referred as 'taste". However, the taste symmetry is only exact in the continuum. To see this, notice that because of the alternating sign of α_μ, the action is invariant under shifts by $2a$, therefore it is natural to divide the lattice into 2^4 hypercubes, by defining

$$n = 2y + \eta, \quad \text{where } \eta = 0, 1. \tag{3.28}$$

If we rewrite the four-spinor Dirac fields in this spin-taste basis as

$$\psi_y^{\alpha a} = \frac{1}{8} \sum_\eta \Omega_\eta^{\alpha a} \chi(2y + \eta), \tag{3.29}$$

where α is the spinor index and a is the taste index, we can see the problem: on the lattice the different elements of the Dirac spinor are distributed to different sites of the 2^4 hypercube, and therefore they experience different gauge fields. This leads to taste breaking, which gets worse if the gauge fields become coarser. To reduce this problem various smearing techniques are introduced, and in the next section we will briefly introduce the smearing scheme we use in our simulations.

On the other hand, instead of completely breaking chiral symmetry like Wilson fermions, staggered fermions have remnant $U(1)_A$ symmetry from the chiral symmetry. At zero mass, the action is invariant under the $U(1)_A$ transformation

$$\psi(y) \to \exp(i\theta\gamma_5 \otimes \gamma_5)\psi(y), \tag{3.30}$$

$$\bar{\psi}(y) \to \bar{\psi}(y)\exp(i\theta\gamma_5 \otimes \gamma_5), \tag{3.31}$$

where the left γ_5 is in spin space and the right in taste space. The Goldstone boson associated with this symmetry is a taste-nonsinglet $\bar{\psi}(\gamma_5 \otimes \gamma_5)\psi$. Although there is only one Goldstone boson for staggered fermions, its existence protects fermion masses from additional renormalization and makes staggered fermions practical to use.

3.2 Improvements of the action

We implement two improvements to the original staggered action: In the fermionic part, we apply normalized hypercubic blocking (nHYP)-smearing to smooth gauge configurations and reduce the taste symmetry breaking; In the gauge part, we add an negative adjoint plaquette term, to avoid a well-known spurious UVFP caused by lattice artifacts.

3.2.1 Fermionic part: nHYP smearing

As we have mentioned, staggered fermions are affected by taste breaking, i.e., the four fermion tastes described by each (unrooted) staggered field are degenerate only in the continuum limit. Smearing the gauge connections reduces this problem, and following Ref. [5, 34, 2], we use nHYP-smeared staggered fermions.

nHYP smearing consists three consecutive smearing steps restricted to the hypercubes that are directly attached to the original link. In a single smearing step we first add a staple sum

$$\Delta_{n,\mu} = \sum_{\nu\neq\mu} U_{n,\nu} U_{n+\hat{\nu},\mu} U^{\dagger}_{n+\hat{\mu},\nu} \tag{3.32}$$

to the original link $U_{n,\mu}$ as

$$\Gamma_{n,\mu} = (1-\alpha) U_{n,\mu} + \frac{\alpha}{m} \Delta_{n,\mu}, \tag{3.33}$$

where m is the number of staples in the staple sum and α is the smearing parameter. Then we can construct a U(N) unitary matrix as

$$V_n = \Gamma(\Gamma^{\dagger}\Gamma)^{-1/2}. \tag{3.34}$$

The three level of smearing is constructed as:

Step I:

$$\bar{\Gamma}_{n,\mu;\nu,\rho} = (1-\alpha_3) U_{n,\mu} + \frac{\alpha_3}{2} \sum_{\pm\eta\neq\rho,\nu,\mu} U_{n,\eta} U_{n+\hat{\eta},\mu} U^{\dagger}_{n+\hat{\mu},\eta}, \tag{3.35}$$

$$\bar{V} = \bar{\Gamma}(\bar{\Gamma}^{\dagger}\bar{\Gamma})^{-1/2}; \tag{3.36}$$

Step II:

$$\tilde{\Gamma}_{n,\mu;\nu} = (1-\alpha_2) U_{n,\mu} + \frac{\alpha_2}{4} \sum_{\pm\rho\neq\nu,\mu} \bar{V}_{n,\rho;\nu,\mu} \bar{V}_{n+\hat{\rho},\mu;\rho,\nu} \bar{V}^{\dagger}_{n+\hat{\mu},\rho;\nu,\mu}, \tag{3.37}$$

$$\tilde{V} = \tilde{\Gamma}(\tilde{\Gamma}^{\dagger}\tilde{\Gamma})^{-1/2}; \tag{3.38}$$

Step III:

$$\Gamma_{n,\mu} = (1-\alpha_1) U_{n,\mu} + \frac{\alpha_1}{6} \sum_{\nu\neq\mu} \tilde{V}_{n,\nu;\mu} \tilde{V}_{n+\hat{\nu},\mu;\nu} \tilde{V}^{\dagger}_{n+\hat{\mu},\nu;\mu}, \tag{3.39}$$

$$V = \Gamma(\Gamma^{\dagger}\Gamma)^{-1/2}. \tag{3.40}$$

The $U_{n,\mu}$ are the original links from site n in direction μ, and $V_{n,\mu}$ are the final nHYP smeared links. The indices after the semi-colon are excluded from the sums. Fig. 3.2 [2] schematically shows the smearing steps in three dimensions. Notice that in three dimension we only have two smearing steps, which can be thought of as the first two of three steps in four dimensions.

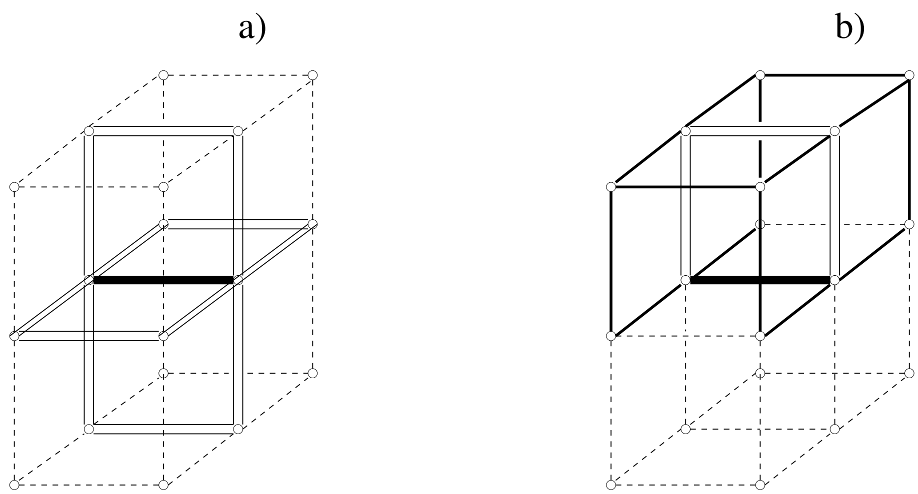

Figure 3.2: From [2]. Hypercubic blocking in three dimensions (Eqns. 3.35-3.38). (a) The 'fat' link $\tilde{V}$ (thick dark line in the center) is built from four staples of intermediate links $\bar{V}$(double line). (b) Each intermediate link $\bar{V}$ is built from two staples of U in the hypercubes directly attached to the original link.

The nHYP smearing greatly smooths the gauge configurations, with minimal distortion of short distance physics by restricting itself in the hypercubes directly attached to the original link. While it significantly improves the taste symmetry of staggered fermions [78, 79], the U(N) projection in the nHYP construction can break down at strong coupling, due to the generation of near-zero eigenvalues in the staple sum. We address this difficulty by adjusting the three HYP smearing parameters to

$$\alpha_1 = 0.5, \quad \alpha_2 = 0.5, \quad \alpha_3 = 0.4. \tag{3.41}$$

3.2.2 Gauge part: negative adjoint term

Lattice calculations are affected by discretization errors, and much effort has been devoted to improving lattice actions to reduce these effects. Strongly-coupled systems are particularly sensitive to these lattice artifacts, which can contaminate or destroy the scaling of the desired continuum limit, even to the point of generating spurious ultraviolet fixed points (UVFPs). Care must be taken that lattice simulations are in the basin of attraction of the perturbative fixed point, or its associated IRFP if it exists.

The existence of a first order phase transition caused by lattice artifacts in the fundamental-adjoint plaquette gauge action of pure gauge SU(N) theory has been well known [3, 80, 4]. To tell the story we start with the SU(N) gauge action containing only plaquette terms in all possible representations[4]:

$$S = \sum_R \tilde{\beta}_R \sum_\Box [1 - \frac{1}{d(R)} \mathrm{Re}\ \mathrm{Tr}_R \Box], \tag{3.42}$$

where the index R indicates representations of $SU(N)$ group, $d(R)$ is the dimension of representation R and $\tilde{\beta}_R$ is the corresponding gauge coupling. In particular we are interested in the mixed fundamental-adjoint action:

$$S_{AF} = \tilde{\beta}_F \sum_\Box [1 - \frac{1}{N} \mathrm{Re}\ \mathrm{Tr}_F \Box] + \tilde{\beta}_A \sum_\Box [1 - \frac{1}{N^2 - 1} \mathrm{Re} \mathrm{Tr}_A \Box]. \tag{3.43}$$

The trace over a plaquette in fundamental and adjoint representation is related via the identity:

$$\mathrm{Tr}_A \Box = \mathrm{Tr}_F \Box^\dagger \mathrm{Tr}_F \Box - 1 \tag{3.44}$$

Therefore we can rewrite the action into:

$$S_{AF} = \beta_F \sum_\Box [1 - \frac{1}{N} \mathrm{Re}\ \mathrm{Tr}_F \Box] + \beta_A \sum_\Box [1 - \frac{1}{N^2} \mathrm{Tr}_F \Box^\dagger \mathrm{Tr}_F \Box], \tag{3.45}$$

where

$$\beta_F = \tilde{\beta}_F, \quad \beta_A = \frac{N^2}{N^2 - 1} \tilde{\beta}_A. \tag{3.46}$$

With this action the phase diagrams of SU(2) and SU(3) pure gauge theory are shown in Fig. 3.3. In SU(2) systems Ref. [81, 82] found abnormal behaviors of RG flow along the fundamental axis near the extension of the first order transition. In SU(3) system the first order transition is found to end at a critical point at $(\beta_F, \beta_A) = (4.00(7), 2.06(8))$ (Fig. 3.3) [4], which indicates the existence of a spurious UVFP. Ref. [83] discovered large scaling violation or breaking near the transition and its extension with negative adjoint coupling. It is tricky to tune the gauge couplings in order to to access interesting physics without encountering the first order transition.

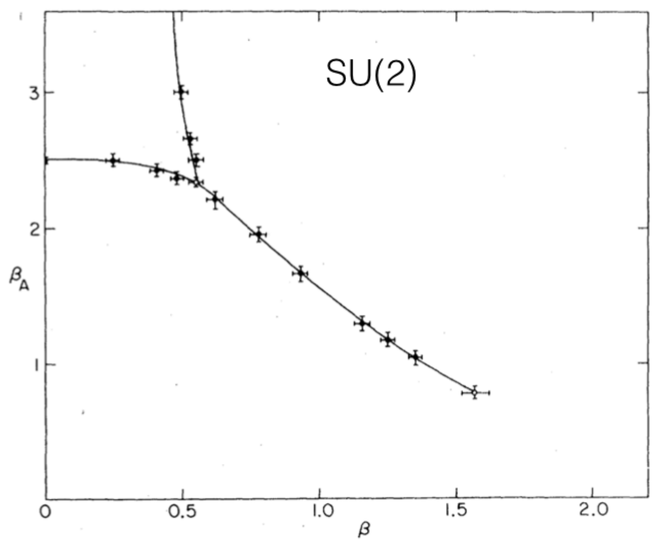

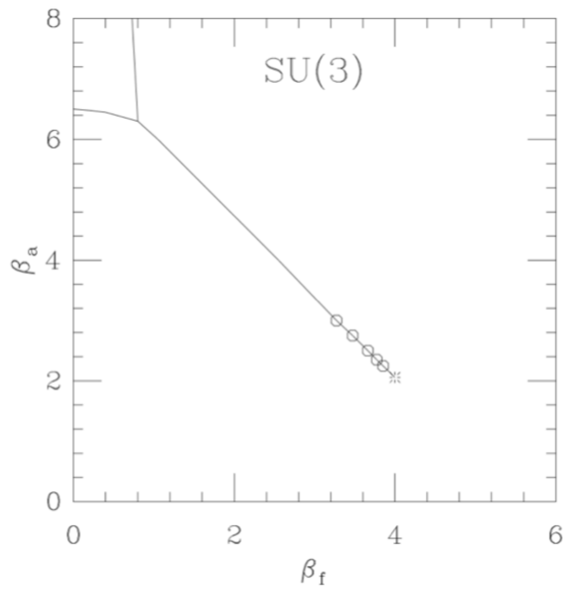

Figure 3.3: Phase diagram for pure SU(2)[3] (left) and SU(3) [4] (right) lattice gauge theory with fundamental-adjoint couplings.

Ref. [34] studied the phase structure of SU(3) gauge theory fundamental-adjoint gauge couplings with 12 fundamental fermions, and proposed to fix the ratio β_A/β_F to be -0.25. Along the line there will be a safe segment far away from the first order transition and its extension, yet contain interesting physics. In Fig. 3.4 [34] the red line indicates the first order transition (solid) continued with a crossover (dashed), and the horizontal blue line at $\beta_A = 0$ is studied by Monte Carlo Renormalization Group (MCRG) matching in Ref. [5]. The second blue line is a segment of $\beta_A/\beta_F = -0.25$ line, which far away from the red line, and finally the green line is $\beta_A/\beta_F = -0.5$ where the large negative adjoint term dominates and completely changes the system.

In the present work we follow the suggestion from Ref. [5] and use a gauge action includes both fundamental and adjoint plaquette terms, with coefficients related by $\beta_A = -0.25\beta_F$. With this constant ratio, the perturbative relation to the bare coupling is

$$6/g^2 = \beta_F + 2\beta_A = \beta_F/2. \tag{3.47}$$

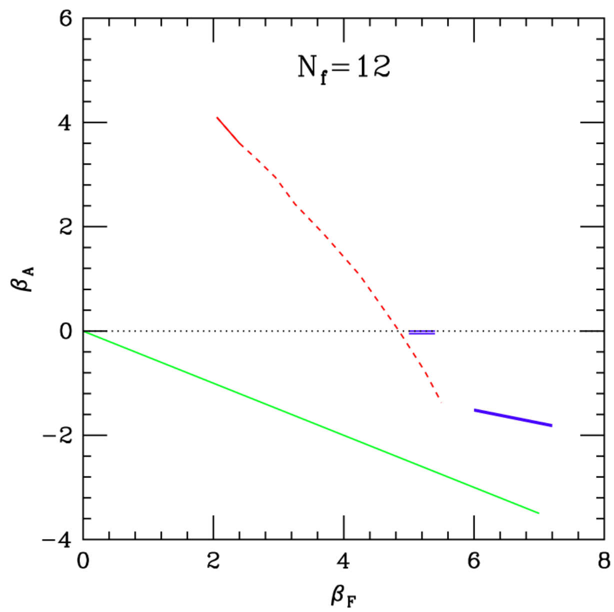

Figure 3.4: Phase diagram for SU(3) lattice gauge theory with fundamental-adjoint couplings and 12 fundamental fermions [5]. The red line is the first order transition (solid) and its continued crossover (dashed). The horizontal blue line at $\beta_A = 0$ is studied by MCRG matching, the second blue line is $\beta_A/\beta_F = -0.25$ which the author advocated because it is far away from the red line and its extension, and the green line is $\beta_A/\beta_F = -0.5$ which flips the system into a new universal class.

3.3 Observables

In this section we will introduce several observables which will be used in the following chapters: the Polyakov loop, the static potential and the meson operators. The first two observables are used to detect confinement in the system.

3.3.1 Polyakov loop

The Polyakov loop is a loop that wraps around the lattice in the periodic temporal direction:

$$\mathcal{P}(x) = \mathrm{Tr} \prod_{\tau} U_{\mathbf{x},\tau}. \tag{3.48}$$

The expectation value of a single Polyakov loop is related to the free energy of an isolated static fermion (point source):

$$\langle \mathcal{P}(x) \rangle = \exp(-F_0/T), \tag{3.49}$$

where F_0 is the free energy of a single static fermion, and the temperature T is the inverse of the lattice temporal extent:

$$T = \frac{1}{aN_\tau}. \tag{3.50}$$

At the first thought one might conclude that F_0 should be infinite for confinement, leading to a zero expectation value of the Polyakov loop. However, due to symmetry requirements as we are going to show, it is actually zero under confinement.

The center of the SU(N) group is isomorphic to the cyclic group Z(N). That means for a given time slice, multiplying all links by an element z of Z(N) should leave the action invariant. Under such a transformation the Polyakov loop $\langle \mathcal{P} \rangle \rightarrow z\langle \mathcal{P} \rangle$. Therefore $\langle \mathcal{P} \rangle$ should be zero unless a static fermion exists and breaks the symmetry, i.e.:

$$\begin{aligned} \langle \mathcal{P} \rangle &= 0, \quad \text{deconfined, Z(N) unbroken,} & (3.51)\\ &\neq 0, \quad \text{confined, Z(N) broken.} & (3.52) \end{aligned}$$

Therefore the Polyakov loop is an order parameter for confinement in pure gauge theories. It is also used in detecting the finite temperature transitions as we do in chapter 4.

3.3.2 Static potential

A single Polyakov loop is no longer an order parameter when dynamical fermions come into play. We can construct a more reliable indicator from two Polyakov loops. The correlation of a pair of Polyakov loops in opposite directions is related to the potential of a pair of static fermions:

$$\langle \mathcal{P}^\dagger(x)\mathcal{P}(x+R)\rangle = \exp(-\frac{V(R)}{T}). \tag{3.53}$$

Phenomenologically the static potential $V(r)$ between a static fermion pair can be parameterized as:

$$V(r) = V_0 + \sigma r + \frac{b}{r}, \tag{3.54}$$

where σ is the string tension, which indicates confinement when it is nonzero, and the b/r is the Coulombic term. Therefore we can fit the lattice simulation data of the static potential to Eqn. 4.11 and check whether it is consistent with confinement or not. To get the lattice scale we can also calculate the Sommer scale r_0 [84] in lattice units by

$$r^2 F(r)|_{r=r_0} = 1.65, \tag{3.55}$$

where the force $F(r)$ can be obtained from the potential:

$$F(r) = \frac{d}{dr}V(r) = \frac{d}{dr}(V_0 + \sigma r + \frac{b}{r}) = -b/r^2 + \sigma. \tag{3.56}$$

3.3.3 Meson spectrum

In the continuum the mesons operators have the general form:

$$M(x) = \bar{\psi}_x^{\alpha a}\Omega^{ab}_{\alpha\beta}\psi(x)^{b\beta}, \tag{3.57}$$

which can be divided into five classes based on their properties under Lorentz transformation, see table 3.1.

Recall that the full Dirac spinor is collected from staggered fields on different sites of the hypercubes (Eqn. 3.29). The local staggered mesons can be found as:

$$M_{stagger}(y) = \sum_\eta \zeta(\eta)\bar{\chi}(2y+\eta)\chi(2y+\eta), \tag{3.58}$$

Table 3.1: Classes of mesons in the continuum.

Class	Field content	Example particle state	Corresponding $\mathcal{J}^{\mathcal{PC}}$
Scalar	$\bar{\psi}(x)\psi(x)$	a_0	0^{++}
Pseudoscalar	$\bar{\psi}(x)\gamma_5\psi(x)$	$\pi^0, \pi^{\pm}$	0^{-+}
Vector	$\bar{\psi}(x)\gamma_\mu\psi(x)$	ρ	1^{--}
Axialvector	$\bar{\psi}(x)\gamma_\mu\gamma_5\psi(x)$	a_1, b_1	$1^{++}, 1^{+-}$
Tensor	$\bar{\psi}(x)\sigma_{\mu\nu}\psi(x)$	A_2	2^{++}

where ζ are phase factors. Examples of the phase factor form for different class of meson operators can be found in table 3.2.

3.4 Formulation and simulation

Since we have constructed the action on lattice, the next step is to build the lattice gauge theory from the action. It is natural to formulate the lattice gauge theory from the Feynman path integral, because on lattice we have a countable number of degrees of freedoms and integrals can be calculated non-perturbatively via various Monte-Carlo procedures. The lattice Euclidean physics can be easily related to real Minkowski physics via standard Wick rotation. Thus we can start with the Euclidean partition function:

$$Z = \mathrm{Tr}[\exp(-S)] \tag{3.59}$$

$$= \int \mathcal{D}U\mathcal{D}\bar{\psi}\mathcal{D}\psi \exp[-S(\bar{\psi},\psi,U)]. \tag{3.60}$$

Table 3.2: Phase factors of staggered meson operators.

Class	Phase factor
Scalar	$\zeta(n) = 1$
Pseudoscalar	$\zeta(n) = (-1)^{n_1+n_2+n_3+n_4}$
Vector	$\zeta_\mu(n) = (-1)^{n_1+n_2+n_3+n_4-n_\mu}$
Axialvector	$\zeta_\mu(n) = (-1)^{n_\mu}$

The expectation value of any observable $\mathcal{O}$ can be calculated by

$$\langle\mathcal{O}\rangle = \frac{1}{Z}\mathrm{Tr}[\mathcal{O}\mathrm{exp}(-S)] \tag{3.61}$$

$$= \frac{1}{Z}\int \mathcal{D}U\mathcal{D}\bar{\psi}\mathcal{D}\psi\mathcal{O}(\psi,\bar{\psi},U)\mathrm{exp}[-S(\bar{\psi},\psi,U)]. \tag{3.62}$$

The path integral uses the gauge invariant Haar measure so there is no need to fix the gauge during integration.

In our calculations we use the hybrid Monte Carlo (HMC) algorithm. Our code is based in part on the MILC Collaborations's public lattice gauge theory software. We have modified this software to implement nHYP smearing, to add the adjoint plaquette term to the gauge action, and to exploit both even and old sub lattices to simulate eight flavors. During the course of our work, we also implemented a second-order Omelyan integrator [85] accelerated by an additional heavy pseudofermion field [86] and multiple time scales [87]. Our HMC trajectory length is typically one molecular dynamics time unit(MDTU), but in some cases can be as small as 0.5 MDTU or as large as 2.0 MDTU.

Chapter 4

Novel phase in SU(3) $N_f = 12$ system

4.1 Introduction

Lattice simulations cannot necessarily reach arbitrarily strong couplings: lattice artifacts can induce first-order transitions, which separate strongly-coupled lattice phases from the weak-coupling phase where the continuum limit is defined. This issue is especially important for systems around the lower edge of the conformal window, where very strong couplings may be required to distinguish IR conformality from chirally-broken dynamics. The Schrödinger functional calculation of Ref. [29] using unimproved staggered fermions encountered a clear first-order transition.

In this chapter we present a study of the $N_f = 12$ system at stronger couplings, reporting results for the phase diagram in the gauge coupling-fermion mass parameter space, at both zero and finite temperature. For most of the ensembles used in this work, we accumulate 1000 - 2000 molecular dynamics time units (MDTU), and measure the eigenvalues and meson spectrum on every tenth trajectory. Around the phase transitions we accumulate more than 10,000 MDTU for some ensembles. We find two transitions at finite tempereture that converge to two well-separated bulk phase transitions, consistent with what Refs. [32] observed using different staggered lattice actions. The general consistency of results observed with very different actions indicates that we are observing a robust feature of lattice gauge theories with many staggered fermions. Ref. [38] interpreted the second transition as a partial restoration of axial $U(1)_A$ symmetry, which is not consistent with our data below.

We identify a novel phase between the two bulk transitions where the single-site shift symmetry (S^4) of the staggered action is spontaneously broken ($\cancel{S^4}$). We study the novel phase by a variety of observables, including the meson spectrum, static potential, low-lying eigenvalues of the massless staggered Dirac operator, renormalization group blocked plaquette and Polyakov loop, and newly-developed order parameters. In terms of continuum symmetries, the $\cancel{S^4}$ phase possesses both chiral symmetry and axial $U(1)_A$ symmetry in the chiral limit, even though the Polyakov loop and static potential clearly indicate confinement. We argue that the $\cancel{S^4}$ phase is likely to be a purely lattice phase with no continuum limit, on the grounds that:

(1) Its combination of confinement and chiral symmetry is forbidden by the continuum 't Hooft anomaly matching condition;

(2) It is bounded by first-order bulk (zero-temperature) phase transitions;

(3) It appears in both 8- and 12-flavor systems, which we believe exhibit different infrared dynamics.

4.2 Phase structure

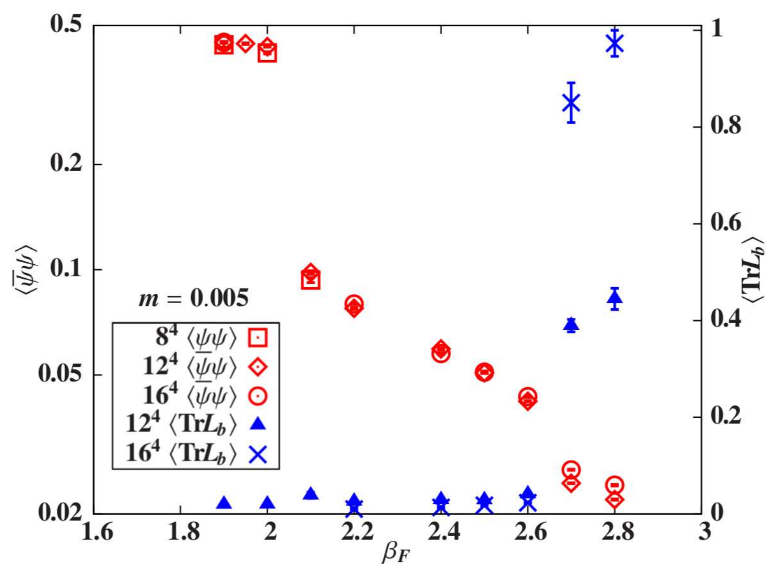

Figure 4.1: The chiral condensate $\langle\overline{\psi}\psi\rangle$ (on a log scale) and the blocked Polyakov loop $\langle \mathrm{Tr}L_b\rangle$ indicate two well-separated transitions at $m = 0.005$.

In the $m = 0$ chiral limit, confining and chirally broken systems with $N_f \geq 3$ flavors of fundamental fermions are expected to exhibit a first-order finite-temperature phase transition at which they become chirally symmetric and deconfined. A finite-temperature lattice system with fixed $N_t \ll L$ will undergo a phase transition at a critical coupling $\beta_F^{(c)}$. In the weak-coupling scaling region the renormalization group equation predicts the dependence of $\beta_F^{(c)}$ on N_t. In order for the theory to be confining and chirally broken at zero temperature, $\beta_F^{(c)} \to \infty$ as $N_t \to \infty$.

Zero-temperature systems with $N_t \geq L$ become deconfined and chirally symmetric when L is so small that the physics is volume-squeezed. This is a finite-volume effect and not a real phase transition, though it could be accompanied by a discontinuity. In few-flavor QCD-like systems no discontinuity is observed at zero temperature.

Much less is known about the finite-temperature behavior of IR-conformal systems. At strong enough coupling, lattice artifacts can create a confining, chirally broken phase on the lattice. This strong-coupling phase must be separated from the weak-coupling conformal phase by bulk (non-thermal) phase transition in the chiral limit. The bulk transition has to be a real infinite-volume transition, with the chiral condensate $\langle\overline{\psi}\psi\rangle$ serving as an order parameter in the chiral limit. While remnants of the finite-temperature phase transition can coexist with the bulk transition, the finite-temperature transitions must occur at stronger couplings than the bulk transition, and converge to the bulk transition as $N_t \to \infty$. This in principle gives a signal that distinguishes confining and conformal systems.

Refs. [30, 32, 38] investigated the 12-flavor SU(3) system and found indication for a bulk transition. Refs [32, 38] also discussed a second discontinuity in $\langle\overline{\psi}\psi\rangle$. Our investigations conform the existence of both bulk phase transitions, as illustrated in Fig. 4.1. In the chiral condensate we observe a clear discontinuity around $\beta_F \approx 2.0$ for $m = 0.005$ on zero-temperature $8^4, 12^4$ and 16^4 volumes. $\langle\overline{\psi}\psi\rangle$ has another, much smaller, discontinuity around $\beta_F \approx 2.65$, where the Polyakov loop, an observable related to confinement, shows a much stronger signal. Because the usual Polyakov loop becomes small and noisy as N_t increase, we consider an improved observable by measuring the Polyakov loop on renormalization group blocked lattices. This blocked Polyakov loop $\langle \mathrm{Tr} L_b \rangle$ has the same Z_3 symmetry as the standard one, and can also be thought of as an extended observable on the original, unblocked lattices.

The chiral condensate $\langle \overline{\psi}\psi \rangle$ has very little volume dependence across the phase transitions, consistent with bulk transitions. The apparent volume dependence of the blocked Polyakov loop is due to the different number of blocking steps performed: the 16^4 lattices are blocked three times with scale factor $s = 2$, while the 12^4 lattices can be blocked only twice.

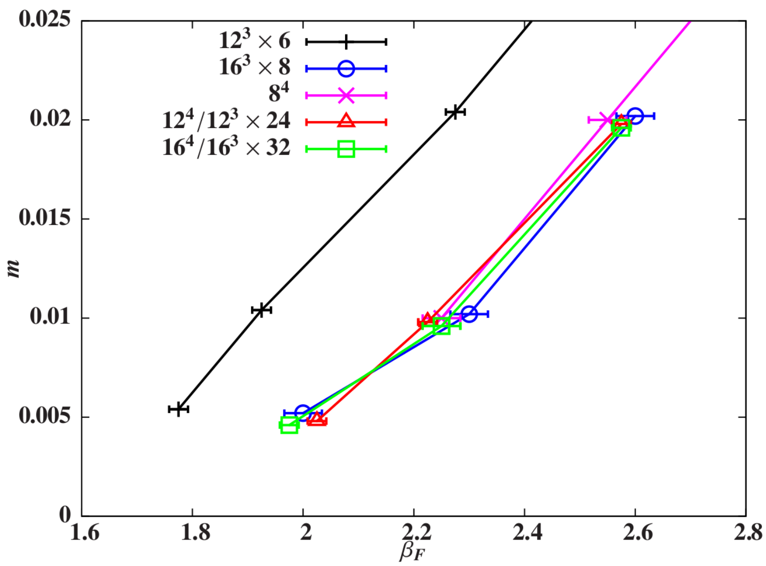

Figure 4.2: The stronger-coupling transitions in the $\beta_F - m$ plane at several temperatures and volumes, signaled by $\langle \overline{\psi}\psi \rangle$.

Fig. 4.2, 4.3 and 4.4 show how the locations of the two phase transitions depends on volume, temperature and fermion mass. In both cases, the transitions at finite temperature converge to zero-temperature bulk transitions where different observables show the same discontinuity on all volumes, up to small finite volume effects. Just like Refs. [30, 32, 38], we observe the stronger-coupling transitions to converge on smaller volumes than those that are needed for the weaker-coupling transitions to converge. We encountered long metastability between runs from hot and cold initial states at both transitions, especially on large volumes. These transitions are strongly first-order, and molecular dynamics evolution is not very effective flipping the system between phases. Mixed initial configurations helped to resolve the transition around $\beta_F \approx 2.65$ more accurately, but they

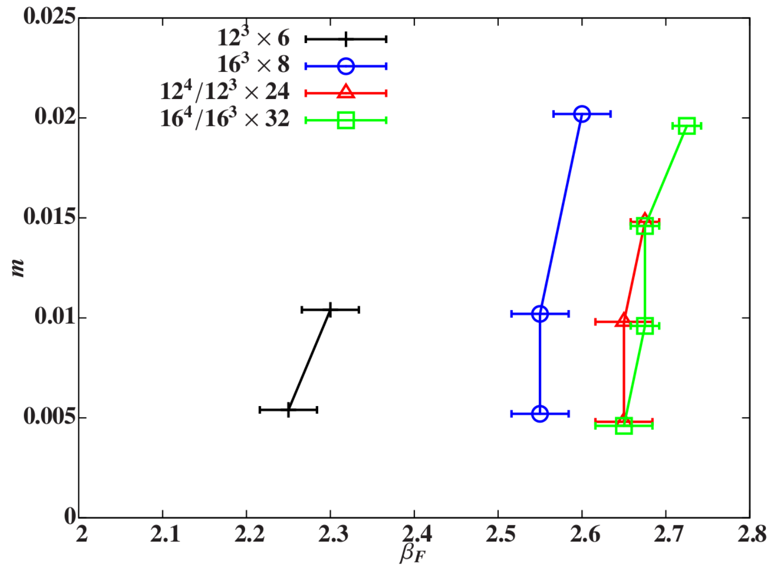

Figure 4.3: The weaker coupling transitions in the $\beta_F - m$ plane at several temperatures and volumes, signaled by $\langle \mathrm{Tr} L_b \rangle$.

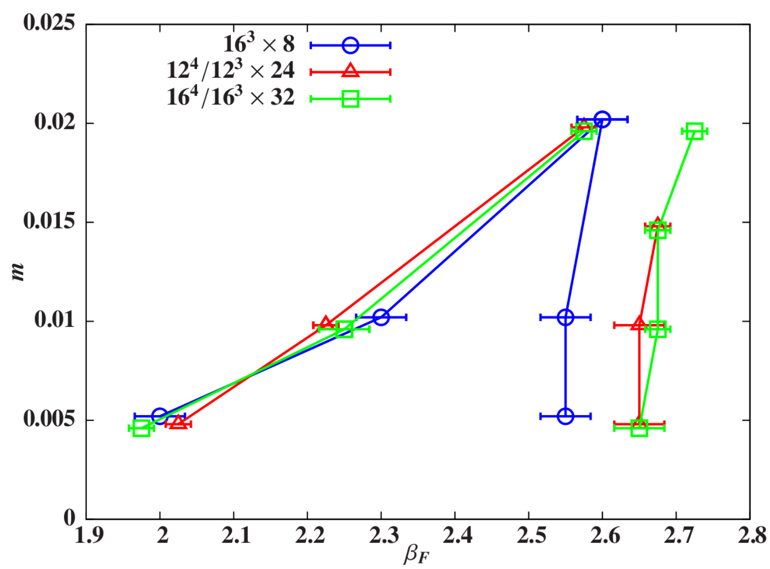

Figure 4.4: The two bulk transitions merge as m increase. Small vertical offsets distinguish the different volumes, and lines connect the points to guide the eye. The transitions are nearly identical on zero-temperature volumes, and the finite-temperature transitions appear to converge to these bulk transitions.

were less reliable at the transition around $\beta_F \approx 2$.

4.3 Single-site shift symmetry breaking

We identified two phases in Fig. 4.1 from the discontinuities in the chiral condensate and (blocked) Polyakov loop. This was possible as both phase transitions are first-order, and almost all observables show a discontinuity. However, neither $\langle\overline{\psi}\psi\rangle$ nor the Polyakov loop is a *bona fide* order parameter of the intermediate phase located between the two transitions. While the Polyakov loop is a good indicator of confinement, it is only an order parameter in the pure gauge theory, and does not distinguish between the intermediate and strong-coupling phases. The chiral condensate is an order parameter in the chiral limit only, and in that limit it likely vanishes in both the intermediate and weak-coupling phases.

There is no *a priori* guarantee that the intermediate phase is separated from the strong- and weak-coupling phases by true phase transitions. However, while investigating the phase diagram, we discovered that the single-site shift symmetry ("S^4") of the staggered fermion action is spontaneously broken in the intemediate ("$\cancel{S^4}$") phase. This ensures the existence of an order parameter characterizing the $\cancel{S^4}$ phase, and full separation of the phases.

The single-site shift symmetry of the staggered action takes form [88]

$$\chi(n) \to \xi_\mu(n)\chi(n+\mu), \quad \bar{\chi}(n) \to \xi_\mu(n)\bar{\chi}(n+\mu), \tag{4.1}$$

$$U_\mu(n) \to U_\mu(n+\mu), \tag{4.2}$$

where

$$\xi_\mu(n) = (-1)^{\sum_{\nu>\mu} n_\nu}. \tag{4.3}$$

This symmetry ensures that the chiral condensate $\langle\overline{\psi}\psi\rangle$ measured on even lattice sites is identical to that measured on odd sites, and the underlying gauge configurations exhibit the usual discrete translational symmetry. To our knowledge this is the first time that the breaking of this symmetry is observed.

Order parameters that are sensitive to this symmetry include the expectation value of the difference between neighboring plaquettes and that between neighboring links,

$$\Delta P_\mu = \langle \text{Re Tr}\Box_n - \text{Re Tr}\Box_{n+\mu} \rangle_{n_\mu \text{even}} \tag{4.4}$$

$$\Delta L_\mu = \langle \alpha_\mu(n)\bar{\chi}(n)U_\mu(n)\chi(n+\mu) - \alpha_\mu(n+\mu)\bar{\chi}(n+\mu)U_\mu(n+\mu)\chi(n+2\mu) \rangle_{n_\mu \text{even}} \tag{4.5}$$

where $\alpha_\mu(n)$ is the usual staggered phase factor given in Eqn. 3.25, Re Tr$\Box_n$ is the real trace of the plaquette originating at site n, and the expectation value $\langle ... \rangle_{n_\mu \text{even}}$ is taken only over cites whose μ component is even. In the intermediate phase these operators develop non-zero expectation values in one or more directions μ. Occasionally the direction of the symmetry breaking changes, rotating in space.

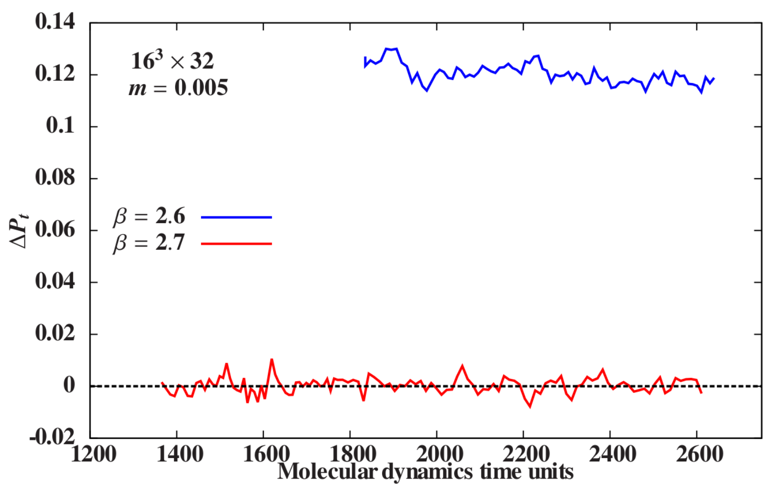

Figure 4.5: (a) The plaquette difference ΔP_t (Eqn. 4.4) measured on $16^3 \times 32$ volumes in both the $\not{S}^4$ phase ($\beta_F = 2.6,\ m = 0.005$) and the weak-coupling phase($\beta_F = 2.7,\ m = 0.005$), as functions of the molecular dynamics time.

Fig. 4.5 and 4.6 show the two order parameters in the intermediate ($\beta_F = 2.6,\ m = 0.005$) and the weak-coupling($\beta_F = 2.7,\ m = 0.005$) phases as functions of the molecular dynamics time on $16^3 \times 32$ volumes. At $\beta_F = 2.7$ the order parameters do not develop a none-zero expectation value in any direction. The order parameters also vanish in the strong-coupling phase, though we do not include that data here. The single-site shift symmetry is broken only in the intermediate phase. The order parameters, when non-vanishing, have only small dependence on the volume.

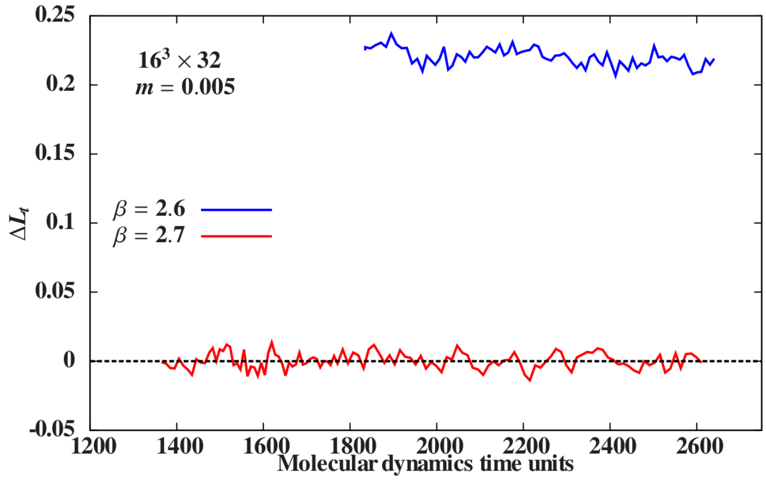

Figure 4.6: the link difference ΔL_t (Eqn. 4.5) measured on $16^3 \times 32$ volumes in both the $\cancel{S^4}$ phase ($\beta_F = 2.6,\ m = 0.005$) and the weak-coupling phase($\beta_F = 2.7,\ m = 0.005$), as functions of the molecular dynamics time.

It is important to note that the single-site shift symmetry is an exact symmetry of the action even at finite fermion mass. It is broken only spontaneously. Both ΔP_μ of Eqn. 4.4 and ΔL_μ of Eqn. 4.5 are nonzero when the symmetry is broken and vanish when it is preserved. The $\not{S}^4$ phase must be separated by true phase transitions from the strong- and weak-coupling phases where both order parameters vanish.

4.4 Eigenvalue Spectrum

The results we discussed in Section 4.2 suggest that the transition at stronger coupling is related to chiral symmetry breaking, while the transition at weaker coupling is related to confinement. We will consider confinement in the next section, while in this section we investigate the chiral properties of the phases. Finite fermion mass explicitly breaks chiral symmetry, and extrapolating the chiral condensate to the $m = 0$ chiral limit can be a difficult task. Here we use the eigenvalue distribution of the Dirac operator to study chiral symmetry.

The spectrum of the Dirac operator of chirally broken systems contains a wealth of information. When the eigenvalue distribution is compared to random matrix theory (RMT), it predicts the chiral condensate and gives information about the lattice artifacts of the simulations. There is no comparable prediction for conformal systems, nevertheless the volume scaling and the level spacing of consecutive eigenvalues might be related to the mass scaling exponent of the fixed point that governs the infrared dynamics [48, 89]. In next chapter we will conduct a systematic exploration on the scaling of Dirac eigenmodes and its relation to the mass anomalous dimension in both chirally broken and conformal systems in the weak coupling phases. Here we only concentrate on the different behaviors in the intermediate and the weak-coupling phase.

The 12-flavor staggered action is local and describes a well-defined statistical system. In the following analysis we will investigate general questions of scaling for this system. We will not compare our data to RMT predictions, and our analysis will not be sensitive to taste symmetry, or its breaking.

In this pilot study we calculate the 12 lowest-lying eigenvalues of the staggered Dirac operator

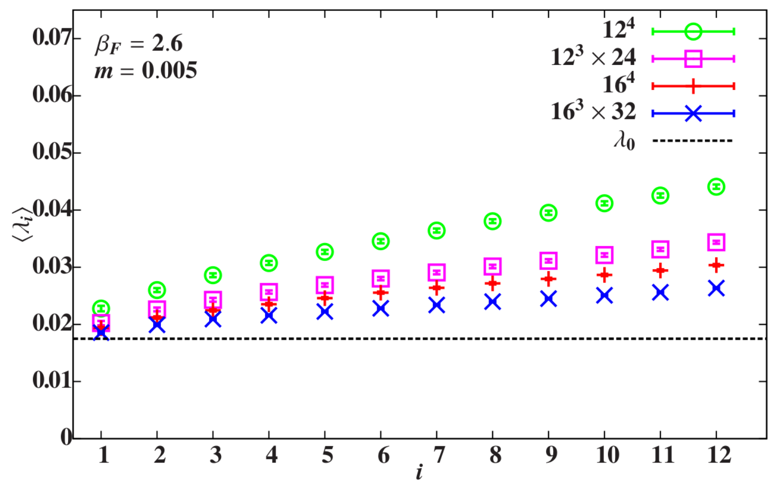

Figure 4.7: The low-lying eigenvalues $\langle\lambda_i\rangle$ in the $\cancel{S^4}$ phase ($\beta_F = 2.6$) for $m = 0.005$ on the four volumes $12^4, 12^3 \times 24, 16^4$ and $16^3 \times 32$. The dashed line shows the soft edge $\lambda_0 = 0.0175(5)$ found in the fit plotted in Fig. 4.9.

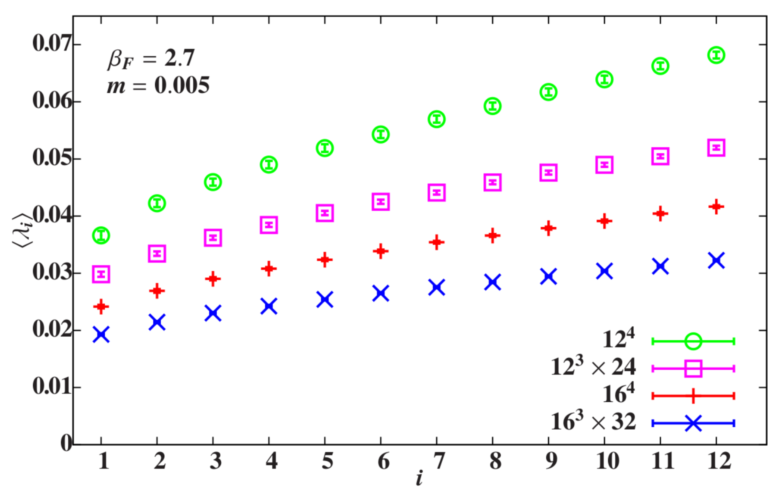

Figure 4.8: The low-lying eigenvalues $\langle\lambda_i\rangle$ in the weak-coupling phase ($\beta_F = 2.7$), for $m = 0.005$ on the four volumes $12^4, 12^3 \times 24, 16^4$ and $16^3 \times 32$.

on volumes 12^4, $12^3 \times 24$, 16^4 and $16^3 \times 32$ in both the $\not{S}^4$ and weak-coupling phases. In principle one should separate the different topological sectors before averaging the eigenvalues, but all of the configurations we analyzed appear to be in the zero-topology sector. Fig. 4.7 and 4.8 illustrate the volume dependence and the level spacing of the lowest-lying eigenvalues in the $\not{S}^4$ and weak-coupling phases. Our gauge configurations are too coarse for the eigenvalues to show the four-fold degeneracy expected in the continuum limit of staggered fermions. Additional HYP smearing steps can remove enough of the ultraviolet fluctuations to reveal the expected degeneracy, but this is not what the dynamical fermions see in the simulations, and we do not pursue this direction.

In the infinite-volume limit the basic quantity is the eigenvalue density $\rho(\lambda)$. In the chiral limit the density of low-lying eigenvalues is expected to scale as

$$\rho(\lambda) \propto (\lambda - \lambda_0)^\alpha, \tag{4.6}$$

where the parameter $\lambda_0 \geq 0$ allows the possibility of a soft edge [90, 91, 92]. In a chirally broken system $\rho(0) \neq 0$, implying $\lambda_0 = 0$ (the "hard edge") and $\alpha = 0$. In a conformal system $\lambda_0 = 0$, and α is related to the scale dependent mass anomalous dimension.

Although the density $\rho(\lambda)$ is only well defined in the infinite-volume limit, the functional form of Eqn. 4.6 can be used to analyze the spacing between discrete eigenvalues in a finite volume. Denoting the finite-volume eigenvalues as λ_i for $i = 1, 2, ...$, we can write the cumulative eigenvalue density as

$$\int_{\tilde{\lambda}}^{\tilde{\Lambda}} \rho(\lambda) d\lambda = \lim_{V \to \infty} (\frac{n-m}{V}), \tag{4.7}$$

where $\lambda_n = \tilde{\Lambda}$ and $\lambda_m = \tilde{\lambda}$. Using Eqn. 4.6 this leads to

$$\lambda_n - \lambda_0 \propto (\frac{n - x_0}{V})^{\frac{1}{\alpha+1}} [1 + \mathcal{O}(V^{-1})], \tag{4.8}$$

where we combined m/V and $(\lambda_m - \lambda_0)^{\alpha+1} \propto (V^{-1})$ in the parameter x_0/V. The proportionality constant and x_0 can depend on the lattice geometry, while λ_0 and α are universal.

Fig. 4.7 shows our results for the low-lying eigenvalues in the $\not{S}^4$ phase at $\beta_F = 2.6, m = 0.005$. In this plot we include a dashed line showing the soft edge $\lambda_0 = 0.0175(5)$ predicted by our global

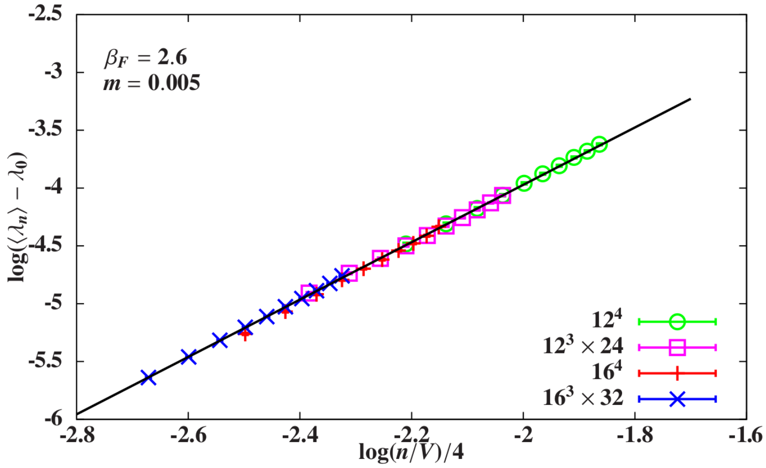

Figure 4.9: Scaling of the low-lying eigenvalues in the $\not{S}^4$ phase ($\beta_F = 2.6$) for $m = 0.005$ on the four volumes $12^4, 12^3 \times 24, 16^4$ and $16^3 \times 32$. The soft edge $\lambda_0 = 0.0175(5)$.

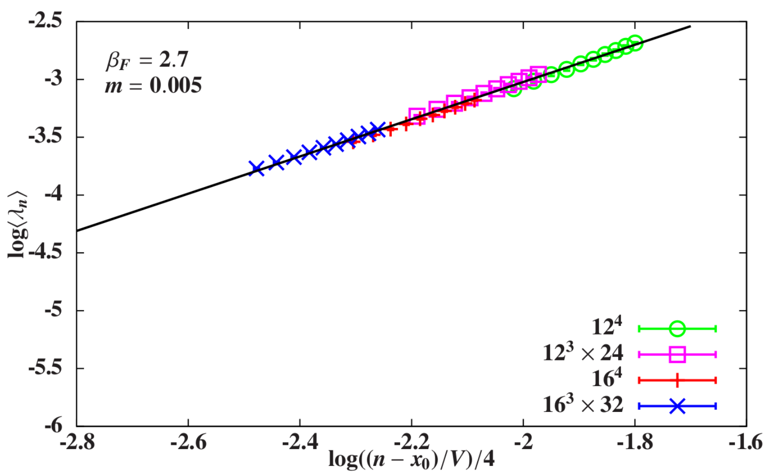

Figure 4.10: Scaling of the low-lying eigenvalues in the weak-coupling phase ($\beta_f = 2.7$) for $m = 0.005$ on the four volumes $12^4, 12^3 \times 24, 16^4$ and $16^3 \times 32$. $\lambda_0 = 0$ but $x_0 \sim 3$.

fit to Eqn. 4.8 using all four volumes. Fig. 4.9 shows the result of this global fit, which does not depend on the aspect ratios of the lattices. The dependence on x_0 is weak, and we fix $x_0 = 0$.

A non-vanishing soft edge is rather unusual. In finite-temperature systems with N_t fixed, $L \to \infty$, Ref. [90] observed $\lambda_0 > 0$ in the chirally broken phase, but in infinite volume neither chirally broken nor conformal systems are expected to have a soft edge. Through the Banks-Casher relation [93]

$$\langle \overline{\psi}\psi \rangle \propto m \int_0^\infty \frac{\rho(\lambda) d\lambda}{\lambda^2 + m^2}, \tag{4.9}$$

a soft edge implies that the chiral condensate $\langle \overline{\psi}\psi \rangle$ vanishes in the chiral limit $m = 0$. With a soft edge, $\rho(\lambda) = 0$ for $0 \leq \lambda < \lambda_0$ as well as for all λ larger than the spectral range of the Dirac operator, so that the integral in Eqn. 4.9 remains finite while $m \to 0$.

In addition, a soft edge excludes the scenario in which $\langle \overline{\psi}\psi \rangle = 0$ but chiral symmetry is broken in the $\cancel{S^4}$ phase by a nonzero four-fermion condensate. As discussed by Ref. [94, 95, 96], this could result from the chiral symmetry breaking pattern

$$SU(N_f) \times SU(N_f)_A \to SU(N_f)_V \times Z_{N_f} \tag{4.10}$$

where the custodial Z_{N_f} symmetry forces $\langle \overline{\psi}\psi \rangle = 0$. The four-fermion condensate considered in Ref. [96] is related to the difference of scaler and pseudoscalar susceptibilities $\omega = \chi_P - \chi_S$ where

$$\chi_P = \frac{1}{V} \int d^4x d^4y \langle \bar{\chi}\tau^j i\gamma_5 \chi(x) \bar{\chi}\tau^j i\gamma_5 \chi(y) \rangle \tag{4.11}$$

$$\chi_S = \frac{1}{V} \int d^4x d^4y \langle \bar{\chi}\tau^j \chi(x) \bar{\chi}\tau^j \chi(y) \rangle \tag{4.12}$$

and τ^j is a flavor generator. The U$(1)_A$-noninvariant ω parameter can be expressed in terms of the eigenvalue density as [97]

$$\omega = 4m^2 \int_0^\infty \frac{\rho(\lambda) d\lambda}{(\lambda^2 + m^2)^2}. \tag{4.13}$$

Just as for Eqn. 4.9, ω vanishes in the chiral limit if the eigenvalue density has a soft edge, so the symmetry breaking scenario of Eqn. 4.10 is not consistent with our data in the $\cancel{S^4}$ phase. The soft edge is a dimensional parameter, but it is not clear what infinite-volume physical quantity it corresponds to. Better understanding of the symmetry breaking mechanism could shed light on this problem.

The eigenvalue spectrum in the weak-coupling phase is more conventional. Fig. 4.8 shows the low-lying eigenvalues in this phase at $\beta_F = 2.7$, $m = 0.005$. The global fit to Eqn. 4.8 predicts $\lambda_0 = 0$ but a non-vanishing $x_0 \sim 3$ (see Fig. 4.10). Volumes with different aspect ratios prefer slightly different x_0 values and proportionality constants.

4.5 Static potential and meson spectrum

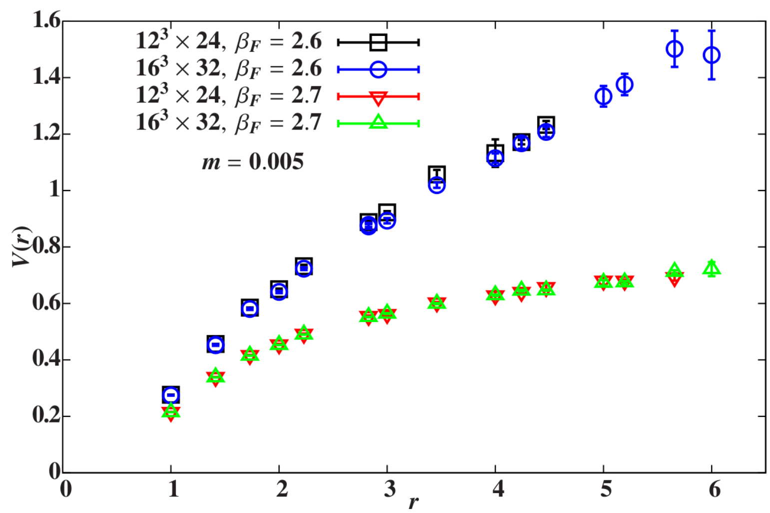

Figure 4.11: The HYP-smeared static potential in the $\not{S}^4$ phase at $\beta_F = 2.6$ and the weak-coupling phase at $\beta_F = 2.7$.

In this section we explore the static potential and meson spectrum in the $\not{S}^4$ phase, contrasting these results with the same observables in the weak coupling phase. Although $\langle \mathrm{Tr} L_b \rangle$ shows a clear signal in Fig. 4.1, the Polyakov loop is not an order parameter in the presence of dynamical fermions. The static potential is a more reliable indicator of confinement. In Fig. 4.11 we contrast the HYP-smeared static potential [78] measured on each side of the transition, at $\beta_F = 2.6$ and 2.7 on $12^3 \times 24$ and $16^3 \times 32$ volumes with $m = 0.005$.

The potential at $\beta_F = 2.6$ is consistent with confinement, with string tension $\sigma = 0.20(1)$ and

Sommer parameter $r_0/a = 2.67(4)$ in lattice units. We obtain similar values at other masses and couplings within the $\mathcal{S}^4\!\!\!\!/$ phase. The potential is almost identical on $12^3 \times 24$ and $16^3 \times 32$ volumes, and the small r_0 suggests that there will be no qualitative change on larger volumes that we are currently investigating. These results indicate confinement with a fairly short gauge correlation length. On the other hand, the potential at $\beta_F = 2.7$ is coulombic and cannot be fitted consistently with a linear term. The lack of volume dependence implies either vanishing string tension and conformality or an intrinsic confinement scale that can only be observed on larger lattice volumes.

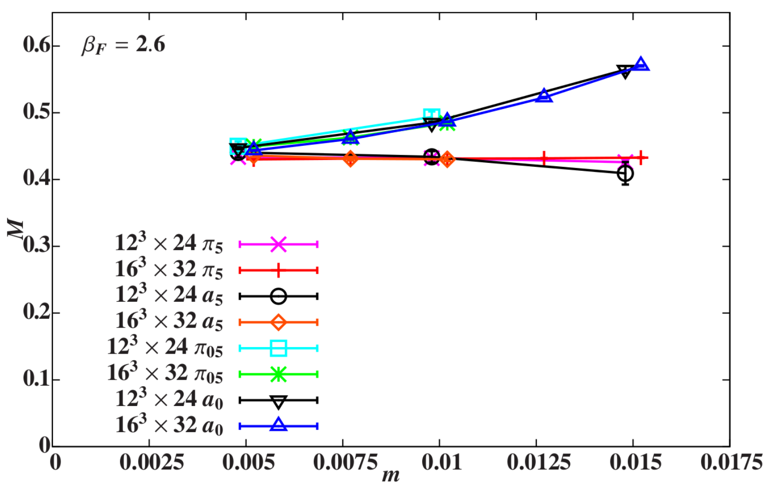

Figure 4.12: The masses of the Goldstone π_5, its "a_5" parity partner, the π_{05} pseudoscalar and the a_0 scalar in the $\mathcal{S}^4\!\!\!\!/$ phase at $\beta_F = 2.6$ on $12^3 \times 24$ and $16^3 \times 32$ lattices.

The meson spectrum at $\beta_F = 2.7$ is also consistent with a small-volume deconfined system. Fig. 4.13 shows the Goldstone γ_5 pseudoscalar (π_5), the pseudoscalar and the scalar components of the $\gamma_0\gamma_5$ channel (π_{05} and a_0) and the $\gamma_i\gamma_5$ pseudoscalar (π_{i5}) versus fermion mass m. We observe significant volume dependence in the scalar become degenerate at small m, consistent with parity doubling. The π_{05} meson becomes heavier than the scalar at $m = 0.005$, where it is degenerate with the π_{i5} state. (Our data do not allow precise results for these states on $12^3 \times 24$ at $m < 0.01$.) Overall our meson spectrum results at $\beta_F = 2.7$ are dominated by finite-volume effects, and do not provide clear information about the IR dynamics of the 12-flavor model. With the computational resources available to us, we cannot compete with the large-volume spectral study of Ref. [98].

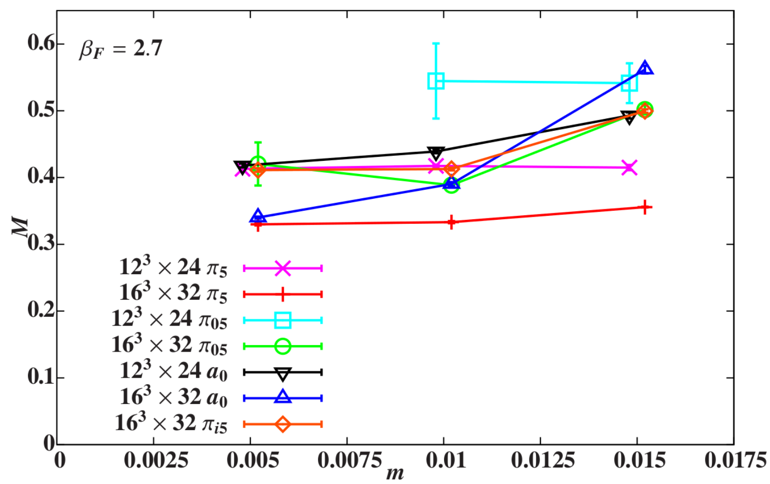

Figure 4.13: The masses of the Goldstone π_5, the π_{05} pseudoscalar, the a_0 scalar and π_{i5} vector in the weak-coupling phase at $\beta_F = 2.7$ on $12^3 \times 24$ (except π_{i5}) and $16^3 \times 32$ lattices.

Our goal in investigating the static potential and meson spectrum in the weak-coupling phase is to contrast these results in the $\not{S}^4$ phase, where we observe several interesting differences. Our results for the pseudoscalar and scalar spectrum at $\beta_F = 2.6$ are summarized in Fig. 4.13. In the $\not{S}^4$ phase we find that the pion has a parity partner ("a_5") in the γ_5 channel, a state that is forbidden in QCD-like systems. The masses measured on $16^3 \times 32$ and $12^3 \times 24$ volumes are indistinguishable in the $\not{S}^4$ phase: the finite volume corrections are negligible, consistent with the small correlation length indicated by the static potential. The parity partner states both in the γ_5 and $\gamma_0\gamma_5$ channels are degenerate. The γ_5 states are largely independent of the fermion mass m while the $\gamma_0\gamma_5$ mesons' masses increase steadily with increasing m. The data indicate that all four mesons might be degenerate in the chiral limit. However, the π_{05} mass again proved difficult to extract, and our statistics and volumes do not allow precise results for the π_{05} at $m > 0.01$.

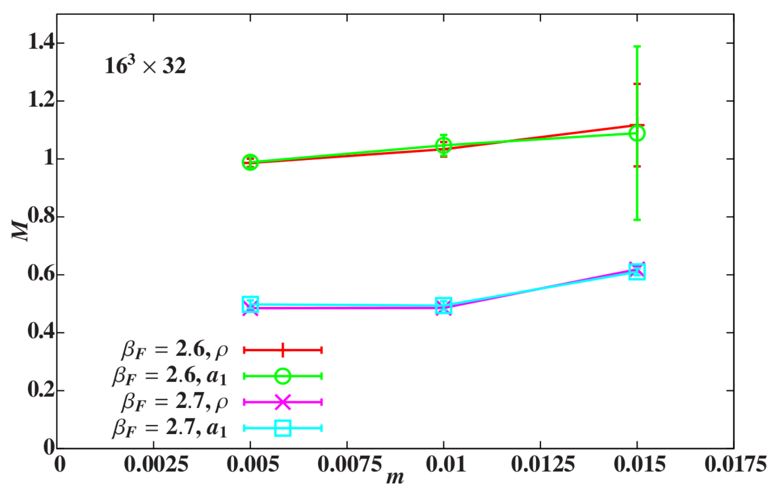

Figure 4.14: The ρ and a_1 are degenerate in both the weak-coupling phase at $\beta_F = 2.7$ as well as the $\not{S}^4$ phase at $\beta_F = 2.6$. At $\beta_F = 2.7$ this degeneracy is a familiar effect. At $\beta_F = 2.6$, it is consistent with our observation of chiral symmetry in the eigenvalue spectrum.

In Fig. 4.14 we show the masses of the vector meson ρ and its parity partner a_1 measured on $16^3 \times 32$ volumes in both the $\not{S}^4$ phase at $\beta_F = 2.6$ and the weak-coupling phase at $\beta_F = 2.7$. At both of these couplings, the ρ and a_1 are degenerate for all $m \leq 0.015$. In the deconfined weak-coupling phase, this parity doubling is a familiar effect. In the confining $\not{S}^4$ phase, however, such

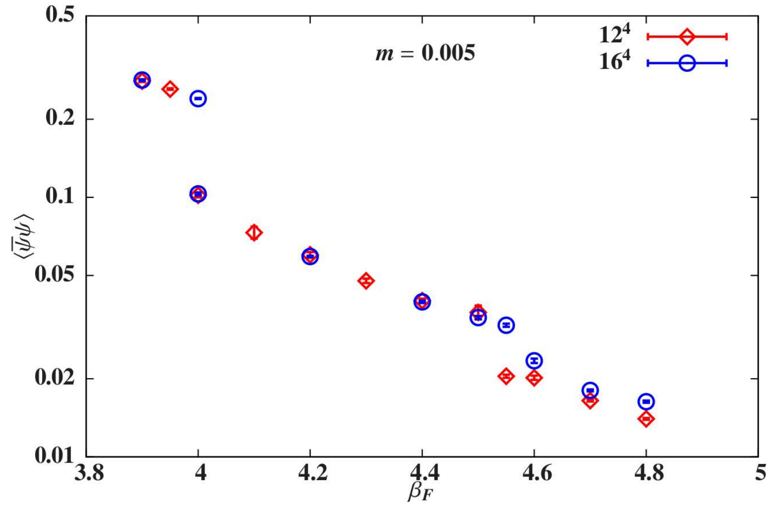

Figure 4.15: The chiral condensate $\langle\overline{\psi}\psi\rangle$ (on a log scale) in the $N_f = 8$ flavor system at $m = 0.005$ on 12^4 and 16^4 lattices. The phase between the two first order transitions is an $\cancel{S^4}$ phase like that we observe for $N_f = 12$.

spectral properties are unusual. The $\rho - a_1$ parity doubling we observe in Fig. 4.14 is inconsistent with the spectrum associated with the chiral symmetry breaking pattern of Eqn. 4.10. Combined the low-lying Dirac spectrum in this phase, the degeneracy of the parity partners in the meson spectrum implies that the intermediate phase is confining but chirally symmetric. The continuum 't Hooft anomaly matching condition does not permit the existence of such a phase, suggesting that the novel phase we observe does not exist in the continuum.

4.6 The 8-flavor case

Finite-temperature transitions converging to a bulk transition could signal that the continuum weak-coupling phase is conformal in the infrared. However, because we observe two bulk transitions bounding an intermediate phase with unusual properties, we must consider the possibility that our results are due to lattice artifacts. With Wilson fermions the existence of a lattice artifact phase, first proposed by Aoki [79], is well known. Ref. [99] argues that an Aoki-like phase might exist with staggered fermions if more than a single four-taste multiplet is considered. We investigate this possibility through additional studies with $N_f = 8$ flavors.

Fig 4.15 shows the $N_f = 8$ chiral condensate $\langle\overline{\psi}\psi\rangle$ at $m = 0.005$ on 12^4 and 16^4 volumes. We observe the same phases as with $N_f = 12$ flavors. On both volumes there are two first-order transitions at approximately volume-independent gauge couplings. The phase in between has the same properties as the $\not{S}^4$ phase with 12-flavors. It breaks single-site shift symmetry as shown by the non-zero expectation values of the two order parameters ΔP_μ (Eqn. 4.4) and ΔL_μ(Eqn. 4.5). The Dirac operator eigenvalue spectrum has a soft edge, the static potential has a non-vanishing string tension, and the meson spectrum shows parity doubling. Yet it is generally believed that the $N_f = 8$ flavor system is below the conformal window [29, 31, 48, 51, 52].

The fact that an $\not{S}^4$ phase exists with 8 flavors implies that this phase and its two corresponding bulk transitions do not necessarily imply IR conformality in the continuum. The infrared behavior of the weak-coupling phase is independent of the $\not{S}^4$ phase and has to be studied by other means.

4.7 Conclusion

Our investigations of the phase diagram of the 12-flavor SU(3) model have identified a novel phase with unusual properties. At small masses this phase lies in between the usual confining, chirally broken lattice strong-coupling phase and the weak-coupling phase that is governed by the perturbation gaussian fixed point and possibly an infrared fixed point. The two first-order phase transitions separating these three phases get closer together with increasing fermion mass. At some mass value the two transitions merge and eventually turn into a crossover. The intermediate phase forms a packet in between the strong and weak-coupling phases at small fermion masses.

In this chapter we studied the intermediate phase and contrasted it with the weak-coupling phase using several observables. The chiral condensate $\langle\overline{\psi}\psi\rangle$ and blocked Polyakov loop gave us first glimpse of the phase structure, and suggested that the transition at stronger coupling is related to chiral symmetry breaking, while the transition at weaker coupling is related to confinement. Our investigation led us to two operators, ΔP_μ (Eqn. 4.4) and ΔL_μ (Eqn. 4.5), that serve as order parameters of the intermediate phase. Both of these order parameters are sensitive to the single-site shift symmetry (S^4) of the staggered fermions, a symmetry that is exact at the level of the lattice action. Since these order parameters develop non-zero expectation values in the intermediate phase, but vanish in both the strong- and weak-coupling phases, we conclude that the intermediate phase spontaneously breaks single-site shift symmetry, $\not{S}^4$. Since the single-site shift symmetry is exact even at finite fermion mass, the $\not{S}^4$ phase must be separated by real phase transitions from both the strong- and weak-coupling phases.

We used the spectrum of the Dirac operator to study the chiral properties of the phases. In the $\not{S}^4$ phase we found evidence for a soft edge, implying chiral symmetry. In the weak-coupling phase the eigenvalue spectrum is consistent with both conformal and volume-squeezed confining scenarios.

The static potential showed that the $\not{S}^4$ phase is confining with a small lattice correlation length, while in the weak-coupling phase on our relative small volumes the potential was only coulombic. These results are consistent with the signal from the (blocked) Polyakov loop. The meson spectrum in both phases indicated parity doubling at light fermion mass. However, in the $\not{S^4}$ phase we observed very little volume dependence, yet we found that all mesons remained massive in the chiral limit. The parity doubling in the weak coupling phase was accompanied by strong volume dependence and could also be consistent with both conformal and confining scenarios.

We presented preliminary data showing that the $\not{S^4}$ phase is present with 8 flavors as well, suggesting that this phase is not related to conformal infrared dynamics. Our findings lead us to believe that the $\not{S^4}$ phase is a lattice artifact of the staggered fermions [99]. Since the single-site shift symmetry is closely related to the fermion staggering and taste breaking, it is most likely that the origin of the $\not{S^4}$ phase is in the fermionic sector. To probe the infrared dynamics we need other methods to study the weak-coupling phases. In the next chapter we will present our method to extract the scale-dependent mass anomalous dimension from the Dirac eigenmode numbers.

Chapter 5

Dirac Eigenmodes

5.1 Introduction and Overview

The eigenmodes of the Dirac operator contain a wealth of information about the dynamics of lattice systems. Eigenvalue density $\rho(\lambda)$ of the Dirac operator is related to the condensate through Banks-Casher relation [93]:

$$\Sigma(m_q) = \int \rho(\lambda) d\lambda \frac{m_q}{\lambda^2 + m_q^2}. \tag{5.1}$$

If the theory is chirally broken, we have

$$\Sigma = \lim_{\lambda \to 0} \pi\rho(\lambda) \tag{5.2}$$

in the infinite-volume chiral limit [100, 101]. This relation allows the determination of Σ at modest computational cost[102, 103, 104, 105]. While one can search for IR conformality by checking whether distributions of low-lying eigenmodes deviate from RMT predictions [48, 106], this approach is complicated by the lack of comparably rigorous theoretical predictions for eigenvalue distributions in IR-conformal systems. An alternative proposed by Ref. [89] is to investigate the finite-size scaling of individual eigenmodes, which is related to the scheme-independent mass anomalous dimension γ_m^* at the IR fixed point. General critical scaling in conformal systems suggests:

$$\begin{aligned} \Sigma(m_q) &\sim m_q^\alpha, & (5.3) \\ \rho(\lambda) &\sim \lambda^\alpha, & (5.4) \end{aligned}$$

for small m_q and λ .

The integral of the eigenvalue density, namely, the eigenmode number

$$\nu(\lambda) = V \int_{-\lambda}^{\lambda} \rho(\omega) d\omega, \tag{5.5}$$

is a more robust and reliable observable due to its renormalization group (RG) invariance [107, 108]. Ref. [107] used a stochastic method to evaluate the mode number on a set of 2-flavor SU(3) p-regime configurations in an extended λ range. The slope of $\nu(\lambda)$ gives the spectral density, which is extrapolated to the chiral limit to determine Σ using the Banks-Casher relation. In conformal theories the scaling of of the mode number can be related to the scheme-independent mass anomalous dimension at the IR fixed point through its RG invariance.

Our unique contribution to this picture is the discovery of the scale-dependence of the mass anomalous dimension. We investigate the mode number in $\lambda \to 0$ infrared limit as well as across a wide range of energy scales from the infrared to the ultraviolet where $\nu(\lambda) \propto \lambda^4$ is expected [109]. At intermediate λ the behavior of the mode number interpolates between these two extremes, with an exponent that is related to the scale-dependent anomalous dimension γ_m. We show how $\gamma_m(\lambda)$ can be determined from lattice simulations of both QCD-like and infrared-conformal systems.

The approach we propose is very general and can be used with any lattice model, offering a new way to investigate the scale dependence of both IR-conformal and chirally broken systems. We review the energy dependence of the mass anomalous dimensions and our method to extract it from lattice data in section 5.2, and then discuss potential systematic effects in 5.4. In particular, since the results are obtained from lattice calculations carried out with very light or massless staggered fermions, we carefully consider the question of finite-volume effects. We show how combining different volumes allows us to access volume-independent physics.

We apply our proposal on SU(3) lattice gauge theories with N_f = 4, 8, 12 and 16 light or massless staggered fermions. We first test our method on the well-known QCD-like $N_f = 4$ system. In the QCD-like 4-flavor system we are able to follow the evolution of the system from the perturbative UV limit to the onset of chiral symmetry breaking in the IR. Our results indicate that the $N_f = 4$ simulations are in the scaling regime of the gaussian fixed point at $g^2 = 0$. This test shows that our method to extract the anomalous dimension is reliable even on very small physical volumes with vanishing fermion masses. Our results for the $N_f = 12$ system are very different from the $N_f = 4$ case. In the infrared, all of our 12-flavor results with different gauge couplings appear to approach a unique value as λ decreases. We interpret this behavior as indication of infrared conformality and identify the common $\lambda \to 0$ limit as the scheme-independent mass anomalous dimension $\gamma_m^\star \approx 0.235(27)$ that characterizes the conformal theory at the IRFP. Our results on the $N_f = 16$ system, which is believed to be IR-conformal, is similar to our $N_f = 12$ system, and further supports the IR-conformality of the $N_f = 12$ system. Finally, our 8-flavor results do not indicate QCD-like, asymptotically free UV behavior, but they also differ compared to the 12-flavor system. We find the 8-flavor system the hardest case to interpret. At the least we observe the walking behavior of the mass anomalous dimension across large energy scales at different gauge couplings.

In the early stage of our study we performed direct calculations of Dirac eigenvalues, and counted the eigenmode number under chosen cutoff during fit. For $N_f = 12$ system we found the severe finite volume effects at weak couplings calling for calculating more eigenmodes on large lattice volumes, which become computationally impractical from direct calculations. We later develop the stochastic estimator of the Dirac eigenmode following refs. [107, 110], and managed to reach large enough λ on large lattice volumes. The details of the stochastic estimator is described in section 5.32.

5.2 Mass anomalous dimension from the mode number

Conformal systems are chirally symmetric, so the eigenvalue density $\rho(\lambda)$ vanishes at $\lambda = 0$ in the infinite volume, zero mass limit. The simplest scaling form valid for small λ is $\rho(\lambda) \propto \lambda^\alpha$, leading to the RG-invariant mode number

$$\nu(\lambda) = V \int_{-\lambda}^{\lambda} \rho(\omega) d\omega \propto V \lambda^{1+\alpha}. \tag{5.6}$$

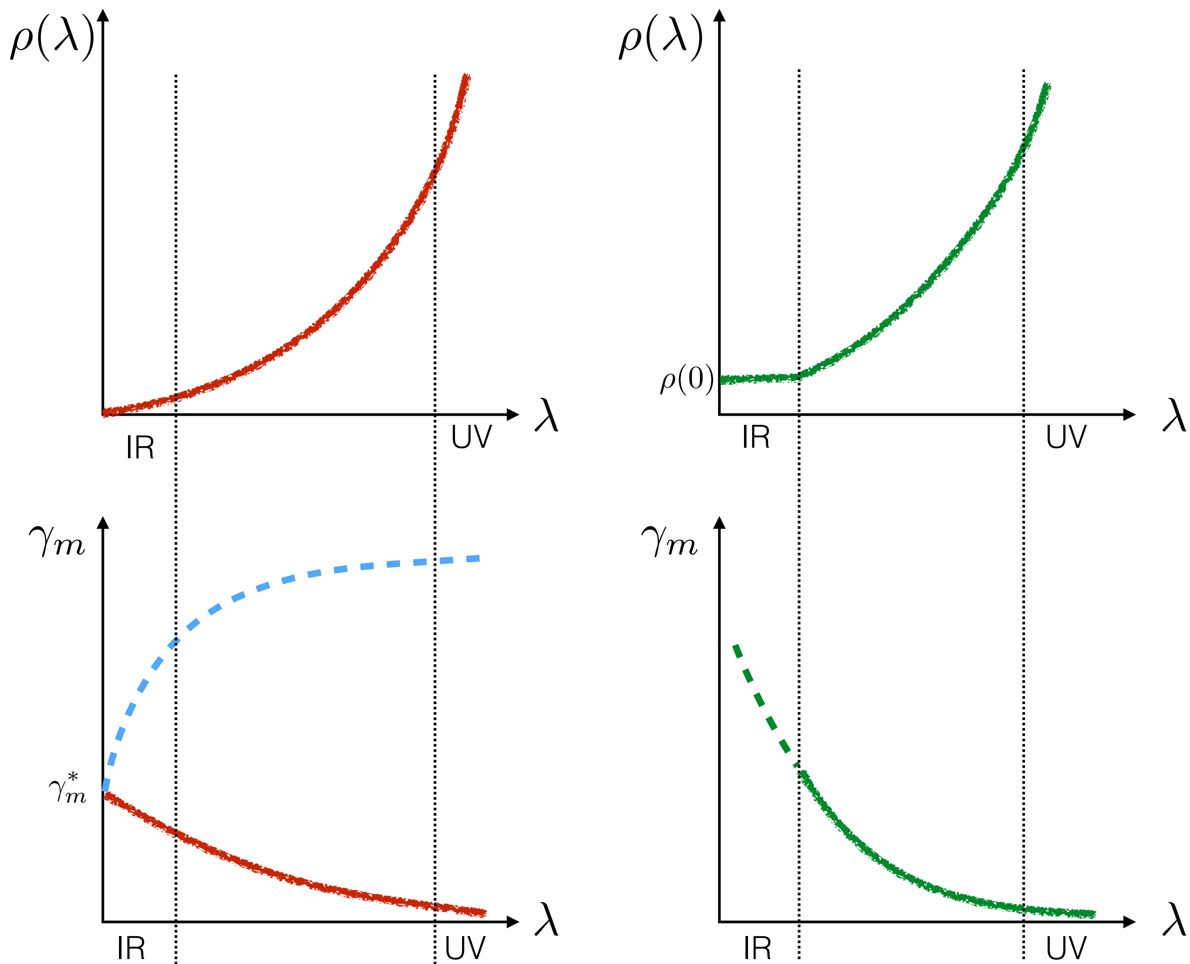

Figure 5.1: Cartoons of eigenvalue densities $\rho(\lambda)$ and scale-dependent mass anomalous dimension γ_m in in IR-conformal (left) and chirally broken (right) continuum systems. In the IR-conformal systems (left), on the weak coupling side of the IRFP γ_m grows toward γ_m^* at the IR fixed point as $\lambda \to 0$, while on the strong coupling we conjecture γ_m increases with energy as suggested by the dashed blue line, motivated from a backward flow in the gauge coupling. In the chirally broken systems (right), spontaneous chiral symmetry breaking produces $\rho(0) \propto \langle\bar{\psi}\psi\rangle \neq 0$ in the infrared, which does not follow the scaling form $\rho(\lambda) \propto \lambda^{\alpha(\lambda)}$. In both systems, asymptotic freedom predicts $\gamma_m \to 0$ as $\lambda \to \infty$ in the UV.

Under a renormalization group transformation with the scale factor s, the volume becomes

$$V \to s^4 V \tag{5.7}$$

while the eigenvalues rescale as

$$\lambda \to \lambda / s^{1+\gamma_m^*} \tag{5.8}$$

in the infrared limit, where γ_m^* is the scheme-independent mass anomalous dimension at the IR fixed point. Due to the RG invariance of the mode number, we have

$$V\lambda^{1+\alpha} = s^4 V (\lambda / s^{1+\gamma_m^*})^{1+\alpha}, \tag{5.9}$$

therefore the scaling exponent α is related to γ_m^* as [108]:

$$1 + \gamma_m^* = \frac{4}{\alpha + 1}, \qquad \lambda \to 0. \tag{5.10}$$

The eigenvalues λ define an energy scale: large λ correspond to the ultraviolet while small λ probe the infrared dynamics. By introducing an energy-dependent scaling exponent $\alpha(\lambda)$, we can generalize the scaling form $\rho(\lambda) \propto \lambda^{\alpha(\lambda)}$ to obtain

$$1 + \gamma_m(\lambda) = \frac{4}{\alpha(\lambda) + 1}. \tag{5.11}$$

While the mass anomalous dimension is only well defined near the fixed points, we will show that the $\gamma_m(\lambda)$ extracted from Eqn. 5.11 agrees very well with the one-loop perturbative prediction near the UVFP in QCD-like systems, and when extrapolated to the infrared limit, it gives the desired value at the IRFP for infrared conformal systems. This behavior is sketched in Fig. 5.1 for idealized (infinite-volume, zero-mass, continuum) IR-conformal and chirally broken systems.

In the UV, considering only asymptotically free theories, $\gamma_m \to 0$ as $\lambda \to \infty$, which by Eq. 5.11 corresponds to $\alpha \to 3$, reproducing the known scaling $\rho(\lambda) \propto \lambda^3$ in free field theory [111]. In the context of lattice calculations, we are restricted to λ smaller than the UV cutoff defined by the inverse of lattice spacing a^{-1} (in lattice units, $\lambda \lesssim 1$). While larger eigenvalues can easily be calculated, they are in a regime dominated by lattice artifacts where no universal behavior can be identified.

In the IR, chirally broken systems and IR conformal theories behave differently:

- In IR-conformal systems, $\gamma_m \to \gamma_m^*$ as $\lambda \to 0$, to reproduce Eq. 5.10.
- In chirally broken systems, below the chiral symmetry breaking scale, $\rho(0) \neq 0$ and the scaling form $\rho(\lambda) \propto \lambda^{\alpha(\lambda)}$ breaks. As a result, while a naive application of Eq. 5.6 to chirally broken systems in the IR would produce $\alpha \to 0$ and $\gamma_m \to 3$ as $\lambda \to 0$, this prediction has no physical significance. Such unphysical large $\gamma_m(\lambda)$ simply indicates the breakdown of the scaling form due to the onset of chiral symmetry breaking.

In between these two extremes we obtain a scale-dependent exponent that connects the limiting UV and IR values. In IR-conformal systems, γ_m is restricted by $0 \leq \gamma_m(\lambda) \leq \gamma_m^*$ on the weak coupling side of the IRFP, and possibly starts to increase from γ_m^* with energy scale on the strong coupling side, as pictured by the lower left panel in Fig. 5.1. In the chirally broken systems, γ_m starts from 0 at the gaussian fixed point in the UV and increases toward the IR. After the onset of chiral symmetry breaking it continues shooting up to unphysical large values in the IR, indicating the scaling breaks down. While in the IR regime chiral effective field theory may be applied to analyze the Dirac eigenmodes for chirally broken systems, in this work we study the mass anomalous dimension in the intermediate range of energy scales from asymptotic freedom to the onset of chiral symmetry breaking, where chiral perturbation theory is not applicable.

To extract the scale-dependent exponent $\alpha(\lambda)$ and therefore $\gamma_m(\lambda)$ from the mode number, we perform a simple linear fit to the logarithmic form

$$\log[\nu(\lambda)] = (\alpha(\lambda) + 1)\log[\lambda] + \text{constant}, \tag{5.12}$$

using finite intervals $\Delta\lambda$ in the eigenvalues and a jackknife analysis to determine uncertainties. The $\Delta\lambda$ values used in different systems are in tables 5.1, 5.2, 5.3, 5.4, 5.5, 5.6.

5.3 Concerns about the Dirac eigenvalue density

There have been concerns about the physical meaning of the Dirac eigenvalue density, since it cannot be defined through the partition function of the system. We will state the problem here for completeness. The eigenvalue density $\rho(\lambda)$ on the lattice is defined as

$$\rho(\lambda) = \frac{1}{V}\sum_{n=1}^{\infty}\delta(\lambda - \lambda_n), \tag{5.13}$$

where λ_n is the nth lowest eigenvalue and V is the lattice volume. If we use the representation of the δ function

$$\delta(\lambda - \lambda_0) = \frac{1}{\pi}\lim_{\epsilon\to 0}\frac{\epsilon}{(\lambda - \lambda_0)^2 + \epsilon^2}, \tag{5.14}$$

the eigenvalue density can be rewritten as

$$\rho(\lambda) = \frac{1}{2\pi V}\lim_{\epsilon\to 0}\sum_n [\frac{1}{i(\lambda_n - \lambda) + \epsilon} - \frac{1}{i(\lambda_n - \lambda) - \epsilon}]. \tag{5.15}$$

On the other hand recall that $i\lambda_n$ are eigenvalues of the Dirac operator D, so we have

$$\frac{1}{D + m_v} = \sum_n |n\rangle\langle n|\frac{1}{i\lambda_n + m_v}, \tag{5.16}$$

where $|n\rangle$ denotes the corresponding eigenvector. Combing Eqns 5.13 and 5.16 we find the eigenvalue density can be expressed as

$$\rho(\lambda) = \frac{1}{2\pi V}\lim_{\epsilon\to 0}[\mathrm{Tr}(D - i\lambda + \epsilon)^{-1} - \mathrm{Tr}(D - i\lambda - \epsilon)^{-1}] \tag{5.17}$$

$$= \frac{1}{2\pi}\lim_{\epsilon\to 0}[\Sigma_{val}(i\lambda + \epsilon) - \Sigma_{val}(i\lambda - \epsilon)] \tag{5.18}$$

where

$$m_v = -i\lambda \pm \epsilon, \tag{5.19}$$

is the valence quark mass, and

$$\Sigma_{val}(m_v) = \frac{1}{V}\sum_n \langle\frac{1}{m_v + i\lambda_n}\rangle, \tag{5.20}$$

is the chiral condensate with valence quark mass m_v. We see that the Dirac eigenvalue density is defined in partially quenched theories, where the mass of valence fermions is different from that of the dynamical fermions. There is a first principles derivation of the connection between the spectral density as used here, and physical properties of an unquenched system, but it only applies to systems which are chirally broken [112]. The application to conformal systems remains to be shown. However, the agreement of the exponent computed with Dirac eigenmodes with that found with other methods suggests strongly that the method does in fact produce a correct mass anomalous dimension.

5.4 Potential systematic effects

The scaling form $\rho(\lambda) \propto \lambda^{\alpha}$ leading to Eq. 5.6 assumes that the system is in infinite volume with vanishing fermion mass. Lattice calculations are necessarily carried out in a finite volume, and typically use non-zero fermion masses as well. Both finite volume and finite mass break conformal scale invariance, which can only be recovered by extrapolations to the infinite-volume, chiral limit. However, Refs. [110] found negligible finite-volume effects for the mode number measured on 24^3 and $32^3 \times 64$ lattices in the SU(2) theory with two fermions in the adjoint representation, and also observed scaling behavior for surprisingly large fermion masses. While the results of [110] give us some confidence that systematic effects may be manageable, because we study different models using a different lattice fermion formulation and different ranges of bare parameters, we must carry out our own tests to directly check these issues.

5.4.1 Systematic effects from direct calculation

We carry out direct calculation of Dirac eigenvalues for $N_f = 4, 8$ and 12 systems, using Kalkreuter [113] and later PReconditioned Iterative MultiMethod Eigensolver (PRIMME) method [114]. The code was adapted to staggered fermions by David Schaich and Anna Hasenfratz. On each ensemble we measure 1000 to 1500 eigenvalues. Fig. 5.2 shows $\rho(\lambda)$ for different sea fermion masses in the 12 flavor system at $\beta_F = 2.8$ on $16^3 \times 32$ volumes. This coupling is strong yet safely on the weak coupling side of the $\cancel{S^4}$ phase. For $m > 0.02$, the eigenvalue density depends strongly on the mass, and appears unlikely to become mass independent even at larger λ . On the

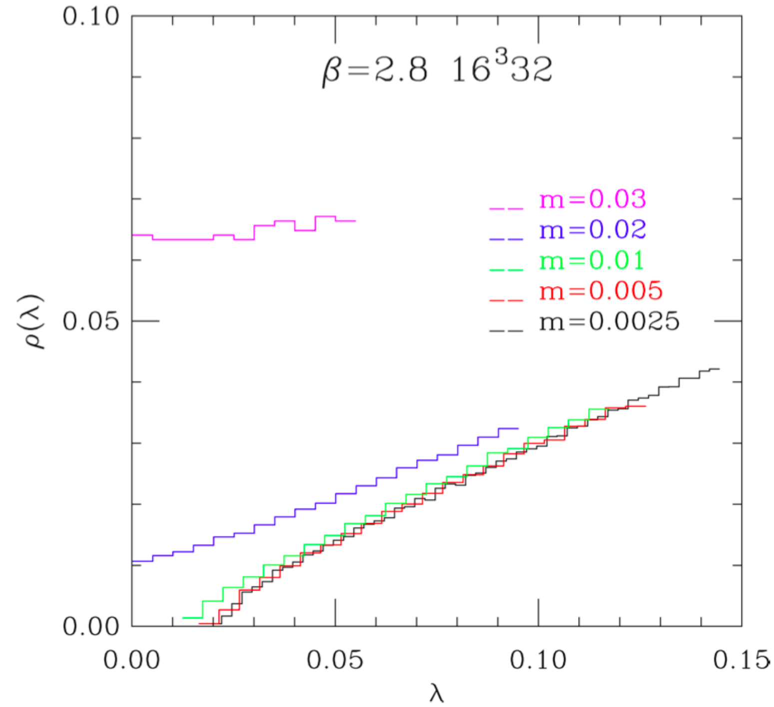

Figure 5.2: The eigenvalue density $\rho(\lambda)$ at $\beta_F = 2.8$ of the 12 flavor system on $16^3 \times 32$ volumes at various sea fermion mass values.

other hand for $m < 0.01$ the mass dependence rapidly disappears as λ increases, suggesting that here it is possible to reach the chiral limit by simple extrapolation. Since these tests are carried out at a relatively strong coupling with many fermions, we expect the mass constraint to be more stringent than required for the systems at weak couplings. The largest mass we use in our analysis is $m = 0.0025$.

Because we use such small masses, the finite volume is a more serious issue. To address finite-volume effects, we carry out simulations with several different lattice volumes and gauge couplings, combining the results to access the infinite-volume physics. We start with a review of the finite-volume effects on the spectral density $\rho(\lambda)$ to emphasize that these effects are manageable even in the chiral limit and at weak gauge couplings.

Fig. 5.3 illustrates the volume dependence of $\rho(\lambda)$ for the smallest mass in Fig. 5.2, $m = 0.0025$. The system is chirally symmetric on all four volumes considered, with $\rho(0) = 0$. At the small λ where the density becomes nonzero, there is transient volume dependence. All four volumes produce consistent results for larger λ which is still well below the cutoff scale. While there remains a small volume dependence even in this regime, an infinite volume extrapolation is feasible.

Fig. 5.4 and Fig 5.5 show the volume dependence of the $N_f = 4$ spectral density $\rho(\lambda)$, normalized per continuum flavor. We calculate 1000 eigenmodes on each lattice volume $24^3 \times 48$, $16^3 \times 32$ and $12^3 \times 24$. In Fig. 5.4 we consider the reasonably strong gauge coupling $\beta_F = 6.4$, where the largest volume (with $m = 0.0025$) shows chiral symmetry breaking, $\rho(0) \neq 0$. (The $\sim 30\%$ drop in the smallest-λ bin may suggest that the $24^4 \times 48$ volume is near the boundary of chiral restoration.) The other two systems are clearly volume-squeezed, and we observe a gap in the $12^3 \times 24$ eigenvalue density, which permits simulation in the $m = 0$ chiral limit. While the small λ region is affected by the finite lattice volume, this is only a transient effect. For $\lambda \geq 0.04$ the two larger volumes are indistinguishable, and all three volumes converge to the same curve shortly thereafter.

Fig 5.5 shows the $N_f = 4$ eigenvalue density from the same lattice volumes, now with $\beta_F = 7.0$. This coupling is significantly weaker (the lattice spacing at $\beta_F = 7.0$ is approximately half

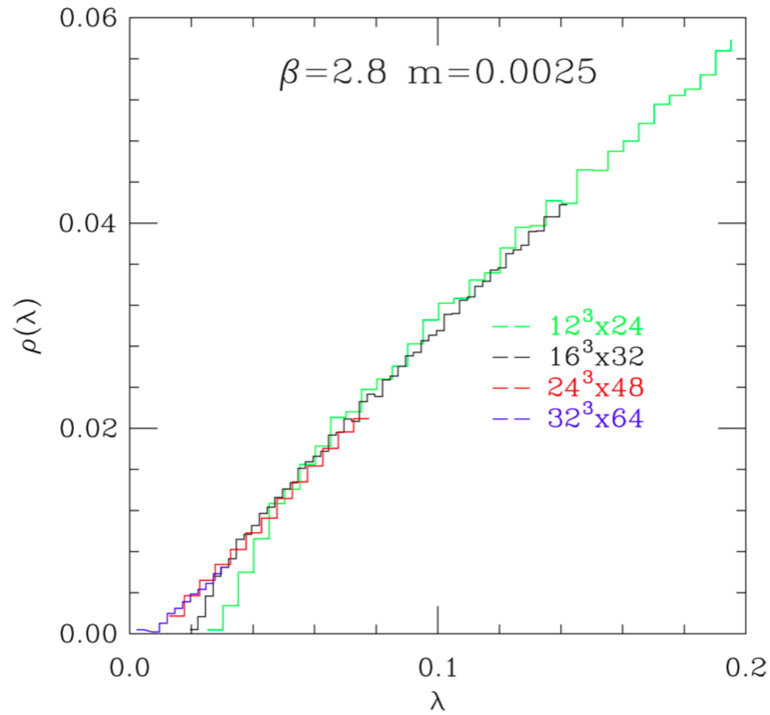

Figure 5.3: The eigenvalue density $\rho(\lambda)$ at $\beta_F = 2.8$ of the 12 flavor system with mass $m = 0.0025$ on various volumes.

of that at $\beta_F = 6.4$ basing on Eqn. 5.52), and we encounter no obstacle to working directly at $m = 0$: all three systems are volume-squeezed and chirally symmetric with gaps that grow smaller as the volume increase. Nevertheless at sufficiently large $\lambda > 0.15$ the different $\rho(\lambda)$ again overlap, indicating that finite-volume effects are manageable. As Fig. 5.5 illustrates, it is possible to identify volume-independent behavior even when volumes in the p-regime are combined with strongly volume-squeezed systems, both with small and exactly vanishing fermion masses.

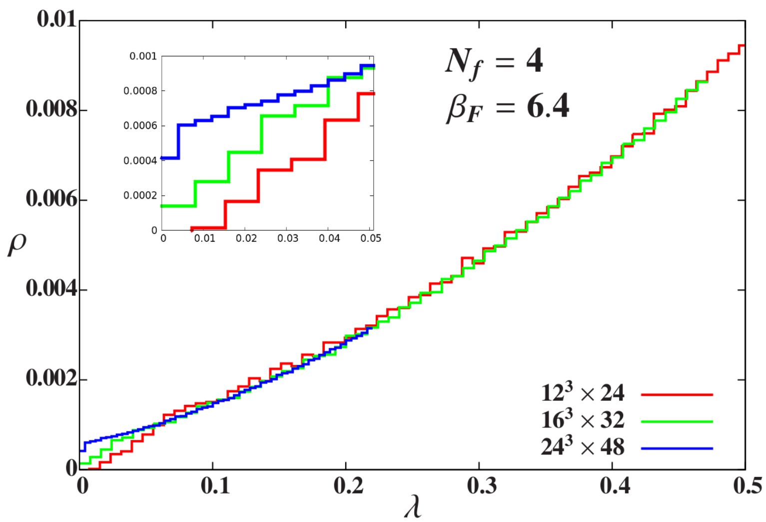

Figure 5.4: The volume dependence of the $\rho(\lambda)$ at $\beta_f = 6.4$ for $N_f = 4$. At this stronger coupling the system exhibits chiral symmetry breaking with $\rho(0) > 0$ on $24^3 \times 48$ lattices with $m = 0.0025$. The insets enlarge the small-λ behavior.

The finite-volume effects we observe in $\rho(\lambda)$ at small λ can only influence our determination of the mass anomalous dimension at comparably small λ. This is because we determine $\gamma_m(\lambda)$ from the logarithm of the mode number, by fitting Eqn. 5.12 over a finite interval in λ . Once we are beyond the small-λ region where finite-volume effects are most significant, this region makes only a constant contribution to $\nu(\lambda)$, which does not affect our extracted anomalous dimension. Moreover, it is straightforward to estimate the extent of this small-λ region from γ_m itself, as we illustrate in Fig. 5.6 and Fig. 5.7.

Fig. 5.6 shows $\gamma_m(\lambda)$ for $N_f = 4$ with $\beta_F = 6.4$, which comes from the data in Fig. 5.4. On the $24^4 \times 48$ volume the anomalous dimension is large in the small-λ regime, $\gamma_m(\lambda) \gtrsim 1$, consistent

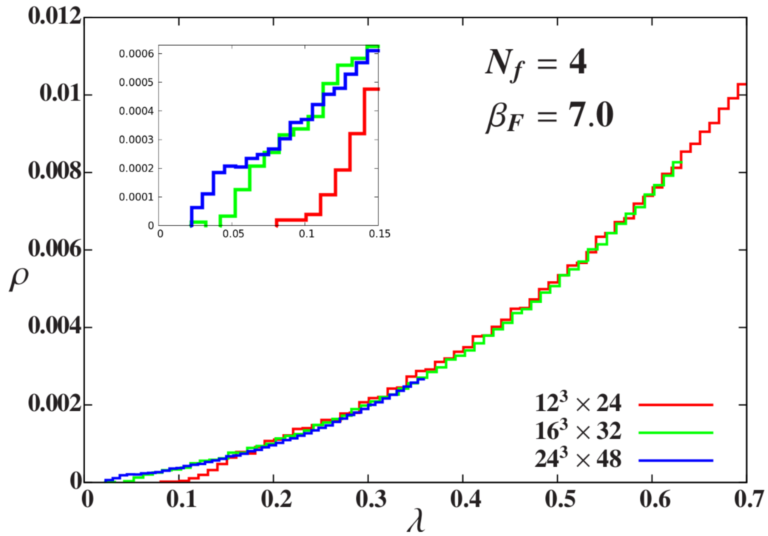

Figure 5.5: The volume dependence of the $\rho(\lambda)$ at $\beta_f = 7.0$ for $N_f = 4$. At this weaker coupling all three lattice systems are volume-squeezed and we encounter no obstacle to working directly at $m = 0$ on all three volumes. The insets enlarge the small-λ behavior.

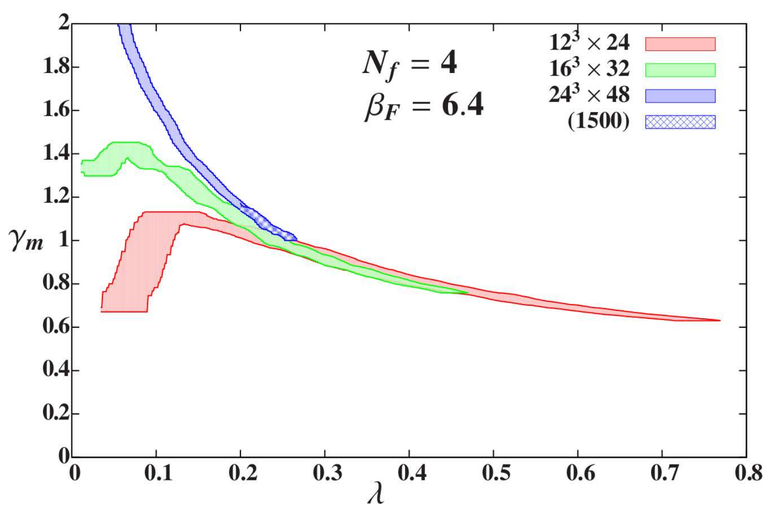

Figure 5.6: Predictions for γ_m from the scaling of ν for $N_f = 4$ at coupling $\beta_F = 6.4$, illustrating finite-volume effects at small λ . We observe $\gamma_m > 1$ on $24^3 \times 48$ lattices with $m = 0.0025$, consistent with chiral symmetry breaking found in Fig. 5.4.

with the chiral symmetry breaking established by Fig. 5.4. In volume-squeezed systems, the finite volume pushes the fitted $\gamma_m \to 0$ as $\lambda \to 0$. This behavior is also unphysical, and indicates the breakdown of the scaling form $\rho(0) \propto \lambda^{\alpha(\lambda)}$ due to finite-volume effects. Since we compare several lattice volumes in Fig. 5.6, we can easily identify these transient effects by observing where the results for a given volume break away from the combined curve.

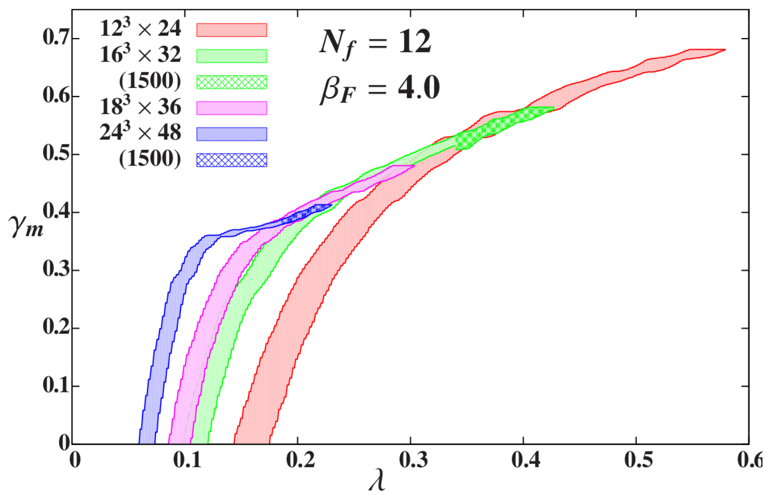

Figure 5.7: Predictions for γ_m from the scaling of ν for $N_f = 12$ at $\beta_F = 4.0$, illustrating finite-volume effects at small λ .

Fig. 5.7 considers the 12-flavor system with $\beta_F = 4.0$ and $m = 0.0025$ on $24^3 \times 48$, $16^3 \times 32$ and $12^3 \times 24$ lattices, also including $m = 0$ on $18^3 \times 36$ lattices. Again, after the small-λ transients, the γ_m from different volumes form a single curve indicating that both finite-volume and finite-mass effects are not significant in comparison to our statistical uncertainties.

However, as we are interested in the infrared dynamics of the $N_f = 12$ system, we push our study to weaker couplings and the finite-volume effects get more severe. At $\beta_F = 5.0$ and $\beta_F = 6.0$ even at large λ the results from different volumes do not overlap perfectly. Fig. 5.8 shows the mass anomalous dimension at $\beta_F = 5.0$ on $L^3 \times 2L$ lattices with L = 12, 16, 18, 24 and 32, where finite volume effects persist to quite large λ and make it hard to extract volume-independent physics. This situation calls for infinite-volume extrapolations that require data for $\nu(\lambda)$ at larger λ on the larger volumes. Directly measuring many more eigenmodes is computationally impractical, so we

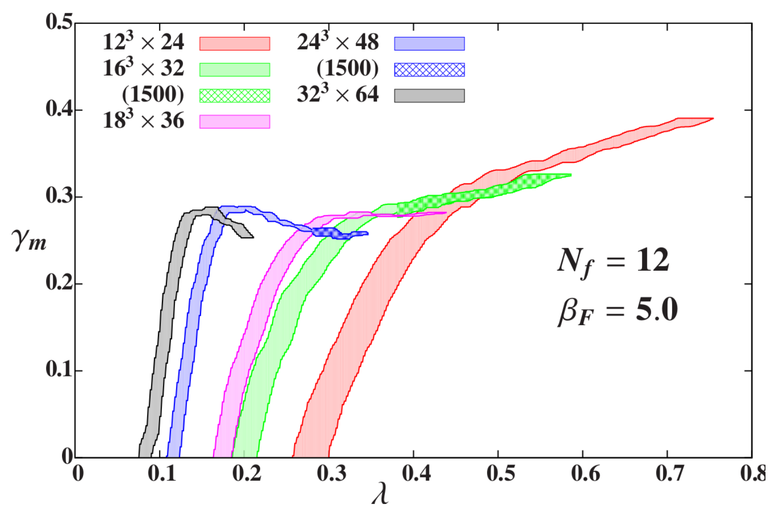

Figure 5.8: Finite volume effects for 12-flavor systems at $\beta_F = 5.0$, where the finite volume effects get so strong that we can hardly see any overlap between different volumes.

carry out stochastic calculations of the mode number, as in Ref. [107, 110].

5.4.2 Systematic effects from stochastic calculation

In the above investigation of potential systematic effects, we found that for the $N_f = 12$ system, although the finite volume effects are manageable at strong couplings, more eigenmodes on large lattice volumes will significantly help the extrapolation to the IR limit and infinite-volume limit. Since direct calculation becomes impractical due to our limited computer resources, we develop stochastic method to measure the eigenmode number instead of the eigenvalue, inspired by Refs. [107, 110]. The details of the stochastic algorithm will be presented in section 5.32. We are then able to extend our study on the interesting $N_f = 12$ and $N_f = 8$ systems as well as including the $N_f = 16$ system, which is known to be conformal, for comparison. We also add new symmetric configurations with anti-periodic boundary conditions in all four directions, so that we can run simulations at exactly zero fermion mass.

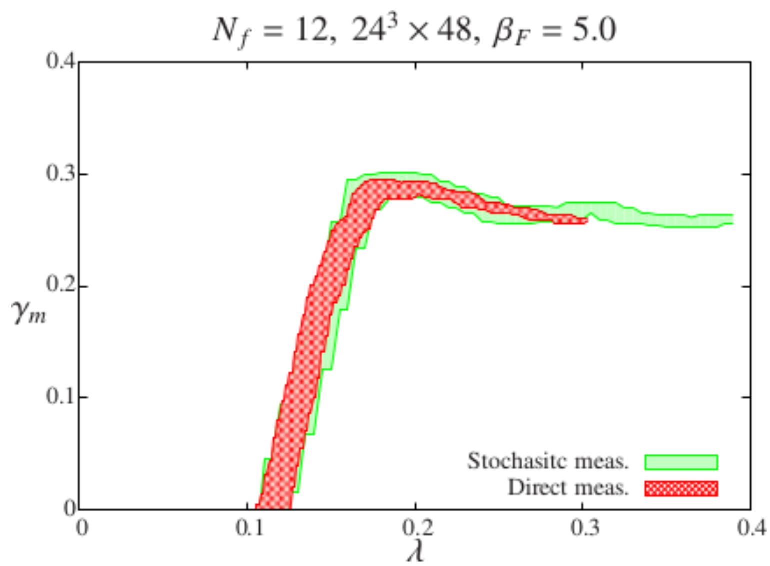

Figure 5.9: The mass anomalous dimension γ_m for $N_f = 12, \beta_F = 5.0$ on volume $24^3 \times 48$. The red band uses mode number from direct calculation, and the green band uses mode number from stochastic estimator. They overlap and confirm the correctness of the stochastic estimator.

The first thing to check is that the stochastic estimator we developed is correct. Since we have already performed direct calculation on some ensembles, we can directly compare the results from the stochastic estimator with the direction calculation to see whether they concise. Fig. 5.9 shows the results from the two methods on the same ensemble, and confirms that our stochastic estimator works as expected.

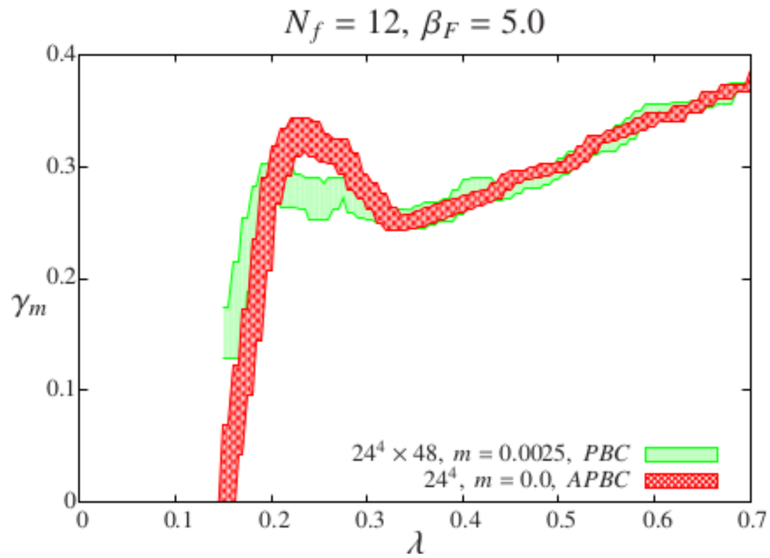

Figure 5.10: The mass anomalous dimension γ_m for $N_f = 12, \beta_F = 5.0$ on volume $24^3 \times 48$ with periodic spatial conditions and 24^4 with anti-periodic spatial conditions. The 24^4 has a larger bump due to finite volume effects, but the finite volume effects on the two ensembles disappear at the same $\lambda \sim 0.34$, and merge together afterwards.

In our extended study with stochastic estimator, we also include new symmetric L^4 configurations with anti-periodic boundary conditions, while in the old $L \times 2L$ configurations we have periodic boundary conditions in the spatial directions. It is interesting to see whether changing the boundary conditions have any effects on our results. Fig. 5.10 shows the results for $N_f = 12, \beta_F = 5.0$, $24^3 \times 48$ with periodic spatial boundary conditions and 24^4 with anti-periodic spatial conditions. The larger 'bump' on the 24^4 ensemble indicates that changing the boundary conditions magnifies the finite volume effects in magnitude. However, the finite volume effects on the two ensembles seem disappearing at the same $\lambda \sim 0.34$, and leaving the physics unaffected.

Since we have confirmed that the stochastic estimator works and the effects of changing boundary conditions are under control, we are ready to explore the finite volume effects in our

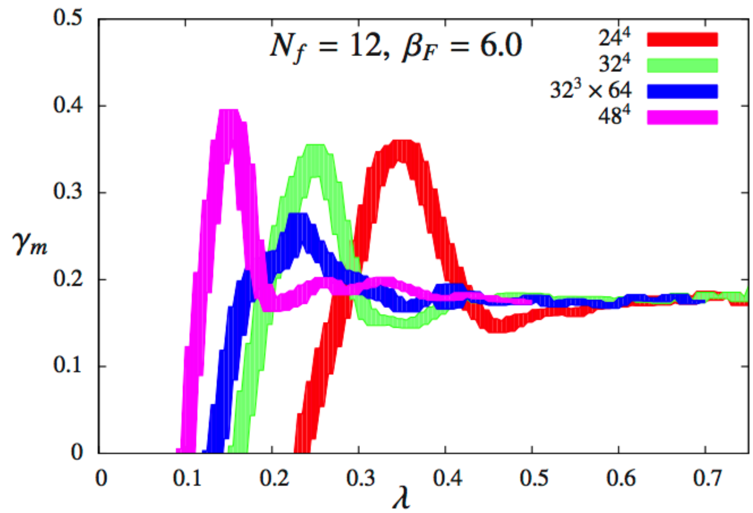

Figure 5.11: Finite volume effects for 12-flavor systems at $\beta_F = 6.0$ using stochastic estimator. Although $\beta_F = 6.0$ is the weakest coupling with most severe finite volume effects in our study, which seem to be further magnified by anti-periodic boundary conditions, we still manage to combine different lattices and obtain volume-independent physics at large enough λ .

new settings. Fig. 5.11 shows the $N_f = 12$ mass anomalous dimension at $\beta_F = 6.0$, our weakest coupling with the most severe finite-volume effects, on $24^4, 32^4, 32^3 \times 64$ and 48^4 volumes. Now by using stochastic calculation, we are able to greatly extend the λ range so that different volumes clearly merge together at large λ , while in Fig. 5.8 we can hardly see any overlap at $\beta_F = 5.0$. At $\lambda \gtrsim 0.6$ the predictions from the smallest $L = 24$ agree with the results from larger volumes. For the largest $L = 48$, finite volume effects appear manageable for $\lambda \gtrsim 0.4$. We also show how well γ_m from different volumes overlap at slightly stronger couplings $\beta_F = 4.0$ after deploying stochastic measurements in Fig. 5.12, compared with Fig. 5.7.

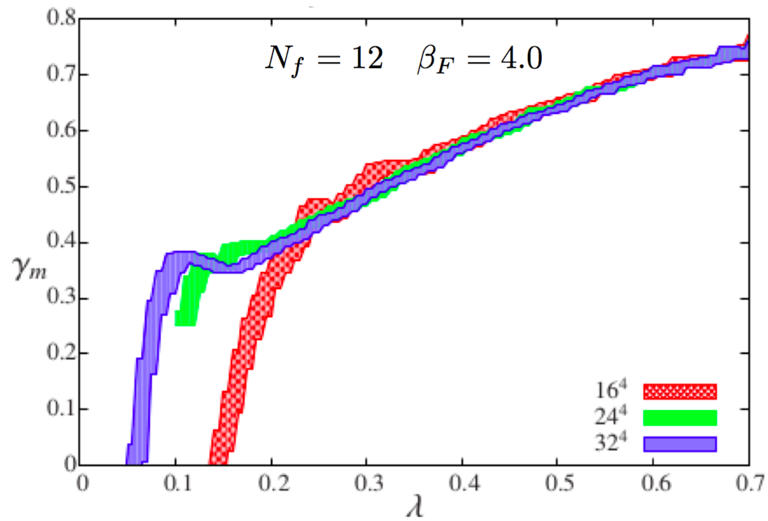

Figure 5.12: Predictions for γ_m from the scaling of ν for $N_f = 12$ at $\beta_F = 4.0$ from stochastic calculation, where we are able to extend λ range on large volumes, and obtain perfect overlap among different volumes.

While we use $m = 0$ in our extended studies, it is instructive to consider how finite mass affects the mode number and predicted γ_m. Fig 5.13 considers two $32^3 \times 64$ ensembles at $m = 0.02$ and 0.025, and a 32^4 ensembles with zero mass. With finite masses $m = 0.02$ and $m = 0.025$, the predicted anomalous dimension becomes unphysical large, $\gamma_m \gtrsim 2$ at small λ as the scaling form $\rho(\lambda) \propto \lambda^\alpha$ breaks down due to the explicit chiral symmetry breaking from the non-zero fermion masses. Even so, as λ increases γ_m turns back and join with the prediction from the zero mass ensemble. This test shows that the finite mass effects are under control.

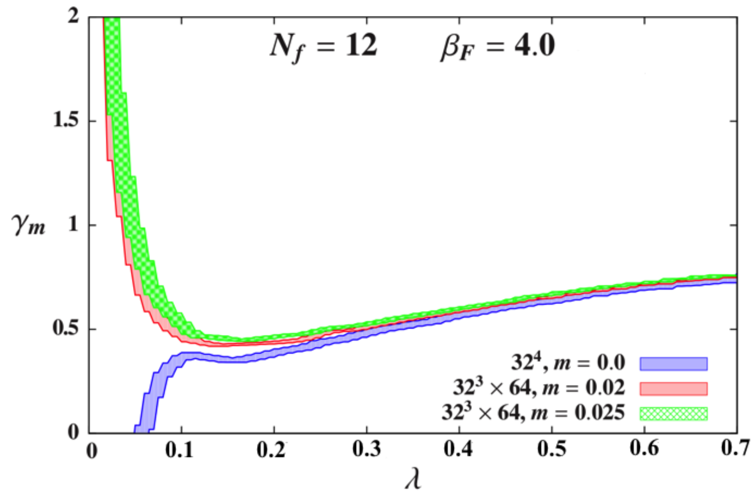

Figure 5.13: . Finite mass effects, tested on 12-flavor systems at $\beta_F = 4.0$. At $m = 0.02$ and $m = 0.025$, heavy fermion masses explicitly break chiral symmetry and cause unphysical large γ_m in the small λ region, but they join the curve from $32^4,\ m = 0$ ensemble shortly.

5.5 Stochastic estimator of Dirac eigenmode number

In this section I will introduce the stochastic algorithm to estimate the eigenmode number of the Dirac operator without calculating the eigenvalues, and the procedures to implement this method.

5.5.1 Overview

To get the mode number, we integrate over the δ functions in Eqn. 5.13 and multiply by the volume

$$\nu(\Omega) = 2V \int_0^{\Omega} \rho(\lambda) d\lambda, \tag{5.21}$$

which is equivalent to integrating from $-\Omega$ to Ω as do [107].

On lattice for computational convenience, instead of measuring the number of eigenvalues λ of D less than Ω, we measure the number of eigenvalues α of $D^\dagger D$ with $\alpha \leq \Omega^2$, because $D^\dagger D$ is hermitian and much easier to manipulate.

The spectral projector $\mathbb{P}_\Omega$ is defined over the vector space spanned by the eigenvectors of $D^\dagger D$ with eigenvalues lower than Ω^2, so that

$$\nu(\Omega) = \langle \mathrm{Tr}[\mathbb{P}_\Omega] \rangle \tag{5.22}$$

To avoid direct calculation of the low-lying eigenmodes, we calculate the trace $\langle \mathrm{Tr}[\mathbb{P}_\Omega] \rangle$ stochastically:

$$\nu(\Omega) = \frac{1}{n} \sum_{k=1}^{n} (\eta_k, \mathbb{P}_\Omega \eta_k), \tag{5.23}$$

where η_1, ..., η_n are a set of randomly generated pseudo-fermion fields. We fixe $n = 5$ in our calculations.

5.5.2 Approximation of the spectral projector $\mathbb{P}_\Omega$

There are basically three steps to construct the projector $\mathbb{P}_\Omega$: We start with an approximation of the sign function $xP(x^2)$, which is then used to construct an approximation of the step function $h(x)$, and finally we construct the projector from the approximation of the step function by $h^4(x)$.

In the first step we make use of a minmax polynomial $P(x)$ that minimizes the error:

$$\delta = \max_{\epsilon \leq x \leq 1} |1 - \sqrt{x} P(x)| \tag{5.24}$$

for a specified, positive and small ϵ. The function $xP(x^2)$ then approximate sign(x) in the range $\sqrt{\epsilon} \leq |x| \leq 1$.

The mixmax polynomial $P(x)$ is chosen to be represented in the form of a series of Chebyshev polynomials:

$$P(x) = \sum_{i=0}^{n} c_i T_i(z), \tag{5.25}$$

where

$$z = (2x - 1 - \epsilon)/(1 - \epsilon). \tag{5.26}$$

The deviation of the approximation is at most δ, which can be adjusted by tuning the polynomial degree n and ϵ. An example is given in Fig. 5.14 [115]. We tuned the parameters in our initial test and set $\epsilon = 0.01$, n=32 and correspondingly $\delta = 4.35 \times 10^{-4}$, as suggested by [110]. The approximation error is much smaller than the statistic error from the stochastic measurement.

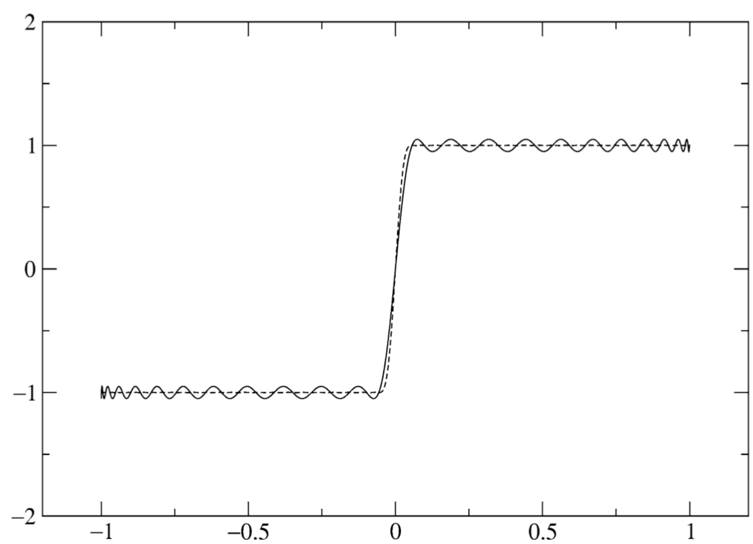

Figure 5.14: . Minmax polynomial approximation of sign(x). Both lines fix $\epsilon = 0.0025$. Full line uses $n = 22$ and has 5% relative error in the range $\sqrt{\epsilon} \leq |x| \leq 1$, while the dashed line uses $n = 57$ and has 0.1% relative error in the same range.

Now we can construct an approximation of a step function $\theta(-x)$ by

$$h(x) = \frac{1}{2}[1 - xP(x^2)] \tag{5.27}$$

for $\epsilon \le |x| \le 1$. Finally the projector $\mathbb{P}_\Omega$ is approximated by:

$$\mathbb{P}(\Omega) \simeq h(\mathbb{X})^4 \tag{5.28}$$

where

$$\mathbb{X} = 1 - \frac{2\Omega^{*2}}{DD^\dagger + \Omega^{*2}} \tag{5.29}$$

and

$$\frac{\Omega}{\Omega^*} = (\frac{1-\sqrt{\epsilon}}{1+\sqrt{\epsilon}})^{\frac{1}{2}} + \int_{-\sqrt{\epsilon}}^{\sqrt{\epsilon}} dx \frac{1+x}{(1-x^2)^{3/2}} h(x)^4. \tag{5.30}$$

The ration $\Omega/\Omega*$ is chosen to cancel the spectral integral in the transition region of the approximated step function, and the error

$$\Delta = \langle \mathrm{Tr}[\mathbb{P}_\Omega - h(\mathbb{X})^4] \rangle \tag{5.31}$$

has been shown much smaller than the statistical errors of the calculated mode numbers [107]. Therefore the stochastic representation of the mode number becomes:

$$(\eta, \mathbb{P}_M \eta) \simeq (\eta, h(\mathbb{X})^4 \eta) = ||h(\mathbb{X})^2 \eta||^2, \tag{5.32}$$

and the mode number is the square norm of $||h(\mathbb{X})^2\eta||$.

5.5.3 Implementation

The procedures to implement Eqn. 5.32 are as follows:

(1) The most basic operation is acting the operator $\mathbb{X}$ on a stochastic source R_0:

$$\mathbb{X}R_0 = R_0 - \frac{2\Omega^{*2}}{DD^\dagger + \Omega^{*2}} R_0. \tag{5.33}$$

Define

$$\frac{2\Omega^{*2}}{DD^\dagger + \Omega^{*2}} R_0 \equiv \psi, \tag{5.34}$$

and solve the equation

$$[DD^\dagger + \Omega^{*2}]\psi' = R_0, \tag{5.35}$$

where $\psi' = \psi/2\Omega^{*2}$, we can get

$$\mathbb{X}R_0 = R_0 - 2\Omega^{*2}\psi' \equiv R_1. \tag{5.36}$$

Most of the computational time is devoted to solve the Eqn. 5.35.

(2) After constructing $\mathbb{X}$ we can use it to build the operator $\mathbb{Z}$ from Eqn. 5.26. Acting the operator $\mathbb{Z}$ on the stochastic source R_0 gives:

$$\begin{aligned} \mathbb{Z}R_0 &= \frac{2\mathbb{X}^2 - 1 - \epsilon}{1-\epsilon} R_0 && (5.37)\\ &= \frac{1}{1-\epsilon}[2\mathbb{X}^2 R_0 - (1+\epsilon)R_0], && (5.38) \end{aligned}$$

The first term on the right hand side is:

$$\mathbb{X}^2 R_0 = \mathbb{X}R_1 = R_1 - 2\Omega^{*2}\psi'' \equiv R_2, \tag{5.39}$$

where we need to solve the equation again:

$$[DD^\dagger + \Omega^{*2}]\psi'' = R_1. \tag{5.40}$$

Therefore we get

$$\mathbb{Z}R_0 = \frac{1}{1-\epsilon}[2R_2 - (1+\epsilon)R_0]. \tag{5.41}$$

(3) Now comes the crucial step in the whole implementation: Computing the Chebyshev series. The coefficients of the Chebyshev polynomials c_i's can be easily calculated by minimizing δ in Eqn. 5.24. Then we can evaluate the Chebyshev series using Clenshaw algorithm:

$$\sum_{i=0}^{n} c_i T_i(\mathbb{Z}) = [b_0 T_0 + b_1(T_1 - 2\mathbb{Z}T_0)], \tag{5.42}$$

where

$$T_0 = 1, \quad T_1 = \mathbb{Z}. \tag{5.43}$$

The key is to evaluate the coefficients $b_0,\ b_1$ using the reversed recursion relation:

$$b_{n+1} = b_{n+2} = 0, \tag{5.44}$$

$$b_i(\mathbb{Z}) = c_i + 2\mathbb{Z}b_{i+1}(\mathbb{Z}) - b_{i+2}(\mathbb{Z}). \tag{5.45}$$

The first few terms in the recursion look like:

$$b_n = c_n, \tag{5.46}$$

$$b_{n-1} = c_{n-1} + 2\mathbb{Z}c_n, \tag{5.47}$$

$$b_{n-2} = c_{n-2} - c_n + 2c_{n-1}\mathbb{Z} + 4c_n\mathbb{Z}^2,\ \ldots \tag{5.48}$$

and we hereby construct the projector:

$$\begin{aligned} P(\mathbb{X}^2)R_0 &= \sum_{i=0}^{n} c_i T_i(\mathbb{Z})R_0 && (5.49)\\ &= (b_0 - \mathbb{Z}b_1)R_0. && (5.50) \end{aligned}$$

For n-degree Chebyshev polynomials we will need to solve Eqn. 5.35 $2n+1$ times, which consumes most of the computational time.

(4) The rest is straightforward. We apply the approximation of the step function $h(\mathbb{X})$ on the stochastic source R_0

$$h(\mathbb{X})R_0 = \frac{1}{2}[R_0 - \mathbb{X}P(\mathbb{X}^2)R_0] \tag{5.51}$$

and repeat this one more time to compute $h(\mathbb{X})^2R(0)$. Finally the mode number is given by the squared norm of $h(\mathbb{X})^2R_0$. The code of implementing the step function can be found in Appendix A.

5.6 Results for the $N_f = 4$ systems

In this section we describe our results for SU(3) lattice systems with $N_f = 4$ light or massless staggered fermions. This model exhibits QCD-like behavior, with spontaneous chiral symmetry breaking, confinement, and a running gauge coupling driven by the perturbative gaussian fixed

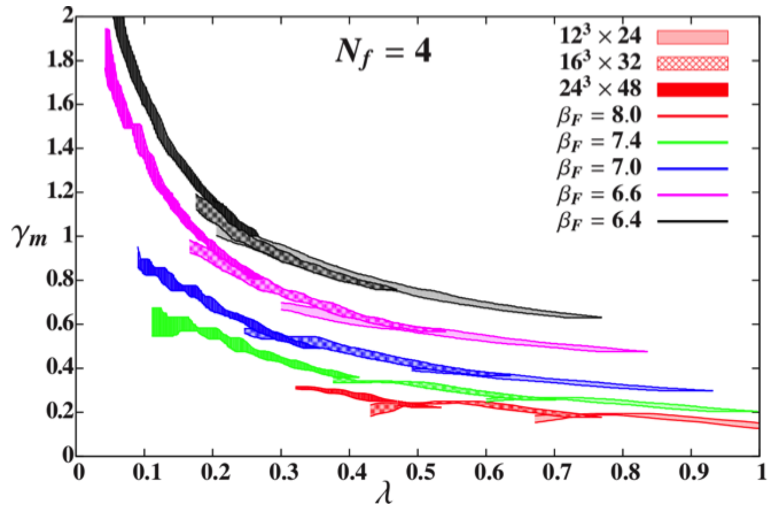

Figure 5.15: . The mass anomalous dimension for $N_f = 4$ system. At each gauge coupling, results from several lattice volumes are combined and the small λ regions affected by finite volume effects are cut off.

point. Our 4-flavor tests verify the applicability of our method to predict the scale-dependent mass anomalous dimension, illustrate the benefits of combining different lattice volumes and gauge couplings, and confirm the validity of results obtained from volumes much smaller than the confinement scale. The lattice ensembles used in the 4-flavor analysis are summarized in Table 5.1.

In the discussion of finite volumes effects we have seen how different volumes can be combined to obtain volume-independent predictions for the mass anomalous dimension. This is illustrated in 5.15 for all five gauge couplings we consider. The results are consistent with an asymptotically free UV fixed point: the mass anomalous dimension decreases towards UV at each coupling, and also decreases as the couplings get weaker. For QCD-like system we manage to do more: combining results at different gauge couplings into a single curve.

To combine our $N_f = 4$ results for multiple gauge couplings, we need to determine the relative lattice spacings a_{β_F} corresponding to different β_F. We accomplish this for lattice volumes $24^3 \times 48, 16^3 \times 32$ and $12^3 \times 24$ using Wilson flow. While our 4-flavor calculations are not extensive enough to carry out a completely controlled continuum extrapolation, we can easily determine the following relative scales:

$$\begin{aligned} &a_{6.4}/a_{7.4} = 2.84(3) \qquad a_{6.6}/a_{7.4} = 2.20(5) \\ &a_{7.0}/a_{7.4} = 1.45(3) \qquad a_{8.0}/a_{7.4} = 0.60(4). \end{aligned} \tag{5.52}$$

Thus the physical size of our configurations changes about an order of magnitude between the $24^3 \times 48$ volume and $\beta_F = 6.4$ and the $12^3 \times 24$ volume at $\beta_F = 8.0$. The errors in Eq. 5.52 are conservative, but suffice for the analysis we consider here.

Then we can rescale the lattice eigenvalues λ_β so that they are all expressed in terms of a uniform scale, $a_{7.4}$ corresponding to $\beta_f = 7.4$. In the chirally symmetric regime

$$\lambda_\beta \to \lambda_\beta (\frac{a_{7.4}}{a_\beta})^{1+\gamma_m(\lambda_\beta)}, \tag{5.53}$$

where the scaling dimension $1 + \gamma_m(\lambda)$ appears because λ scales in the same way as m. This is easy to understand by recalling that the massive Dirac operator is $D_m = D + m$. In the chirally broken

Table 5.1: $N_f = 4$ lattice ensembles used in Figs. 5.4, 5.5, 5.6, 5.15 and 5.16. For each ensemble specified by the volume, fermion mass, and gauge coupling β_F, we report the total molecular dynamics time units generated with the HMC algorithm, the number of configurations on which we measure at least 1000 (1500) eigenvalues, and the fit range $\Delta\lambda$.

Volume	Mass	β_F	Total MDTU	# meas.	$\Delta\lambda$
$24^3 \times 48$	0.0025	6.4	920	32 (6)	0.015
	0.0025	6.6	635	26	0.015
	0.0	7.0	800	31	0.0225
	0.0	7.4	790	30	0.0325
	0.0	8.0	1000	40 (40)	0.04
$16^3 \times 32$	0.0025	6.4	1365	41	0.0325
	0.0025	6.6	1125	46	0.0375
	0.0	7.0	750	47	0.05
	0.0	7.4	750	47	0.05
	0.0	8.0	1400	41	0.0525
$12^3 \times 24$	0.0	6.4	1000	50	0.055
	0.0	6.6	1000	50	0.07
	0.0	7.0	1000	62	0.07
	0.0	7.4	1000	61	0.07
	0.0	8.0	1840	86	0.075

regime the scaling form $\rho(\lambda) \propto \lambda^{\alpha(\lambda)}$ no longer holds, and results for γ_m determined from Eq. 5.11 are not physical. Therefore, when $\gamma_m > 1$ we take

$$\lambda_\beta \rightarrow (\frac{a_{7.4}}{a_\beta})^2. \tag{5.54}$$

Our choice of $\gamma_m = 1$ as the value at which we switch from Eq. 5.53 to Eq. 5.54 is motivated by our observation that those systems with $\gamma_m > 1$ also posses $\rho(0) > 0$. This is what we would expect from the conventional wisdom that chiral symmetry breaking sets in for $\gamma_m \gtrsim 1$. While this choice is rather arbitrary, the range where $\gamma_m > 1$ is so small that using only Eq. 5.53 would not make a significant difference.

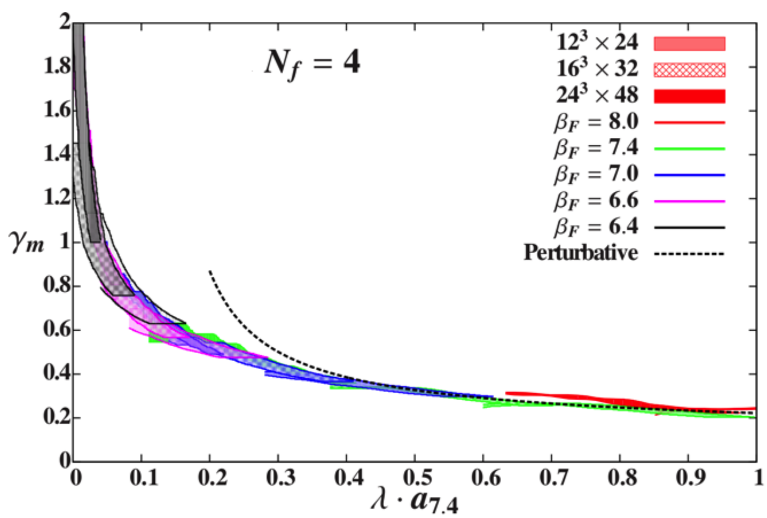

Figure 5.16: . Mass anomalous dimension for $N_f = 4$ system. We rescale the $N_f = 4$ results to be expressed in terms of a common lattice spacing ($a_{7.4}$ corresponding to $\beta_F = 7.4$). The dashed line is the one-loop perturbative prediction of the mass anomalous dimension.

Applying Eqs. 5.52-5.54 to the 4-flavor results produces the single curve shown in Fig. 5.16. Every volume and gauge coupling we consider can be combined to cover nearly two orders of magnitude in energy, from the onset of chiral symmetry breaking in the IR to the perturbative regime in the UV. The dashed line in Fig 5.16 is the one-loop perturbative prediction of the anomalous dimension,

$$\gamma_m(\lambda) = c_0 g^2(\lambda) = [2\frac{b_0}{c_0}\log(\lambda/\Lambda)]^{-1}, \tag{5.55}$$

where the leading-order coefficients are

$$c_0 = \frac{6C_2(R)}{16\pi^2}, \tag{5.56}$$

and b_0 is given in Eqn. 2.39 for fermions in representation R. We fix the scale Λ by matching the perturbative prediction with our numerical results at $\lambda_{7.4} = 0.8$. After fixing the relative scale, our numerical results agree with perturbation theory while $\gamma_m \lesssim 0.4$. Even at stronger couplings where our non-perturbative results break away from the perturbative prediction, we still obtain a single combined curve well into the chirally broken regime. It is reassuring that such a consistent picture is produced by combining so many lattice systems with different finite-volume and lattice spacing effects. From this test we see that all of our $N_f = 4$ systems are in the basin of attraction of the perturbative fixed point, with scaling violations small compared to our statistical uncertainties.

The 4-flavor model provides robust rests of our proposal in the relatively familiar context of QCD-like systems. We observe that the systematic effects discussed in section 5.4 are manageable, justifying our use of volumes much smaller than the confinement scale. The universal curve we obtain after rescaling with Eqns 5.52-5.54 demonstrates the power of combining multiple volumes and gauge couplings, and confirms that finite-mass effects are negligible for $m = 0.0025$. These results increase our confidence in the method.

5.7 Results for the $N_f = 12$ system

The SU(3) 12-flavor system has been one of the most controversial systems regarding its infrared dynamics. In chapter 4, we observed an unusual $\cancel{S^4}$ lattice phase where the single site shift symmetry ("S^4") of the lattice action is spontaneously broken. We restrict our presents analysis of the Dirac eigenmodes to $\beta_F \geq 3.0$, weak enough to avoid the $\cancel{S^4}$ lattice phase. Our $N_f = 12$ simulations in this range of couplings, which include volumes as large as 48^4 with vanishing masses, do not show spontaneous chiral symmetry breaking.

Fig. 5.17 shows the results from direct calculations of Dirac eigenvalues at $\beta_F = 3.0, 4.0, 5.0, 6.0$, and Fig. 5.18 shows the results from stochastic estimator of Dirac eigenmode number with addi-

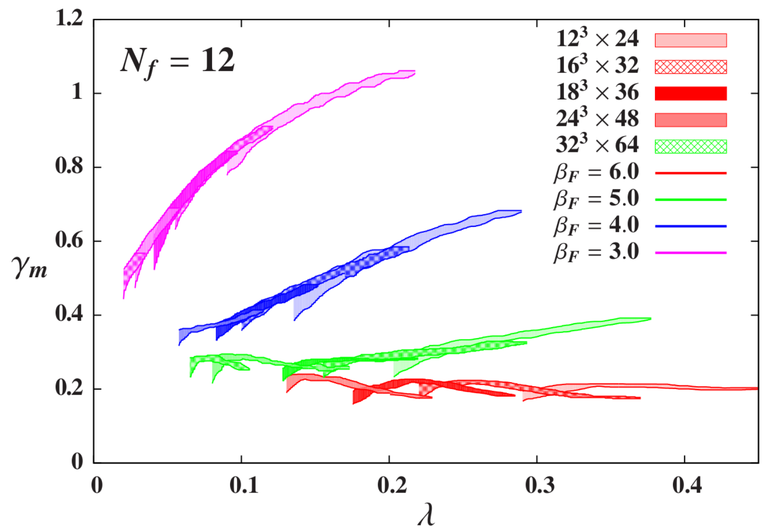

Figure 5.17: . The effective mass anomalous dimension γ_m for $N_f = 12$ model using direct calculation. At weaker couplings the finite volume effects are large.

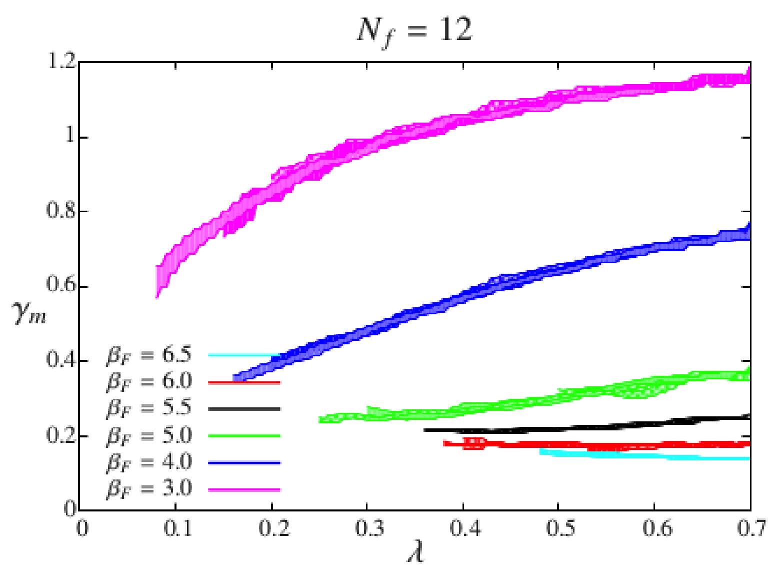

Figure 5.18: . The mass anomalous dimension γ_m for $N_f = 12$ model using stochastic calculation. All volumes overlap and essentially indistinguishable.

Table 5.2: $N_f = 12$ lattice ensembles used in direct calculation (Figs. 5.7, 5.8 and 5.17), with columns as in Table 5.1.

Volume	Mass	β_F	Total MDTU	# meas.	$\Delta\lambda$
$32^3\times64$	0.0025	3.0	1370	11	0.015
	0.0025	5.0	1250	13	0.015
$24^3\times48$	0.0025	3.0	1075	40	0.015
	0.0025	4.0	1000	24 (22)	0.015
	0.0025	5.0	1000	40 (9)	0.015
	0.0025	6.0	1250	36 (36)	0.0225
$18^3\times36$	0.0	3.0	1250	32	0.015
	0.0	4.0	1260	30	0.02
	0.0	5.0	1250	62	0.0225
	0.0	6.0	1250	52	0.025
$16^3\times32$	0.0025	3.0	2000	40	0.015
	0.0025	4.0	980	40 (6)	0.0225
	0.0025	5.0	1020	40 (6)	0.03 (0.35)
	0.0025	6.0	1130	24 (24)	0.0325
$12^3\times24$	0.0025	3.0	2000	40	0.0225
	0.0025	4.0	550	40	0.0325
	0.0025	5.0	900	40	0.0425
	0.0025	6.0	850	40	0.045

Table 5.3: $N_f = 12$ lattice ensembles used in stochastic estimator (Figs. 5.11, 5.12, 5.18). Columns are lattice volume, fermion mass, tgauge coupling β_F, otal MDTU and the number of thermalized configurations on which measurements are made. Each fit uses 3 point and λ are measured with constant separation $\Delta\lambda = 0.01$.

Volume	Mass	β_F	Total MDTU	# meas.
48^4	0.0	6.0	3500	38
$32^3\times64$	0.0025	5.0	1250	20
	0.0025	6.0	1981	15
32^4	0.0	4.0	10000	34
	0.0	6.0	10000	40
$24^3\times48$	0.0025	3.0	1075	34
	0.0025	5.0	1000	10
24^4	0.0	4.0	6000	40
	0.0	5.0	6000	40
$18^3\times36$	0.0	3.0	1250	32
$16^3\times32$	0.0025	3.0	2000	40
16^4	0.0	4.0	10000	40
	0.0	5.0	10000	40
	0.0	6.0	10000	40

tional $\beta_F = 5.5, 6.5$. The lattice ensembles used in the direct and stochastic calculations are summarized in Table 5.2, 5.3, respectively. In both plots we span a significant range from near the $\not{S}^4$ phase to the weakest coupling where finite-volume effects remain manageable on the largest volumes we explore. We only present results that appear largely volume independent. It is clear that significant improvements at weak couplings are achieved by using stochastic estimator. In Fig. 5.17 at weak couplings $\beta_F = 5.0,\ 6.0$ we do not obtain satisfactory overlap between different volumes, while in Fig. 5.18, at each β_F results from up to five different volumes overlap perfectly and essentially indistinguishable. Therefore we do not distinguish different volumes in Fig. 5.18.

The results at strong couplings are striking. They do not follow the behavior expected near the asymptotically-free fixed point: γ_m increases towards the ultraviolet for all $\beta_F < 6.0$, but decreases as the coupling gets weaker. This behavior is not consistent with the ultraviolet dynamics that is driven by the perturbative fixed point, and implies that all couplings $\beta_F < 6.0$ are outside the scaling regime of the UVFP.

Another contrast with the 4-flavor case is that the 12-flavor results for these gauge couplings cannot be rescaled to a unique curve. This is consistent with an irrelevant gauge coupling. Analysis that considers only a single gauge coupling and neglect the $\lambda \to 0$ extrapolation, risks at getting a precise but incorrect value of γ_m^*.

Our results are consistent with the existence of a conformal IR fixed point. The energy dependence of the mass anomalous dimension is minimal at $\beta_F = 6.0$, suggesting that this gauge couplings is close to the fixed point β_F^* in the scheme defined by this observable. The finite volumes of our lattice systems prevent us from directly investigating $\lambda = 0$. At the smallest $\lambda \sim O(0.1)$ that we can access, the γ_m from different β_F vary over a wide range $0.2 \lesssim \gamma_m \lesssim 0.6$. This is due to the slow running of the gauge coupling, as have been observed and discussed in similar models [116, 117]. Even though the dependence of γ_m on the gauge coupling dies out fairly slowly, the results for different β_F do approach a common value in the infrared, as expected for an IRFP at which the gauge coupling is irrelevant.

In the IR-conformal interpretation of our 12-flavor results, we identify this common value with the universal, scheme-independent γ_m^* at the conformal fixed point. To determine it we consider four couplings near the IRFP: $\beta_F = 5.0, 5.5, 6.0, 6.5$ and extrapolate results from the largest volumes that cover a sufficient range of λ. We use quadratic extrapolation for each coupling while constrain them sharing a common intercept. To ensure all couplings contribute equally we use 15 points from each coupling. To estimate the uncertainty we use jackknife analysis with 20 configurations at each coupling. The extrapolations are shown in Fig. 5.19.

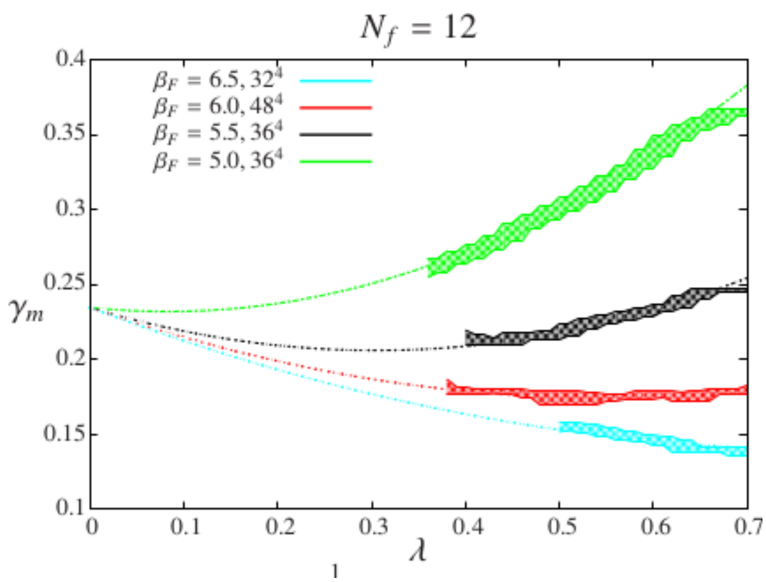

Figure 5.19: Extrapolations of γ_m from the results at the largest volumes (see Table. 5.3) at each coupling. The bands are data and the dashed lines are extrapolations. The common intercept is predicted to be 0.235(27).

In this manner we predict $\gamma_m^* = 0.235(27)$. This value is consistent with the 4-loop perturbative prediction $\gamma_m^* = 0.253$ in the $\bar{M}S$ scheme [44], and is comparable to other recent lattice results for $N_f = 12$. Ref. [118] obtains $0.4 \lesssim \gamma_m^* \lesssim 0.5$ from IR-conformal finite-size scaling of spectral observables, considering two relatively weak gauge couplings and large fermion masses $m \geq 0.04$. Ref. [119] considers smaller masses $0.006 \leq m \leq 0.035$ at a single gauge coupling, but argues against the existence of an IR fixed point for $N_f = 12$ on the grounds that finite-size scaling of different observables predicts different $0.2 \lesssim \gamma_m \lesssim 0.4$. In [120] we demonstrated that the apparent inconsistencies in the finite size scaling analysis [118, 119] can be resolved by considering the effect of the leading irrelevant coupling, and concluded that the $N_f = 12$ system is infrared conformal with $\gamma_m^* = 0.235(15)$, which is surprisingly consistent with the our prediction here.

To further verify the value we predict is scheme-independent, we perform similar analysis with twice nHYP smeared configurations at $\beta_F = 4.0, 4.5, 5.0$, and predict $\gamma_m^* = 0.231(36)$, which is consistent with our previous prediction. On the twice nHYP smeared configurations we encounter larger finite volume effects and have to push the cutoff λ to higher values, which makes the extrapolation to the $\lambda \to 0$ limit sensitive to the cutoffs. Despite this instability we are able to get very consistent predictions with reasonable cutoffs. The extrapolations are shown in Fig. 5.20.

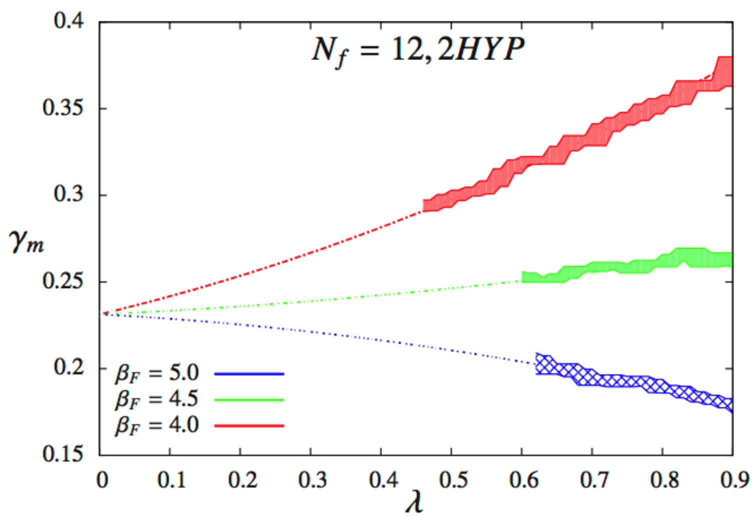

Figure 5.20: Extrapolations of γ_m from twice nHYP smeared configurations. The bands are data and the dashed lines are extrapolations. The common intercept is predicted to be 0.231(36).

While numerical calculations cannot exclude the possibility that some unexpected and unusual property of a chirally-broken system produces the behavior of γ_m depicted in Fig. 5.18, it is difficult to image how our $N_f = 12$ data could be consistent with spontaneous chiral symmetry breaking. Such an interpretation would require a major qualitative change in the $\beta_F < 6.0$ eigenvalue spectra for larger volumes on which smaller energy scales would be accessible. Even if large-volume simulations showed spontaneous chiral symmetry breaking in the IR, the ultraviolet behavior at these couplings is not consistent with asymptotic freedom, which requires that γ_m

decreases to zero in the UV.

5.8 Results for the $N_f = 8$ system

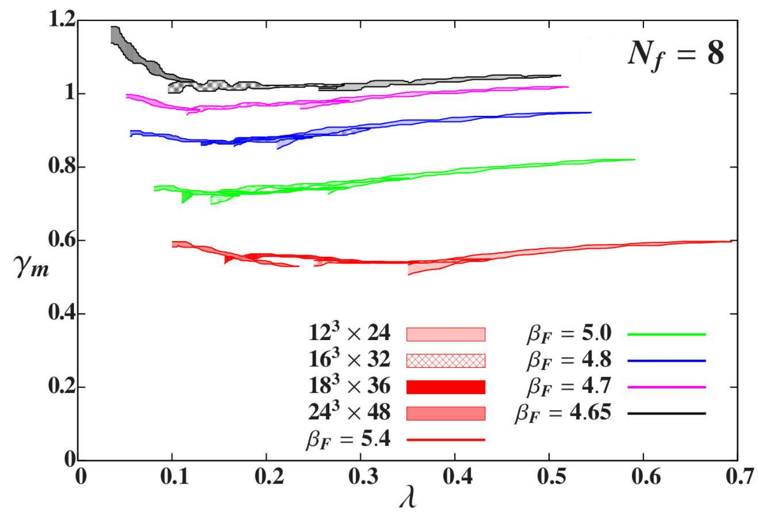

Figure 5.21: The mass anomalous dimension γ_m for $N_f = 8$ model from direct calculation.

The $N_f = 8$ system is also interesting to study. As for $N_f = 12$, we consider only weak enough couplings to avoid the 8-flavor $\not{S}^4$ phase, though our strongest $\beta_F = 4.65$ is close to this transition. Table 5.4 summarizes these ensembles used in the direct calculations and Table 5.5 summarizes the ensembles used in the stochastic calculations.

Our data are not consistent with the ϵ-regime scaling $\lambda_n \propto 1/V$; instead, the low-lying eigenvalues scale with the volume raised to a power consistent with the anomalous dimension shown in Fig. 5.21 and 5.22. While we have not been able to establish spontaneous chiral symmetry breaking for $N_f = 8$, even on volumes as large as $32^3 \times 64$ and $40^4 \times 30$ [50], neither did we observe an IR fixed point with the MCRG method [5, 121].

We show our results for the 8-flavor anomalous dimension in Fig. 5.21 and 5.22. They differ from both the 4- and 12-flavor cases. The anomalous dimension shows very little dependence on λ, but changes with the gauge coupling. At each fixed coupling, we find γ_m to be roughly constant

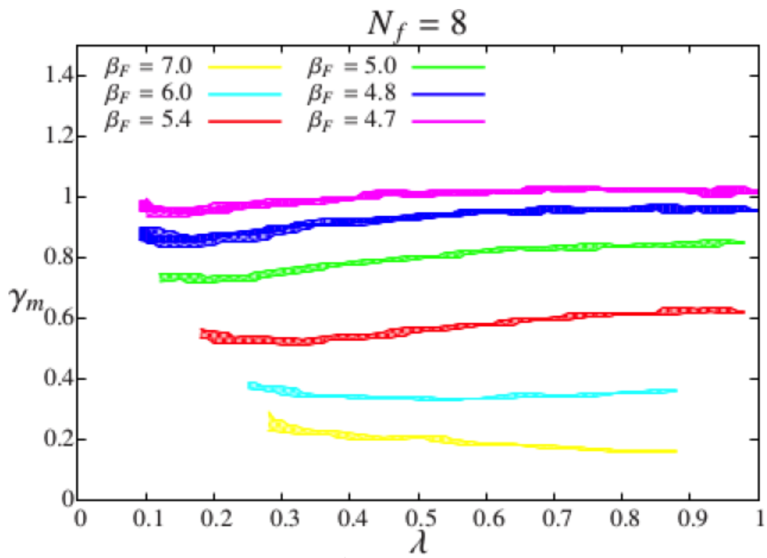

Figure 5.22: The mass anomalous dimension γ_m for $N_f = 8$ model from stochastic calculation. All measurements are in chiral limit.

Table 5.4: $N_f = 8$ lattice ensembles used direct calculation (Figs. 5.23 and 5.21), with columns as in Table 5.1.

Volume	Mass	β_F	Total MDTU	# meas.	$\Delta\lambda$
	0.0	4.65	224	11	0.015
	0.0	4.7	385	24	0.015
$24^3\times 48$	0.0	4.8	540	37	0.015
	0.0	5.0	435	34	0.015
	0.0	5.4	690	52	0.015
	0.0	4.8	960	50	0.015
$18^3\times 36$	0.0	5.0	930	52	0.02
	0.0	5.4	1000	50	0.0225
	0.0	4.65	980	25	0.0175
	0.0	4.7	1250	70	0.0175
$16^3\times 32$	0.0	4.8	595	29	0.02
	0.0	5.0	690	39	0.0225
	0.0	5.4	940	36	0.0275
	0.0	4.65	750	47	0.0275
	0.0	4.7	1250	67	0.0325
$12^3\times 24$	0.0	4.8	1250	87	0.035
	0.0	5.0	1250	87	0.035
	0.0	5.4	1250	43	0.045

Table 5.5: $N_f = 8$ lattice ensembles used in stochastic calculation (Fig. 5.22). All configurations are in chiral limit (zero mass). Each fit uses 3 points while λ are measured with constant separation $\Delta\lambda = 0.02$.

Volume	β_F	Total MDTU	# meas.
$32^3 \times 64$	4.7	1510	23
	4.8	1210	20
	6.0	1479	20
	7.0	1473	15
$24^3 \times 48$	4.7	404	12
	4.8	540	9
	5.0	435	20
	5.4	690	12

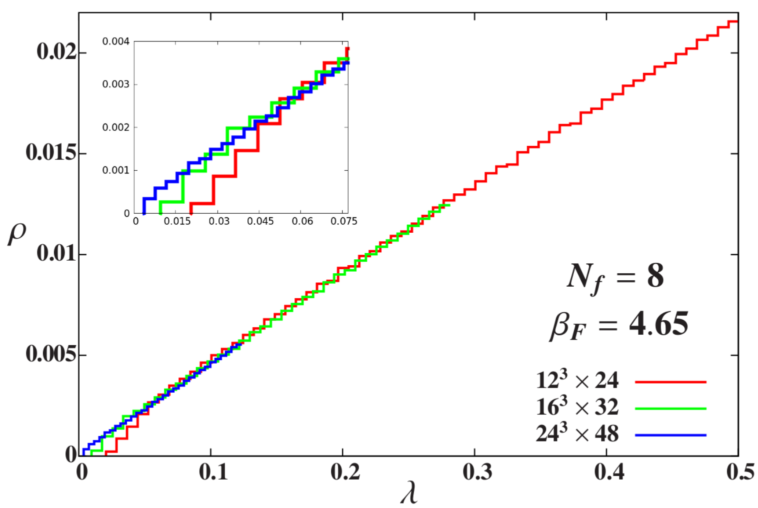

Figure 5.23: Volume dependence of the spectral density $\rho(\lambda)$, normalized per continuum flavor, for $N_f = 8$ with $\beta_F = 4.65$. We do not observe spontaneous chiral symmetry breaking even on our largest $24^3 \times 48$ and $32^3 \times 64$ volumes. The insets enlarge the small-λ behavior.

over the order-of-magnitude change in scale accessible from combining lattice volumes, with a slight tendency to increase both towards the UV and towards the IR at $\beta_F \leq 6.0$. $\gamma_m(\lambda)$ increasing with large λ suggests that these systems are not in the basin of attraction of the perturbative fixed point. The non-monotonicity of $\gamma_m(\lambda)$ prevents us from rescaling λ_β to obtain a combined universal curve. The λ dependence of the 8-flavor anomalous dimension most closely resembles that observed for $N_f = 12$ at $\beta_F = 5.0$. As we move to stronger couplings, γ_m increases significantly (but remains $\gamma_m \lesssim 1$), while the overall structure of $\gamma_m(\lambda)$ does not change. At our strongest accessible gauge coupling $\beta_F = 4.65$, the anomalous dimension is $\gamma_m \gtrsim 1$, yet we do not observe spontaneous chiral symmetry breaking even on our largest volumes.

These results, like our other investigations of the 8-flavor system, are hard to interpret. At a minimum, we observe that the anomalous dimension is large, $\gamma_m \approx 1$ across a wide range of scales (consistent with the results of Ref. [28] using finite-size-scaling.) We also see that different gauge couplings produce greater changes in γ_m than does evolution over an order of magnitude in energy. This behavior is consistent with a "walking" gauge coupling.

5.9 Results for the $N_f = 16$ system

The $N_f = 16$ system is right below the upper edge of the conformal window as predicted by the two loop beta function, and is believed to be IR-conformal. We expanded our study to the $N_f = 16$ system using the stochastic estimator and take it as an illustrative example of IR conformal systems. The ensembles we used for $N_f = 16$ system are summarized in Table 5.6. All volumes are anti-periodic with the fermion mass at exactly zero. For each ensemble we perform measurements on 20 thermalized configurations. The results are shown in Fig. 5.24. For the $N_f = 16$ system we observe large finite volume effects in the infrared as well as large cut-off effects in the ultraviolet. At weak couplings these two effects meet and makes it difficult to perform quantitative analysis.

The IRFP of $N_f = 16$ system is at weak coupling and therefore the two-loop perturbation theory should give reliable estimates both to the coupling $g_*^2 = 0.5$ and the mass anomalous dimension $\gamma_m^* = 0.022$. Our original goal was to demonstrate that the numerical simulations can

Table 5.6: $N_f = 16$ lattice ensembles used with stochastic estimator (Fig. 5.24 and 5.25). All fermion masses are set to zero. Each fit uses 3 point and λ are measured with constant separation $\Delta\lambda = 0.01$.

Volume	β_F	Total MDTU	# meas.
36^4	6.0	1000	20
	7.0	1000	20
	8.0	1000	20
24^4	4.0	1000	20
	4.5	1000	20
	5.0	1000	20
	6.0	1500	20
	7.0	1500	20
	8.0	1500	20
16^4	4.0	1000	20
	4.5	1000	20
	5.0	1000	20
	7.0	1500	20

predict these values. However, in our action $g_*^2 = 0.5$ corresponds to $\beta_F = 12/g^2 = 24$, considerably weaker than our largest simulation coupling $\beta_F = 8.0$. Even at $\beta_F = 8$ the finite volume effects are so strong that it persists to the the UV region where the lattice cutoff effects set in. We tentatively performed a linear extrapolation on the largest volume at each coupling using 15 points from $\beta_F = 4.0$ to 7.0, constraining that they have a common intercept. The results are illustrated in Fig. 5.25 and predict $\gamma_m^* = 0.025(10)$ in the infrared limit. The value should not be taken too seriously as the fit is not satisfactory, the extrapolations start at large λ and therefore are sensitive to the cutoff values, and the couplings we can access is far from the IRFP. Nevertheless, the strong positive dependence of the mass anomalous dimension on the energy scale at strong couplings is very similar to the $N_f = 12$ system and supports our conclusion on the IR-conformal nature of the $N_f = 12$ system.

5.10 Conclusion

We have shown how to extract the scale-dependent mass anomalous dimension $\gamma_m(\lambda)$ from the renormalization group invariant Dirac eigenmode number $\nu(\lambda)$. We tested our method with 4-, 8-,

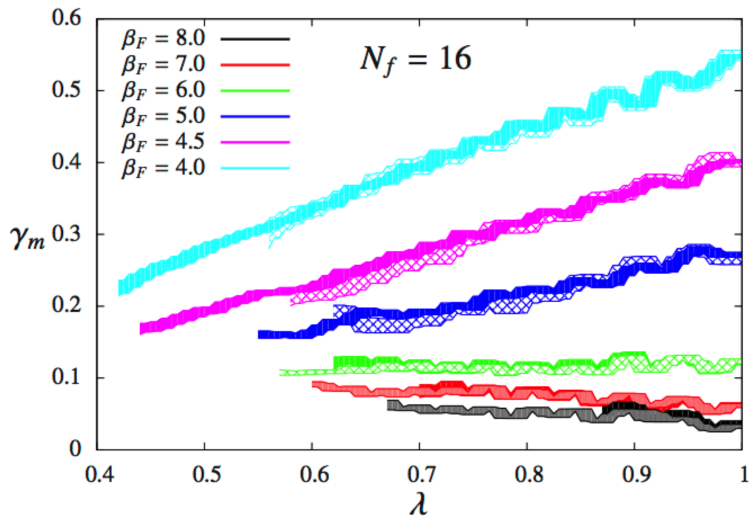

Figure 5.24: The mass anomalous dimension γ_m for $N_f = 16$ system.

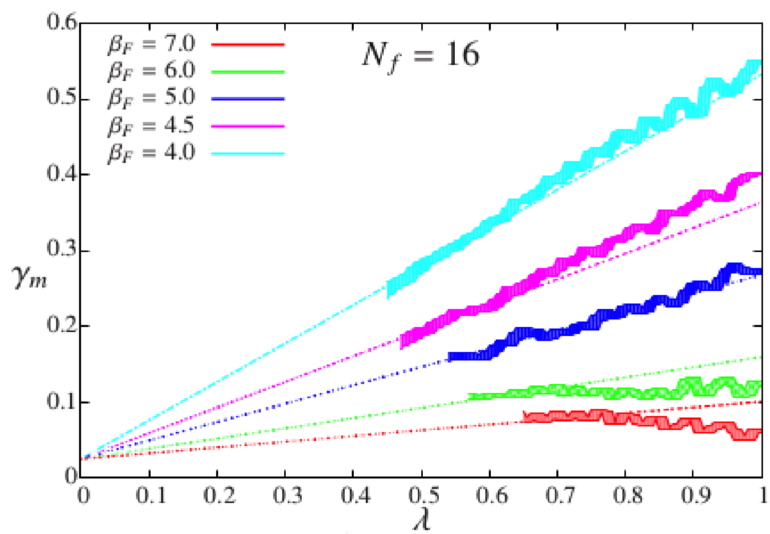

Figure 5.25: Linear extrapolations of γ_m from multiple couplings with a common intercept. The intercept is 0.025(10). Though it should not be taken too seriously, it is consistent with the perturbative prediction 0.022.

12- and 16-flavor SU(3) lattice gauge theories, to investigate systematic effects and to demonstrate that by considering multiple lattice volumes and gauge couplings we can determine the anomalous dimension across a wide range of scales.

In our numerical calculations we used nHYP-smeared staggered fermions and generated gauge configurations at very small or vanishing fermions masses. We directly measured Dirac eigenvalues in our earlier studies, and then applied stochastic estimator to measure the mode number more efficiently. In the direct calculation we measured 1000 to 1500 Dirac eigenvalues for each ensemble. With the stochastic measurement we are able to reach the UV cutoff scale on the lattice where $\lambda \sim 1$. For 8- and 12-flavor system we stay on the weak coupling side of the $\cancel{S^4}$ phase that we discovered in chapter 4. By combining different lattice volumes at fixed gauge coupling we can identify finite-volume effects and determine volume-independent results in an energy range covering about an order of magnitude.

For the 4-flavor system by rescaling with the lattice spacing at different gauge couplings we predict a universal curve, which is consistent with the one-loop perturbation theory in the ultraviolet once the continuum and lattice scales are matched. In the infrared we observe chiral symmetry breaking as expected for a QCD-like system. Our 4-flavor results thus demonstrate the strength of our method.

Our 12-flavor results are very different from the 4-flavor case, and are consistent with the existence of an infrared fixed point. At stronger couplings we observe γ_m increasing towards the ultraviolet, indicating that these systems are not in the basin of attraction of the gaussian fixed point. Our results at different β_F cannot be combined to predict a universal curve, which is consistent with an IRFP with irrelevant gauge couplings. The coupling runs slowly and we observe significant dependence of γ_m on the couplings. However, γ_m at different gauge couplings converge to a common value $\gamma_m^* = 0.235(27)$ in the $\lambda = 0$ limit, which is interpreted as the universal mass anomalous dimension at the IRFP. Our results for the 8-flavor system also illustrate the effects of the slowly-running gauge coupling. We find the anomalous dimension is large over the range of scales accessible at fixed β_F, but shows a strong dependence on the coupling itself. This behavior is consistent with walking dynamics and makes the 8-flavor system very interesting to study.

The 16-flavor system serves as an example of IR-conformal systems. We found the mass anomalous dimension in the 16-flavor system behaves very similar to the 12-flavor system. We encounter large finite volume effects and cut-off effects on the lattice, and do not pursue further with this system. Nevertheless the qualitative behaviors of γ_m in the 16-flavor system support our conclusion of the 12-flavor system.

While the eigenvalues of the Dirac operator can reveal a surprising amount of information, it is clear that this approach has systematic effects that must be understood and addressed. Even in the 12-flavor system that we identify a conformal fixed point in the infrared, the energy dependence of the anomalous dimension can be significant. Analyses that do not check a range of energy scales risk obtaining apparently very precise but actually incorrect results. Extrapolation to the infrared limit is necessary, and may significantly increase the numerical uncertainties. In addition, the slow running of the coupling near the IR fixed point can make results sensitive to β_F, even though the gauge coupling is irrelevant at the IRFP. Investigating several gauge couplings is important to address this systematic effect and confirm that consistent results are obtained from extrapolations to the IR limit. Our method provides a unique probe to study systems from the UV to the IR. It is universal and can be applied to any lattice model of interest, including both chirally broken and IR-conformal systems.

Chapter 6

Conclusion

In this dissertation we have discussed the motivations of our interests in SU(3) gauge theory with many flavor fermions, and the two methods we used in study: the phase structure and the scale-dependent mass anomalous dimension from Dirac eigenmodes.

The walking technicolor models provide an alternative to the standard Higgs model to explain EWSB. They break the eletroweak symmetry via strong interactions and feature a large mass anomalous dimension $\gamma_m \sim 1$ across large energy scales. In particular, the WTC model that posses approximate conformal symmetry predicts a pseudo-Nambu-Goldstone boson associated with the spontaneous (approximate) conformal symmetry breaking, which could play the role of the 125 GeV Higgs-like particle.

It is thus important to check if concrete examples of the walking technicolor models actually exsit. The universal two-loop beta function of SU(N) gauge theory with N_f flavors indicates the existence of a conformal window in N_f, where the beta function has a second zero and the theory is infrared conformal. The walking behaviors are likely to occur slightly below the conformal window, and therefore exact locating the lower edge of the conformal window is the center of the search. This question is non-perturbative in nature and have to be studied on the lattice.

We studied the SU(3) gauge theory with many flavors in the fundamental representation, for which the conformal window from the two-loop beta function is [8.05, 16.5]. We use nHYP smeared staggered fermions with a negative adjoint gauge term in the lattice formulation. We explored the phase structure for the $N_f = 12$ system and extracted the scale-dependent mass anomalous dimension from Dirac eigenmodes for the $N_f = 4, 8, 12, 16$ systems.

In the study of the phase structure we discovered a novel phase for the $N_f = 12$ system where the single site shift symmetry is spontaneous broken. We believe the novel phase is a lattice artifact because the it is confining and chirally symmetric, bounded by first order bulk transitions, and also exists in the $N_f = 8$ system. Other methods are needed to study the weak coupling side of the novel phase for $N_f = 12$ and $N_f = 8$ systems.

We developed a method to extract the scale-dependent mass anomalous dimension from the eigenmode number of the Dirac operator. The scale-dependence of the mass anomalous dimension is firstly reported by us and makes it necessary to explore a range of energy scales as well as multiple gauge couplings in order to obtain correct results.

The results for the $N_f = 4$ system are consistent with an asymptotically free UVFP and coincide with the one-loop perturbative prediction in the ultraviolet. The success on the $N_f = 4$ system demonstrates the power of our method, and confirms that the systematic effects are manageable.

The results for the $N_f = 12$ system are consistent with an IRFP whose mass anomalous dimension is identified to be 0.235(27) by extrapolating the results at different couplings to the infrared limit. The result is very consistent with our finite-size scaling study which predicts $\gamma_m^* = 0.235(15)$. We also tested our methods with twice nHYP smeared configurations and get $\gamma_m^* = 0.231(36)$. The consistency of the predictions from different actions further supports the universality and robustness of our method.

The results for the $N_f = 8$ system are hard to interpret, but we find 'walking' behaviors in the mass anomalous dimension at different gauge couplings, which makes this system interesting to study. The results for the $N_f = 16$ system is very similar to the $N_f = 12$ system and further support the IR-conformal nature of the $N_f = 12$ systems.

The method to extract the scale-dependent mass anomalous dimension from Dirac eigenmode number is universal and can be applied to any lattice model of interest. The stochastic estimator has been adapted to the HISQ and Wilson actions so similar analysis could be performed in the future.

Bibliography

[1] D. Dietrich and F. Sannino, "Conformal window of SU(N) gauge theories with fermions in higher dimensional representations," Physical Review D, vol. 75, p. 085018, Apr. 2007.

[2] A. Hasenfratz, R. Hoffmann, and S. Schaefer, "Hypercubic smeared links for dynamical fermions," Journal of High Energy Physics, vol. 05, May 2007.

[3] M. Creutz and M. Carlo, "Variant actions and phase structure in lattice gauge theory," vol. 24, no. 12, pp. 3212–3217, 1981.

[4] T. Blum, C. DeTar, and U. Heller, "Thermal phase transition in mixed action SU(3) lattice gauge theory and Wilson fermion thermodynamics," Nuclear Physics B, vol. 442, pp. 301–316, 1995.

[5] A. Hasenfratz, "Conformal or walking? MonteCarlo renormalization group studies of SU(3) gauge models with fundamental fermions," Physical Review D, vol. 82, p. 014506, July 2010.

[6] S. Weinberg, "Implications of dynamical symmetry breaking," Physical Review D, vol. 13, no. 4, pp. 974–996, 1976.

[7] L. Susskind, "Dynamics of spontaneous symmetry breaking in the Weinberg-Salam theory," Physical Review D, vol. 20, no. 10, pp. 2619–2625, 1979.

[8] E. Eichten and K. Lane, "Dynamical breaking of weak interaction symmetries," Physics Letters B, vol. 90, no. 1, 1980.

[9] S. Dimopoulos and L. Susskind, "Mass without scalars," Nuclear Physics B, vol. 155, pp. 237–252, 1979.

[10] E. Farhi and L. Susskind, "Technicolour," Physics Reports, vol. 3, no. 3, 1981.

[11] K. Yamawaki, M. Bando, and K. Matumoto, "Scale-invariant hypercolor model and a dilaton," Physical Review Letters, vol. 56, no. 13, pp. 1335–1338, 1986.

[12] T. Appelquist, K. Lane, and U. Mahanta, "Ladder Approximation for Spontaneous Chiral-Symmetry Breaking," Physical Review Letters, vol. 61, no. 14, pp. 1553–1556, 1988.

[13] ATLAS Collaboration, "Observation of a new particle in the search for the Standard Model Higgs boson with the ATLAS detector at the LHC," Physics Letters B, vol. 716, pp. 1–29, Sept. 2012.

[14] CMS Collaboration, "Observation of a new boson at a mass of 125 GeV with the CMS experiment at the LHC," Physics Letters B, vol. 716, pp. 30–61, Sept. 2012.

[15] G. Cacciapaglia and F. Sannino, "Fundamental Composite (Goldstone) Higgs Dynamics," Journal of High Energy Physics, vol. 04, 2014.

[16] M. Bando, K. Matumoto, and K. Yamawaki, "Technidilaton," Physics Letters B, vol. 178, no. 2, 1986.

[17] D. Dietrich, F. Sannino, and K. Tuominen, "Light composite Higgs boson from higher representations versus electroweak precision measurements: Predictions for CERN LHC," Physical Review D, vol. 72, p. 055001, Sept. 2005.

[18] T. Appelquist and Y. Bai, "Light dilaton in walking gauge theories," Physical Review D, vol. 82, p. 071701, Oct. 2010.

[19] Z. Chacko, R. Franceschini, and R. K. Mishra, "Resonance at 125GeV: Higgs or dilaton/radion?," Journal of High Energy Physics, vol. 2013, p. 15, Apr. 2013.

[20] C. T. Hill and E. H. Simmons, "Strong dynamics and electroweak symmetry breaking," vol. 381, pp. 235–402, 2003.

[21] T. Appelquist and G. Wu, "Electroweak chiral Lagrangian and new precision measurements," Physical Review D, vol. 48, no. 7, 1993.

[22] S. Matsuzaki and K. Yamawaki, "Discovering the 125GeV techni-dilaton at the LHC," Physical Review D, vol. 86, p. 035025, Aug. 2012.

[23] S. Matsuzaki and K. Yamawaki, "Techni-dilaton at 125GeV," Physical Review D, vol. 85, p. 095020, May 2012.

[24] W. Caswell, "Asymptotic behavior of non-abelian gauge theories to two-loop order," Physical Review Letters, vol. 33, no. 4, pp. 4–6, 1974.

[25] L. D. Debbio, "The conformal window on the lattice," Pos Lattice 2010, no. 004, 2011.

[26] E. T. Neil, "Exploring models for new physics on the lattice," Pos Lattice 2011, no. 009, 2011.

[27] J. Giedt, "Lattice gauge theory and physics beyond the standard model," Pos Lattice 2012, no. 006, 2012.

[28] Y. Aoki, T. Aoyama, M. Kurachi, T. Maskawa, K.-i. Nagai, H. Ohki, A. Shibata, K. Yamawaki, and T. Yamazaki, "Walking signals in $N_f = 8$ QCD on the lattice," Physical Review D, vol. 87, p. 094511, May 2013.

[29] T. Appelquist, G. Fleming, and E. Neil, "Lattice study of conformal behavior in SU(3) Yang-Mills theories," Physical Review D, vol. 79, p. 076010, Apr. 2009.

[30] a. Deuzeman, M. P. Lombardo, and E. Pallante, "Evidence for a conformal phase in SU(N) gauge theories," Physical Review D, vol. 82, p. 074503, Oct. 2010.

[31] X.-y. Jin and R. D. Mawhinney, "Lattice QCD with 8 and 12 degenerate quark flavors," Pos Lattice 2009, no. 049, 2009.

[32] A. Deuzeman, E. Pallante, M. P. Lombardo, I.-l. N. Frascati, and F. Rm, "The bulk transition of many-flavor QCD and the search for a UVFP at strong coupling," Pos Lattice 2010, no. 067, 2010.

[33] Z. Fodor, K. Holland, J. Kuti, D. Nógrádi, C. Schroeder, and C. H. Wong, "Can the nearly conformal sextet gauge model hide the Higgs impostor?," Physics Letters B, vol. 718, pp. 657–666, Dec. 2012.

[34] A. Hasenfratz, "Infrared Fixed Point of the 12-Fermion SU(3) Gauge Model Based on 2-Lattice MonteCarlo Renomalization-Group Matching," Physical Review Letters, vol. 108, p. 061601, Feb. 2012.

[35] T. Appelquist, G. T. Fleming, M. F. Lin, E. T. Neil, and D. a. Schaich, "Lattice simulations and infrared conformality," Physical Review D, vol. 84, p. 054501, Sept. 2011.

[36] T. DeGrand, "Finite-size scaling tests for spectra in SU(3) lattice gauge theory coupled to 12 fundamental flavor fermions," Physical Review D, vol. 84, p. 116901, Dec. 2011.

[37] K. Ogawa, T. Aoyama, H. Ikeda, M. Kurachi, C.-J. D. Lin, H. Matsufuru, H. Ohki, T. Onogi, E. Shintani, and T. Yamazaki, "The infrared behavior of SU(3) $N_f = 12$ gauge theory-about the existence of conformal fixed point-," Pos Lattice 2011, no. 081, 2011.

[38] A. Deuzeman and M. P. Lombardo, "Bulk transitions of twelve flavor QCD and $U_A(1)$ symmetry," Pos Lattice 2010, no. 321, 2011.

[39] A. Hasenfratz, "MCRG study of 12 fundamental flavors with mixed fundamental-adjoint gauge action," Pos Lattice 2011, no. 065, 2011.

[40] A. Deuzeman and M. P. Lombardo, "On the spectrum of QCD-like theories and the conformal window," Pos Lattice 2011, no. 083, 2012.

[41] Y. Aoki, T. Aoyama, M. Kurachi, and T. Maskawa, "Many flavor QCD with $N_f = 12$ and 16," Pos Lattice 2011, no. 053, 2012.

[42] X.-y. Jin and R. D. Mawhinney, "Lattice QCD with 12 degenerate quark flavors," Pos Lattice 2011, no. 066, 2012.

[43] Y. Aoki, T. Aoyama, M. Kurachi, T. Maskawa, K.-i. Nagai, H. Ohki, E. Rinaldi, A. Shibata, K. Yamawaki, T. Yamazaki, and L. Collaboration, "Light Composite Scalar in Twelve-Flavor QCD on the Lattice," vol. 162001, no. October, pp. 1–5, 2013.

[44] T. a. Ryttov and R. Shrock, "Higher-loop corrections to the infrared evolution of a gauge theory with fermions," Physical Review D, vol. 83, p. 056011, Mar. 2011.

[45] C. Pica and F. Sannino, "Ultraviolet and infrared zeros of gauge theories at the four-loop order and beyond," Physical Review D, vol. 83, p. 035013, Feb. 2011.

[46] T. Appelquist, J. Terning, and L. Wijewardhana, "Zero Temperature Chiral Phase Transition in SU(N) Gauge Theories.," Physical review letters, vol. 77, pp. 1214–1217, Aug. 1996.

[47] T. Appelquist, A. Cohen, and M. Schmaltz, "A new constraint on strongly coupled field theories," vol. 60, p. 045003, 1999.

[48] Z. Fodor, K. Holland, J. Kuti, D. Nógrádi, and C. Schroeder, "Nearly conformal gauge theories in finite volume," Physics Letters B, vol. 681, pp. 353–361, Nov. 2009.

[49] A. Cheng, A. Hasenfratz, and D. Schaich, "Novel phase in SU(3) lattice gauge theory with 12 light fermions," Physical Review D, vol. 85, p. 094509, May 2012.

[50] D. Schaich, A. Cheng, A. Hasenfratz, and G. Petropoulos, "Bulk and finite-temperature transitions in SU(3) gauge theories with many light fermions," PoS Lattice 2012, no. 028, 2012.

[51] A. Deuzeman, M. P. Lombardo, and E. Pallante, "The physics of eight flavours," Physics Letters B, vol. 670, pp. 41–48, Dec. 2008.

[52] X.-Y. Jin and R. D. Mawhinney, "Evidence for a First Order , Finite Temperature Phase Transition in 8 Flavor QCD," Pos Lattice 2010, no. 055, 2010.

[53] K. Miura, M. P. Lombardo, and E. Pallante, "Chiral phase transition at finite temperature and conformal dynamics in large QCD," Physics Letters B, vol. 710, pp. 676–682, Apr. 2012.

[54] Y. Aoki, T. Aoyama, M. Kurachi, and T. Maskawa, "Many flavor QCD as exploration of the walking behavior with the approximate IR fixed point," Pos Lattice 2011, no. 080, 2011.

[55] Y. Aoki, T. Aoyama, M. Kurachi, and T. Maskawa, "Exploring walking behavior in SU (3) gauge theory with 4 and 8 HISQ quarks," Pos Lattice 2012, no. 035, 2013.

[56] C. Davies, E. Follana, a. Gray, G. Lepage, Q. Mason, M. Nobes, J. Shigemitsu, H. Trottier, M. Wingate, C. Aubin, C. Bernard, T. Burch, C. DeTar, S. Gottlieb, E. Gregory, U. Heller, J. Hetrick, J. Osborn, R. Sugar, D. Toussaint, M. Pierro, a. El-Khadra, a. Kronfeld, P. Mackenzie, D. Menscher, and J. Simone, "High-Precision Lattice QCD Confronts Experiment," Physical Review Letters, vol. 92, p. 022001, Jan. 2004.

[57] C. Aubin, C. Bernard, C. DeTar, M. DiPierro, a. El-Khadra, S. Gottlieb, E. Gregory, U. Heller, J. Hetrick, a. Kronfeld, P. Mackenzie, D. Menscher, M. Nobes, M. Okamoto, M. Oktay, J. Osborn, J. Simone, R. Sugar, D. Toussaint, and H. Trottier, "Semileptonic Decays of D Mesons in Three-Flavor Lattice QCD," Physical Review Letters, vol. 94, p. 011601, Jan. 2005.

[58] I. Allison, C. Davies, A. Gray, A. Kronfeld, P. Mackenzie, and J. Simone, "Mass of the Bc Meson in Three-Flavor Lattice QCD," Physical Review Letters, vol. 94, p. 172001, May 2005.

[59] C. Aubin, C. Bernard, C. DeTar, M. Di Pierro, E. Freeland, S. Gottlieb, U. Heller, J. Hetrick, a. El-Khadra, a. Kronfeld, L. Levkova, P. Mackenzie, D. Menscher, F. Maresca, M. Nobes, M. Okamoto, D. Renner, J. Simone, R. Sugar, D. Toussaint, and H. Trottier, "Charmed-Meson Decay Constants in Three-Flavor Lattice QCD," Physical Review Letters, vol. 95, p. 122002, Sept. 2005.

[60] R. Gupta, "Introduction to lattice QCD," arXiv preprint hep-lat/9807028, 1998.

[61] M. Lüscher, "Advanced Lattice QCD," arXiv preprint hep-lat/9802029, 1998.

[62] M. Luscher, "Computational Strategies in Lattice QCD," arXiv preprint hep-lat/1002.4232, 2010.

[63] P. Weisz, "Renormalization and lattice artifacts," arXiv preprint hep-lat/1004.3462, 2010.

[64] A. Vladikas, "Three topics in renormalization and improvement," arXiv preprint hep-lat/1103.1323, 2011.

[65] K. Wilson, "Confinement of quarks," Physical Review D, vol. 10, no. 8, p. 2445, 1974.

[66] K. Symanzik, "Continuum limit and improved action in lattice theories (II)," Nuclear Physics B, vol. 226, pp. 205–227, 1983.

[67] P. Weisz, "Continuum limit improved lattice action for pure Yang-Mills theory (I)," Nuclear Physics B, vol. 212, pp. 1–17, 1983.

[68] M. Lüscher and P. Weisz, "Computation of the action for on-shell improved lattice gauge theories at weak coupling," Physics Letters B, vol. 158, no. 3, 1985.

[69] J. Kogut and L. Susskind, "Hamiltonian formulation of Wilson's lattice gauge theories," Physical Review D, vol. 11, no. 2, 1975.

[70] H. Hamber, E. Marinari, G. Parisi, and C. Rebbi, "Numerical simulations of quantum chromodynamics," Physics Letters B, vol. 124, no. 1, pp. 99–104, 1983.

[71] F. Fucito and S. Solomon, "The SU(3) deconfining transition in the presence of quarks," Physics Letters B, no. June, pp. 387–391, 1984.

[72] S. Gottlieb, W. Liu, R. Renken, R. Sugar, and D. Toussaint, "Hadron asses with two quark flavors," Physical Review D, vol. 38, no. 7, p. 2245, 1988.

[73] M. Creutz, "Chiral anomalies and rooted staggered fermions," Physics Letters B, vol. 649, pp. 230–234, May 2007.

[74] M. Creutz, "Reply to: Comment on: Chiral anomalies and rooted staggered fermions [Phys. Lett. B 649 (2007) 230] [Phys. Lett. B 649 (2007) 235]," Physics Letters B, vol. 649, pp. 241–242, May 2007.

[75] C. Bernard, M. Golterman, Y. Shamir, and S. R. Sharpe, "Comment on: Chiral anomalies and rooted staggered fermions [Phys. Lett. B 649 (2007) 230]," Physics Letters B, vol. 649, pp. 235–240, May 2007.

[76] A. Kronfeld, "Lattice gauge theory with staggered fermions: how, where, and why (not)," PoS Lattice 2007, vol. 016, 2007.

[77] D. B. Kaplan, "Chiral Symmetry and Lattice Fermions," Dec. 2009.

[78] A. Hasenfratz, R. Hoffmann, and F. Knechtli, "The static potential with hypercubic blocking," Nuclear Physics B - Proceedings Supplements, vol. 106-107, pp. 418–420, Mar. 2002.

[79] S. Aoki, "New phase structure for lattice QCD with Wilson fermions," Physical Review D, vol. 30, no. 12, 1984.

[80] G. Bhanot, "SU(3) lattice gauge theory in 4 dimensions with a modified Wilson Action," Physics Letters B, vol. 108, no. 4, pp. 337–340, 1982.

[81] E. Tomboulis and a. Velytsky, "Improving the Improved Action," Physical Review Letters, vol. 98, p. 181601, May 2007.

[82] E. Tomboulis and a. Velytsky, "Renormalization group therapy," Physical Review D, vol. 75, p. 076002, Apr. 2007.

[83] M. Hasenbusch and S. Necco, "SU(3) lattice gauge theory with a mixed fundamental and adjoint plaquette action: lattice artefacts," Journal of High Energy Physics, vol. 08, no. 005, 2004.

[84] R. Sommer, "A new way to set the energy scale in lattice gauge theories and its application to the static force and in alpha_s SU(2) Yang-Mills theory," Nuclear Physics B, vol. 411, pp. 839–854, 1994.

[85] T. Takaishi and P. de Forcrand, "Testing and tuning symplectic integrators for the hybrid Monte Carlo algorithm in lattice QCD," Physical Review E, vol. 73, p. 036706, Mar. 2006.

[86] M. Hasenbusch and K. Jansen, "Speeding up lattice QCD simulations with clover-improved Wilson fermions," Nuclear Physics B, vol. 659, pp. 299–320, May 2003.

[87] C. Urbach, K. Jansen, a. Shindler, and U. Wenger, "HMC algorithm with multiple time scale integration and mass preconditioning," Computer Physics Communications, vol. 174, pp. 87–98, Jan. 2006.

[88] M. Golterman and J. Smit, "Self-energy and flavor interpretation of staggered fermions," Nuclear Physics B, vol. 245, pp. 61–88, 1984.

[89] T. DeGrand, "Finite-size scaling tests for SU(3) lattice gauge theory with color sextet fermions," Physical Review D, vol. 80, p. 114507, Dec. 2009.

[90] P. Damgaard, U. Heller, R. Niclasen, and K. Rummukainen, "Low-lying eigenvalues of the QCD Dirac operator at finite temperature," Nuclear Physics B, vol. 583, pp. 347–367, Sept. 2000.

[91] M. Bowick and E. Brézin, "Universal scaling of the tail of the density of eigenvalues in random matrix models," Physics Letters B, vol. 268, no. M, pp. 21–28, 1991.

[92] G. Akemann, P. Damgaard, U. Magnea, and S. Nishigaki, "Universality of random matrices in the microscopic limit and the Dirac operator spectrum," Nuclear Physics B, vol. 3, pp. 721–738, 1997.

[93] T. Banks and A. Casher, "Chiral Symmetry Breaking in Confining Theories," Nuclear Physics B, vol. 169, pp. 103–125, 1980.

[94] J. Stern, "Light quark masses and condensates in QCD," arXiv preprint hep-ph/9712438, 1997.

[95] J. Stern, "Two alternatives of spontaneous chiral symmetry breaking in QCD," arXiv preprint hep-ph/9801282, 1998.

[96] I. Kogan, A. Kovner, and M. Shifman, "Chiral symmetry breaking without bilinear condensates, unbroken axial Z_N symmetry, and exact QCD inequalities," Physical Review D, vol. 59, p. 016001, 1998.

[97] S. Chandrasekharan, D. Chen, N. Christ, W. Lee, R. Mawhinney, and P. Vranas, "Anomalous Chiral Symmetry Breaking above the QCD Phase Transition," Physical Review Letters, vol. 82, pp. 2463–2466, Mar. 1999.

[98] Z. Fodor, K. Holland, J. Kuti, D. Nógrádi, and C. Schroeder, "Twelve massless flavors and three colors below the conformal window," Physics Letters B, vol. 703, pp. 348–358, Sept. 2011.

[99] C. Aubin and Q. Wang, "Possible Aoki phase for staggered fermions," Physical Review D, vol. 70, p. 114504, Dec. 2004.

[100] J. Verbaarschot and I. Zahed, "Spectral Density of the QCD Dirac Operator near Zero Virtuality," Physical Review Letters, vol. 70, no. 25, pp. 3852–3855, 1993.

[101] E. Shuryak and J. Verbaarschot, "Random matrix theory and spectral sum rules for the Dirac operator in QCD," Nuclear Physics A, vol. 560, pp. 306–320, 1993.

[102] P. Damgaard and U. Heller, "Eigenvalue distributions of the QCD Dirac operator," Physics Letters B, vol. 495, no. December, pp. 263–270, 2000.

[103] E. Follana, a. Hart, C. Davies, and Q. Mason, "Low-lying Dirac spectrum of staggered quarks," Physical Review D, vol. 72, p. 054501, Sept. 2005.

[104] T. DeGrand and S. Schaefer, "Parameters of the lowest order chiral Lagrangian from fermion eigenvalues," Physical Review D, vol. 76, p. 094509, Nov. 2007.

[105] P. H. Damgaard, U. M. Heller, and K. Splittorff, "New ways to determine low-energy constants with Wilson fermions," Physical Review D, vol. 86, p. 094502, Nov. 2012.

[106] J.-w. Lee, M. Hanada, and N. Yamada, "Large N_c volume reduction and chiral random matrix theory," PoS Lattice 2012, no. 047, 2013.

[107] L. Giusti and M. Lüscher, "Chiral symmetry breaking and the Banks-Casher relation in lattice QCD with Wilson quarks," Journal of High Energy Physics, vol. 2009, pp. 013–013, Mar. 2009.

[108] L. Del Debbio and R. Zwicky, "Hyperscaling relations in mass-deformed conformal gauge theories," Physical Review D, vol. 82, p. 014502, July 2010.

[109] H. Leutwyler and A. Smilga, "Spectrum of Dirac operator and role of winding number in QCD," Physical Review D, vol. 46, no. 12, 1992.

[110] A. Patella, "A precise determination of the $\bar{\psi}\psi$ anomalous dimension in conformal gauge theories," Physical Review D, vol. 86, p. 025006, July 2012.

[111] L. Keegan, "Mass Anomalous Dimension at Large N," PoS Lattice 2012, no. 044, 2012.

[112] J. Osborn, D. Toublan, and J. Verbaarschot, "From chiral random matrix theory to chiral perturbation theory," Nuclear Physics B, vol. 540, pp. 317–344, Feb. 1999.

[113] T. Kalkreuter and H. Simma, "An accelerated conjugate gradient algorithm to compute low-lying eigenvaluesa study for the Dirac operator in SU(2) lattice QCD," Computer Physics Communications, vol. 93, pp. 33–47, 1996.

[114] A. Stathopoulos and J. McCombs, "PRIMME: preconditioned iterative multimethod eigensolvermethods and software description," ACM Transaction on Mathematical Software, vol. 37, no. 2, 2010.

[115] L. Giusti, C. Hoelbling, M. Lüscher, and H. Wittig, "Numerical techniques for lattice QCD in the ϵ-regime," Computer Physics Communications, vol. 153, pp. 31–51, June 2003.

[116] T. DeGrand, Y. Shamir, and B. Svetitsky, "Mass anomalous dimension in sextet QCD," Physical Review D, vol. 87, p. 074507, Apr. 2013.

[117] T. DeGrand, Y. Shamir, and B. Svetitsky, "Infrared fixed point in SU(2) gauge theory with adjoint fermions," Physical Review D, vol. 83, p. 074507, Apr. 2011.

[118] Y. Aoki, T. Aoyama, M. Kurachi, T. Maskawa, K.-i. Nagai, H. Ohki, A. Shibata, K. Yamawaki, and T. Yamazaki, "Lattice study of conformality in twelve-flavor QCD," Physical Review D, vol. 86, p. 054506, Sept. 2012.

[119] Z. Fodor, J. Kuti, and C. Schroeder, "Conformal finite size scaling of twelve fermion flavors," Pos Lattice 2012, no. 279, 2012.

[120] A. Cheng, A. Hasenfratz, Y. Liu, G. Petropoulos, and D. Schaich, "Finite size scaling of conformal theories in the presence of a near-marginal operator," Physical Review D, vol. 90, p. 014509, July 2014.

[121] G. Petropoulos, A. Cheng, A. Hasenfratz, and D. Schaich, "MCRG study of 8 and 12 fundamental flavors," Pos Lattice 2012, no. 051, 2012.

[122] N. Manton, "An alternative action for lattice gauge theories," Physics Letters B, vol. 96, no. 3, pp. 4–6, 1980.

[123] A. Hasenfratz and F. Knechtli, "Flavor symmetry and the static potential with hypercubic blocking," Physical Review D, vol. 64, p. 034504, July 2001.

[124] M. Albanese, F. Costantini, and G. Fiorentini, "Glueball masses and string tension in lattice QCD," Physics Letters B, vol. 192, no. 1, pp. 163–169, 1987.

[125] A. Hasenfratz, "Investigating the critical properties of beyond-QCD theories using Monte-Carlo renormalization group matching," Physical Review D, vol. 80, p. 034505, Aug. 2009.

[126] D. Daniel and T. Kieu, "On the flavor interpretations of staggered fermions," Physics Letters B, vol. 175, no. 1, pp. 73–76, 1986.

[127] T. Banks and A. Zaks, "On The Phase Structure of Vector-Like Gauge Theories With Massless Fermions," Nuclear Physics B, vol. 196, pp. 189–204, 1982.

[128] L. D. Debbio and L. Giusti, "Stability of lattice QCD simulations and the thermodynamic limit," Journal of High Energy Physics, vol. 02, no. 011, 2006.

[129] K. Orginos, D. Toussaint, and R. Sugar, "Variants of fattening and flavor symmetry restoration," Physical Review D, vol. 60, p. 054503, July 1999.

Appendix A

Code of the step function in the stochastic estimator

```
// -----------------------------------------------------------------
// Step function implemented through Clenshaw algorithm
#include "mode_includes.h"
// -----------------------------------------------------------------


// -----------------------------------------------------------------
// dest = src - 8M^2 (DD^dag + 4M^2)^{-1} src
// Hard-code EVEN parity in inverse
void X(field_offset src, field_offset dest) {
  register int i;
  register site *s;
  Real MSq_x2 = -8 * M * M / starSq;

  // psi = (DD^dag + 4M^2)^{-1} src
  clear_latvec(F_OFFSET(psi), EVENANDODD);    // Zero initial guess
#ifdef CG_DEBUG
  int iters = ks_congrad(src, F_OFFSET(psi), M / star, EVEN);
  node0_printf("%d iters in congrad with M=%.4g\n", iters, M / star);
#else
```

```
  ks_congrad(src, F_OFFSET(psi), M / star, EVEN);
#endif

  // dest = src - 8M^2 psi
  FOREVENSITES(i, s)
    scalar_mult_add_su3_vector((su3_vector *)F_PT(s, src), &(s->psi),
                               MSq_x2, (su3_vector *)F_PT(s, dest));
}
// -----------------------------------------------------------------

// -----------------------------------------------------------------
// dest = (2X^2 - 1 - epsilon) src / (1 - epsilon)
// Hard-code EVEN parity
void Z(field_offset src, field_offset dest) {
  register int i;
  register site *s;
  double toAdd = -1.0 - epsilon;
  double norm = 1.0 / (1.0 - epsilon);

  X(src, F_OFFSET(R1));
  X(F_OFFSET(R1), F_OFFSET(Xsrc));

  FOREVENSITES(i, s) {
    scalar_mult_su3_vector(&(s->Xsrc), 2, &(s->Xsrc));
    scalar_mult_add_su3_vector(&(s->Xsrc), (su3_vector *)F_PT(s, src),
                               toAdd, (su3_vector *)F_PT(s, dest));
    scalar_mult_su3_vector((su3_vector *)F_PT(s, dest), norm,
```

```
                               (su3_vector *)F_PT(s, dest));
  }
}
// ----------------------------------------------------------------


// ----------------------------------------------------------------
// Clenshaw algorithm:
// P(x)R(0) = \sum_i^n c[i]T[i]R(0) = (b[0] - xb[1])R(0);
// where b[i] = c[i] + 2zb[i + 1] - b[i + 2], b[n] = b[n + 1] = 0;
// so want to compute b[0]-xb[1];
// Hard-code EVEN parity
void clenshaw(field_offset src, field_offset dest) {
  register int i;
  register site *s;
  int j;

  for (j = Norder; j >= 0; j--) {
    // Construct bj.src = (cj + 2Zbjp1 - bjp2).src
    // Start with bj.src = cj.src
    FOREVENSITES(i, s)
      scalar_mult_su3_vector((su3_vector *)F_PT(s, src), coeffs[j], &(s->bj));

    // Now subtract bjp2.src calculated in previous iterations
    if (j < Norder - 1) {
      FOREVENSITES(i, s)
        scalar_mult_add_su3_vector(&(s->bj), &(s->bjp2), -1, &(s->bj));
    }
```

```
    // Finally we need 2Z(bjp1.src)
    // Based on bjp1.src calculated in previous iterations
    if (j < Norder) {
      Z(F_OFFSET(bjp1), F_OFFSET(Zbjp1));
      FOREVENSITES(i, s)
        scalar_mult_add_su3_vector(&(s->bj), &(s->Zbjp1), 2, &(s->bj));
    }

    // Now move bjp1-->bjp2 and bj-->bjp1 for next iteration
    if (j > 0) {
      copy_latvec(F_OFFSET(bjp1), F_OFFSET(bjp2), EVENANDODD);
      copy_latvec(F_OFFSET(bj), F_OFFSET(bjp1), EVENANDODD);
    }
  }

  // We now have bj = b[0].src and Zbjp1 = Z(b[1].src)
  // We want to return (b[0].src - Z(b[1].src))
  FOREVENSITES(i, s) {
    scalar_mult_add_su3_vector(&(s->bj), &(s->Zbjp1), -1,
                               (su3_vector *)F_PT(s, dest));
  }
}
// -----------------------------------------------------------------


// -----------------------------------------------------------------
// Step function approximated by h(x) = [1 - xp(x)^2] / 2
```

```
// Hard-code EVEN parity
void step(field_offset src, field_offset dest) {
  register int i;
  register site *s;

  // dest = P(X^2) src temporarily
  clenshaw(src, dest);

  // dest = (src - X P(X^2) src) / 2
  X(dest, F_OFFSET(Xsrc));
  FOREVENSITES(i, s) {
    scalar_mult_add_su3_vector((su3_vector *)F_PT(s, src), &(s->Xsrc), -1,
                               (su3_vector *)F_PT(s, dest));
    scalar_mult_su3_vector((su3_vector *)F_PT(s, dest), 0.5,
                           (su3_vector *)F_PT(s, dest));
  }
}
// ------------------------------------------------------------------
```